Imperial College London
Department of Computing

Robotic Manipulators for Single Access Surgery

Piyamate Wisanuvej

August 2018

Supervised by Professor Guang-Zhong Yang and
Professor Lord Ara Darzi

Submitted in part fulfilment of the requirements for the degree of
Doctor of Philosophy in Computing of Imperial College London
and the Diploma of Imperial College London

Declaration

I herewith certify that all material in this dissertation which is not my own work has been properly acknowledged.

Piyamate Wisanuvej

Copyright

Abstract

This thesis explores the development of cooperative robotic manipulators for enhancing surgical precision and patient outcomes in single-access surgery and, specifically, Transanal Endoscopic Microsurgery (TEM). During these procedures, surgeons manipulate a heavy set of instruments via a mechanical clamp inserted in the patient's body through a surgical port, resulting in imprecise movements, increased patient risks, and increased operating time. Therefore, an articulated robotic manipulator with passive joints is initially introduced, featuring built-in position and force sensors in each joint and electronic joint brakes for instant lock/release capability.

The articulated manipulator concept is further improved with motorised joints, evolving into an active tool holder. The joints allow the incorporation of advanced robotic capabilities such as ultra-lightweight gravity compensation and hands-on kinematic reconfiguration, which can optimise the placement of the tool holder in the operating theatre.

Due to the enhanced sensing capabilities, the application of the active robotic manipulator was further explored in conjunction with advanced image guidance approaches such as endomicroscopy. Recent advances in probe-based optical imaging such as confocal endomicroscopy is making inroads in clinical uses. However, the challenging manipulation of imaging probes hinders their practical adoption. Therefore, a combination of the fully cooperative robotic manipulator with a high-speed scanning endomicroscopy instrument is presented, simplifying the incorporation of optical biopsy techniques in routine surgical workflows.

Finally, another embodiment of a cooperative robotic manipulator is presented as an input interface to control a highly-articulated robotic instrument for TEM. This master-slave interface alleviates the drawbacks of traditional master-slave devices, e.g., using clutching mechanics to compensate for the mismatch between slave and master workspaces, and the lack of intuitive manipulation feedback, e.g. joint limits, to the user. To address those drawbacks a joint-space robotic manipulator is proposed emulating the kinematic structure of the flexible robotic instrument under control.

Acknowledgement

I would like to express my gratitude to numerous people who have been tremendously supportive in making this thesis possible. First of all, thank you to my supervisor Professor Guang-Zhong Yang, without whom this work would not have been possible. I am very grateful to have been granted this opportunity to conduct my research at The Hamlyn Centre, with access to such cutting-edge facilities and extremely pleasant environment. I would also like to thank my second supervisor Professor Lord Ara Darzi. I am honoured to have worked alongside and learned from such an incredible surgeon, someone with crucial contributions to research in medicine, especially in minimally invasive and robotic-assisted surgery.

Furthermore, thank you to Jindong Liu, with whom I have been working closely since the beginning of my PhD. I appreciate his generosity in being very supportive and providing practical solutions for all the technical difficulties I have encountered.

I would like to express my sincere thank to Professor Brian Davies and Professor Peter Kazanzides who spent their precious time examining this thesis and providing a significant amount of feedback.

Moreover, I would like to acknowledge the Institute of Global Health Innovation, the Department of Computing, and the administrative team behind them; especially, Nicolette Davies, Raphaële Raupp, Amani El-Kholy, Marina Hall, and Yakov Boglev, who facilitated necessary support required to accomplish my research throughout the years.

I would like to extend my gratitude to Kasetsart University, who granted me an invaluable scholarship to be able to work on this PhD, and without which this research would not have been possible.

In addition, I would like to mention that I have been lucky enough to work alongside and be motivated by Petros Giataganas, Konrad Leibrandt, and

Gauthier Gras, three exceptional engineers that have been through many deadlines together. Thank you to all members of The Hamlyn Centre with whom I have worked and socialised, with particular mentions to Carlo Alberto Seneci, Maria Grammatikopoulou, Andreas Schmitz, Pierre Berthet-Rayne, Maura Power, Jianzhong Shang, Khushi Lavsi, Michael Hughes, Christos Bergeles, Lin Zhang, Chistopher Payne, and Hani Marcus.

Additionally, a special thanks to Van – Wichurat Sakulpaptong, who has always been there to support me through hard times. And last but not least, I owe my sincere gratitude to my parents, Prapairut Sampachanya and Sittisak Wisanuvej, for encouraging me to pursue my interests in this academic career.

Contents

List of Tables **11**

List of Figures **13**

List of Acronyms **19**

1 Introduction **21**

1.1 Contributions 23
1.2 Research Contributions 25
1.3 Publications 28

2 Background **31**

2.1 Single Access Surgical Systems 31
2.2 Robotic Assisted Surgical Tool Holders 35
2.3 Safe Robotic Manipulators working in Human Environment . 37
2.4 Robotic-Assisted Endomicroscopy Systems 39
2.5 Master Interfaces for Robotic Surgery 41
2.5.1 Developments of Master Interface for Robotic Surgery 42
2.5.2 Commercial Haptic Interfaces 43
2.6 Conclusions 43

3 Articulated Dock with Passive Joints for Surgical Instruments **46**

3.1 Introduction 46
3.2 Design 47
3.3 Characterisation 50
3.4 Clinical Trials 52
3.5 Results 54
3.6 Conclusions 57

4 Hamlyn Active Arm – Articulated Robotic Manipulator for Surgical Applications **58**
4.1 Introduction . . . 58
4.2 Hamlyn Active Arm . . . 61
4.3 Methods . . . 61
4.4 Hands-on Positioning with Weight Compensation . . . 61
4.4.1 Pseudo-null-space Inverse Kinematics . . . 66
4.4.2 Inverse Kinematics Experimental Results . . . 67
4.4.3 Hands-on Manipulator Reconfiguration . . . 68
4.5 Experiments and Results . . . 70
4.5.1 Hands-on Positioning User Study . . . 70
4.5.2 Hands-on Positioning – Experimental Results . . . 72
4.5.3 Hands-on Reconfiguration User Study . . . 73
4.5.4 Hands-on Reconfiguration – Experimental Results . . . 77
4.6 Conclusions . . . 79

5 Collision Detection and Object Characterisation with Robotic Manipulators **80**
5.1 Introduction . . . 80
5.2 Methodology . . . 81
5.2.1 Robot Hardware . . . 81
5.2.2 Blind Collision Detection . . . 82
5.2.3 Object Identification . . . 88
5.2.4 Environment Exploration . . . 92
5.3 Experiments . . . 93
5.3.1 Collision Detection . . . 93
5.3.2 Object Identification . . . 93
5.3.3 Environment Exploration . . . 96
5.4 Results . . . 97
5.4.1 Collision Detection . . . 97
5.4.2 Object Identification . . . 99
5.4.3 Environment Exploration . . . 99
5.5 Conclusions . . . 103

6 Robotic-assisted Endomicroscopy with Hamlyn Active Arm **104**
6.1 Introduction . . . 104

6.2 Materials and Methods 105
6.2.1 Hamlyn Active Arm 105
6.2.2 Endomicroscopy 106
6.2.3 Differential Inverse Kinematics 107
6.2.4 Workspace Analysis 108
6.2.5 Contact Force and Orientation Control 109
6.2.6 Modelling and Calibration 112
6.3 Experimental Results 113
6.3.1 Microscopy Probe Weight Modelling 113
6.3.2 Force Controller 113
6.3.3 Wide-area Microscopy Scanning 116
6.3.4 Motion Compensation 118
6.4 Conclusions 118

7 Master Manipulator for Teleoperation of Single Access Surgical Instruments 122
7.1 Introduction 122
7.2 Manipulator Design 124
7.2.1 Surgical Instrument 124
7.2.2 Hardware Design 126
7.2.3 Grip Angle Sensing 127
7.2.4 Dependent Joint Designs 127
7.2.5 Workspace Analysis 131
7.3 Control System 134
7.3.1 Joint Limit Force Rendering 135
7.3.2 Gravity Compensation 135
7.3.3 Friction Compensation 136
7.4 Experimental Results 137
7.4.1 Gravity and Friction Compensations 137
7.4.2 Usability Study 139
7.4.3 Suturing Test 143
7.5 Conclusion 143

8 Conclusions and Future Research Directions 146
8.1 Contributions of this Thesis 146
8.2 Future Research Directions 147

8.3 Conclusions 149

Bibliography **151**

List of Tables

2.1 Manufacturer specifications of the commercially available haptic devices 44

3.1 Structural stiffness test results based on different arm configurations shown in Fig. 3.7. The stiffness values are obtained from linear regression using deformation and force information, with R^2 showing the coefficient of determination. 51
3.2 Statistics of the Hamlyn Lightweight Robot Arm in human trials. *Surgical Phases: I–visual rectal examination, II–main procedure, III–post-procedure assessment. 56

4.1 Comparison between configurations for cooperative manipulation 60
4.2 Results from hands-on positioning experiment showing $MEAN \pm SD$ and $(MIN - MAX)$ 74
4.3 Results from hands-on reconfiguration experiment showing $MEAN \pm SD$ and $(MIN - MAX)$ 78

5.1 Material properties of the solenoid tips used in the object identification experiment 93
5.2 root-mean-square error (RMSE) values for the direction and magnitude estimations between the estimated and actual value in the experiments 98
5.3 Confusion matrix for the highest-accuracy classifier, Neural Network (overall 98% correct) 100
5.4 *InfoGain* ranking values for the signal features used, higher values mean higher contribution to classification accuracy 100
5.5 Root mean square values of the distance between the estimated environment points and the actual environment surface in blind environment exploration experiments 100

6.1 Comparison of probe weight compensation results between the measured and corrected values of force and torques. . . . 115

7.1 Task execution times (in second) between the master manipulators, with statistical values. 141

7.2 Comparison of the number of times the peg was dropped or had to be placed down for repositioning, and the number of times the master devices had to be clutched. 143

List of Figures

2.1 da Vinci Si with Single-Site Instrumentation robotic system from Intuitive Surgical. @2011 Intuitive Surgical Inc. 32

2.2 da Vinci Sp robotic system from Intuitive Surgical; (left) patient-side cart with a surgical port and 4 robotic tools, (centre) vision stack and (right) surgeon's console. @2014 Intuitive Surgical Inc. 32

2.3 Single-port Surgical System from Samsung Electronics @2015 Samsung Electronics 33

2.4 SPORT Surgical System from Titan Medical Inc.; (left) patient-side cart with surgical tools, and (right) surgeon's console. @2017 Titan Medical Inc. 34

2.5 Surgibot, single-access surgical robot from TransEnterix; (left) robotic interface with a surgical port and tools, and (right) system controller and endoscope vision stack. @2014 TransEnterix 34

2.6 Single-port Surgical Robot (Kobayashi *et al.*) [1] 35

3.1 Richard Wolf instrument set for TEM. 47

3.2 Overview and operation of the Hamlyn Lightweight Robot Arm. The arm is attached to the operating table at the patient's leg end of the table. 48

3.3 Dimensions and motion ranges of the Hamlyn Lightweight Robot Arm. 49

3.4 Components inside the Hamlyn Lightweight Robot Arm. . . . 49

3.5 Exploded view of each rotational joint inside the Hamlyn Lightweight Robot Arm. 50

3.6 Experiment setup for the measurement of structural stiffness of the Hamlyn Lightweight Robot Arm. 52

3.7 Configurations of the arm that the tests were performed on. . 53

3.8 *In vivo* human trial of the Hamlyn Lightweight Robot Arm. . 54
3.9 3D rendering of the Hamlyn Lightweight Robot Arm based on the position tracking data from the absolute encoders inside the arm during the clinical trial. 55

4.1 Different methods of using force/torque sensors to implement hands-on cooperative manipulation on an articulated robot arm. 59
4.2 The Hamlyn Active Arm with an endoscopic instrument attached. Its axes of rotation are shown in dashed lines. 62
4.3 Internal components of a 2-axis sub-assembly of the Hamlyn Active Arm. 63
4.4 An example showing an end effector of an articulated robot with a tool and a force sensor mounted for hands-on positioning. 64
4.5 Block diagram of the control software for the hands-on positioning function. 65
4.6 Pseudo-*null*-space mapping. Maintenance of a reference end effector pose while rotating its base joint. Background image: reference configuration. 68
4.7 System components: A) KUKA LWR4+, B) KUKA LBR iiwa,
C) ATI Mini40, D) Tool, E) Tube, F) Adjustable weights . . 71
4.8 Experiment setup showing initial tool position P_0, tool entry position P_1, and tool exit position P_2 72
4.9 Recorded tool tip positions from all participants from all trials during the experiment 4.5.1. The points are evenly sampled from the continuous trajectories. 73
4.10 Comparison of user manipulation force 74
4.11 Experiment setup for targeting and reconfiguration tasks . . . 75
4.12 Examples of collected data from experimental tasks with different operation modes. 76
4.13 Results from reconfiguration experiments 78

5.1 Cyton Alpha 7D 1G robotic arm by Robai. It has 7 degrees of freedom (DoFs) with a gripper. 82

5.2 The circuit board assembly of the customised servo motor for the robotic arm. The yellow circle indicates the location of the accelerometer. The axes illustrate the alignment of the sensor's coordinate frame. 83
5.3 Acceleration signals of the arm's end effector showing hard collisions (with wooden table) and general collision (with finger) along with an arm movement 84
5.4 Parameters of a collision signal in k^{th} axis: Magnitude A_k, Baseline Acceleration B_k, Amplitude Threshold $\pm Tm_k$, and Time Threshold Tt_k 84
5.5 Acceleration signals for collisions from different materials used in experiments 89
5.6 Material classification pipeline. 90
5.7 The experiment setup using *Cyton Alpha 7D 1G* robotic arm and a solenoid with interchangeable hardness tips (showing the white tip in enlarged image). The arm is divided into 6 links (L0-L5) for the purpose of location identification of collisions. 94
5.8 Solenoid tip materials, showing material M_1, M_2, M_3, M_4 respectively 94
5.9 Collision sequence captured at 4000 frames/sec, this entire sequence takes 15 milliseconds 95
5.10 Experiment setups of environment exploration, Scenario 1: arm in an empty box, Scenario 2: an obstacle is added into the box 96
5.11 Collision detection and estimations accuracy for each robot's link corresponding to Fig. 5.7 98
5.12 Object identification accuracy 99
5.13 Exploration results viewed from different angles, top plots show the 1^{st} scenario, bottom plots show the 2^{nd} scenario, axes are in millimetres 101
5.14 Exploration experiment image sequence, scenario 1 102
5.15 Exploration experiment image sequence, scenario 2 102

6.1 Hamlyn Active Arm with a micro-scanning robotic tool. . . . 105

6.2 Micro-scanning robotic tool with an endomicroscopy probe inside the working channel. 107
6.3 Dexterity of the manipulator with the scanning probe within the reachable workspace calculated using the dexterity measure $\mathcal{D}$ in (6.9). 110
6.4 Placement of the microscopy probe and the force/torque sensor at the end effector. A tool coordinate system is defined at the tip. 110
6.5 Architecture of the 3-DoF force and orientation controller. . . 111
6.6 Calibration of the probe offset weight in different sensor axes (F_x,τ_y,τ_z) due to orientation changes. The black dots represent the measurement from the force/torque sensor using preprogrammed trajectory with five repetitions. The fitted models are shown with coloured surfaces. 114
6.7 Comparison of the measured force, modelled probe weight, and the corrected force F_x during orientation changes. 115
6.8 Step response from the contact force controller on a tissue sample, showing the desired contact force, the measured force, and their difference. 116
6.9 Experimental setups of the line scanning microscopy on a porcine tissue with a spherical surface. 118
6.10 Comparison of the normalised cross-correlation (NCC) values from the mosaicking process between different control schemes applied during scanning. 119
6.11 Comparison of mosaicking results from endomicroscopy scanning with different control schemes. 120
6.12 Comparison of responses from the contact force controller on a moving tissue sample at different speeds. The setpoint is at 50 mN. 120

7.1 Different viewpoints of the proposed master manipulator. . . 123
7.2 Joint control mapping of (a) the highly articulated robotic instrument to (b) the master manipulator. The corresponding axes of rotation and translation are shown. 124

7.3 Rotational axes of the articulated sections of the slave instrument, and the corresponding axes on the master manipulator (for simplification, some components are not shown). 125
7.4 Master manipulator's finger grips design; (a) operator while manipulating the finger grips, (b) computer-aided design (CAD) rendering of the finger grips, and (c) exploded view presenting the magnet and the Hall effect sensor for position sensing and the integrated force sensor to facilitate the manipulator's motion. 128
7.5 Distance-voltage data collected from an experiment, 42 data points in total. 129
7.6 Grip angle sensor 129
7.7 Different linkage designs for the mapping of the dependent joints; (a) gear-based design, (b) tendon-based design, and (c) currently implemented four-bar linkage design. 130
7.8 Parameter optimisation of the four bar mechanism. a.) parameter definition of the mechanism. b.) blue: relation between angle θ and link-length a, red: angular error ϵ as function of θ. 131
7.9 Dexterous workspace $\mathcal{D}_{\mathcal{V}}$ of the master manipulators and the highly articulated instrument. 133
7.10 Diagram of the control system for the master manipulator. Four terms that contribute to the output torques; τ_L, τ_G, τ_D, τ_F; are calculated by the software on the host computer. . . . 135
7.11 Experimental setup of the usability study, presenting (a) the operator manipulating the highly articulated instrument through the three-dimensional (3D) display while performing the peg transfer task, and (b) the slave robotic system for single-access robotic surgery. 138
7.12 Structure and a peg for the insertion task, showing five different locations of the holes and the rubber peg. 139
7.13 Telemanipulation of the highly articulated surgical instrument with the master manipulator. The top right corner of each image shows a view from the endoscope. 140

7.14 Comparison of manipulation force and the movement of the *translation* stage in implementations with and without the friction and gravity compensations. (see Fig. 7.2 for the reference of axis names) 141
7.15 Comparison of manipulation torque and the movement of the *roll* joint in implementations with and without the friction and gravity compensations. (see Fig. 7.2 for the reference of axis names) 142
7.16 Task execution times between the master manipulators. The mean values are indicated by the circles. 142
7.17 One handed preliminary suture test. The top right corner of each image shows a view from the endoscope. 144

List of Acronyms

1D One-dimensional.

2D Two-dimensional.

3D Three-dimensional.

AC/DC Alternating Current to Direct Current.

CAD Computer-aided Design.

CAN Controller Area Network.

CE Conformité Européene (European Conformity).

CoM Centre of Mass.

DAQ Data Acquisition.

DC Direct Current.

DLS Damped Least Squares.

DoF Degree of Freedom.

ENT Ear, Nose, and Throat.

FDA Food and Drug Administration.

FoV Field of View.

GI Gastrointestinal.

IGES Image-Guided Endoluminal Surgery.

IIR Infinite Impulse Response.

MEMS Microelectromechanical Systems.

MIS Minimally Invasive Surgery.

NA Not Available.

NCC Normalised Cross-correlation.

NOTES Natural Orifice Transluminal Endoscopic Surgery.

PCIe Peripheral Component Interconnect Express.

PID Proportional-Integral-Derivative.

RMSE Root-Mean-Square Error.

SVM Support Vector Machine.

TDOA Time Difference of Arrival.

TEM Transanal Endoscopic Microsurgery.

WYSIWYG What You See Is What You Get.

1 Introduction

Colorectal cancer is the third most commonly diagnosed malignancy and the fourth leading cause of cancer-related death globally [2]. Currently, one third of the cancerous lesions identified tend to be early stage tumours and are, in those accessible, suitable for local transanal excision over conventional open surgery without compromising the oncological treatment. Transanal Endoscopic Microsurgery (TEM) is a technique for the safe and effective excision of early stage tumours and high-grade adenomas, the benign precursors to malignancy, within the rectum and rectosigmoid. The approach, in essence, is a *single-access surgery*. However, operating within a narrow space through a single-port using rigid pre-bent laparoscopic instruments, as is the case with the TEM approach, is highly challenging and limits its potential. Many of the challenges with this single-port technique are ergonomic in nature and well-described. Of particular note is the limited external workspace available to the operator, restricting their ability to triangulate the instruments and perform dexterous manipulation. Other limitations include the fulcrum effect, which describes the inversion of the instrument's movements relative to the surgeon's hand motion. In addition, the tool leverage that occurs within the port can lead to the inaccurate representation of forces applied to the tissue.

Robotic surgery has been a domain of intense research activity in recent years [3, 4]. Robotic-assisted surgery presents important benefits over the conventional approach, such as providing a high-definition visualisation system and enhanced dexterity. A robotic system can overcome aforementioned challenges of TEM with the potential of treating even more patients in a minimally invasive way, more effectively and potentially with lower risk.

Intuitive Surgical's da Vinci Surgical System (Sunnyvale, CA, USA) is the leading surgical robot used in several operation types, such as urology, gynaecology and general surgery. The system provides three-dimensional (3D) stereoscopic vision and high dexterity to control the surgical instruments at the tip of the robot. However, force feedback resulting from the interaction between the instruments and tissues is neglected and surgeons utilising this system rely on only visual cues [5]. It has been shown that force feedback enhances performance in robotic surgery [6, 7, 8, 9]. The employment of a tele-operated robotic system removes the direct contact of hands with tissues and, thus, diminishes the sense of touch. All information about the patient is given to surgeons only through the visual sense. This enforces that surgeons exclusively rely on visual cues, compromising patient safety and telepresence. From the surgeons' perspective, force feedback plays a crucial role in intuitiveness and patient safety [10]. However, up to now, the potential of force feedback in robotic surgery has not yet been fully exploited, and therefore, this application still represents a fascinating research field.

Currently, the only commercially-available robotic platform for single-access surgery is the da Vinci Single-Site [11]. It is, however, not suitable for surgeries within a confined space like that involved with TEM. The recently-introduced da Vinci Sp system [12] received FDA 510(k) clearance in 2014 initially for urological procedures that are suitable for single-access surgery and is expected to be available on the market soon.

This thesis seeks to present the use of robotic manipulators for enhancing the precision and workflow of a single-access surgery, TEM in particular. It proposes solutions to some of the challenges that will enable single-access surgery to be successfully performed. A portion of the work presented in this thesis is part of a novel robotic platform, entitled *Micro-IGES*, which is appropriate for performing complex surgical tasks in TEM while improving the precision of operation and ergonomics for the surgeon. Publications on this system include: *surgical system and clinical studies* [13, 14], *surgical instrument* [15, 16], *control system and algorithms* [17, 18], and *support arm* [19, 20, 21].

In **Chapter 2**, a detailed review of robotic systems suitable for single-access surgery is presented. It covers several works and devices related to that presented herein.

In **Chapter 3**, an articulated global positioning robot that functions as a docking platform for instrumentation in single-access surgery is presented.

It is based on a passive mechanism realising a lightweight design and high-payload capability. The design, component selection, and corresponding workspace analysis are described. The embedded sensors allow not only the instrument pose to be known, but also the estimation of the contact forces to be carried out. Additionally, the results from clinical studies are presented.

In **Chapter 4**, another embodiment of a docking platform for instrumentation for single-access surgery is put forth. This is another iteration of a surgical tool holder that enables *hands-on reconfiguration*, rendering the placement of the arm more flexible and optimised for the reduced workspace on the operating table.

In **Chapter 5**, a method allowing a robotic manipulator to detect collisions with environments is described. By analysing the characteristics of the vibration captured with a high-bandwidth accelerometer, the hardness of the material can be identified. The method is then extended to an environment-mapping application as an example use case.

In **Chapter 6**, a robotic-assisted endomicroscopy system employing an arm introduced in the previous chapter is reported. It proposes a novel *in-situ*, *in-vivo* optical biopsy system which practically allows clinicians to *point and scan* target tissues with large area image acquisition via automatic mosaicking. It enables real-time tumour biopsies, a technique which could only be carried out via post-processing time-consuming histopathology examinations.

In **Chapter 7**, a master manipulator optimised for a type of surgical instrument is presented. It operates via a different concept in terms of how a highly articulated surgical instrument can be telemanipulated with a kinematically identical manipulator via joint-space mapping as opposed to the conventional task-space mapping. This design potentially gives more transparency and intuitiveness to the surgeon as he/she has control over the entire shape of the surgical tool.

1.1 Contributions

All the technical chapters (3–7) in this thesis are results of work carried out by a group of researchers. The following lists summarise the technical contributions of various sub-tasks for each chapter. Items in **bold** are sole contributions from the *author*.

1. Chapter 3
   Articulated Dock with Passive Joints for Surgical Instruments
   Overall contributions: 50% by *author*, 50% by *Jindong Liu*

   - Mechanical design: by *Jindong Liu*
   - Component selection: 20% by *author*, 80% by *Jindong Liu*
   - **Electronics**
   - **Communications**
   - Position sensing: 50% by *author*, 50% by *Jindong Liu*
   - Characterisation: 50% by *author*, 50% by *Jindong Liu*
   - EMC tests and medical certification: 20% by *author*, 80% by *Jindong Liu*
   - Clinical trals: 20% by *author*, 80% by *Jindong Liu*

2. Chapters 4 and 6
   Articulated Robotic Manipulator for Surgical Applications and *Three-dimensional Robotic-assisted Endomicroscopy with a Force Adaptive Robotic Manipulator.*
   Overall contributions: 80% by *author*, 20% by others

   - Mechanical design: 90% by *Jindong Liu*, 10% by *Petros Giataganas*
   - Workspace analysis: by *Konrad Leibrandt*
   - **Component selection**
   - **Electronics**
   - **Communications and control system**
   - Inverse kinematics: by *Konrad Leibrandt*
   - **Integration with force/torque sensor**
   - Endomicroscopy: by *Petros Giataganas* and *Michael Hughes*

3. Chapter 5
   Collision Detection and Object Characterisation with Robotic Manipulators.
   Overall contributions: 100% by *author*

4. Chapter 7
   Master Manipulator for Teleoperation of Single Access Surgical Instruments.
   Overall contributions: 90% by *author*, 10% by others
   - **Mechanical designs – rotational joints and finger grips**
   - Mechanical design – translation stage: by *Petros Giataganas*
   - Geometric and workspace analyses: by *Konrad Leibrandt*
   - **Component selection**
   - **Electronics**
   - **Communications and control system**
   - **Integration with force/torque sensor**
   - Integration with slave robotic instrument: 50% by *author*, 50% by *Gauthier Gras*

1.2 Research Contributions

The key novelties of this work *e.g.* designs, implementations, solution to unsolved problems; can be summarised as follows:

1. Chapter 3
   Articulated Dock with Passive Joints for Surgical Instruments
   - Absolute rotary encoder:
     The use of novel multi-pole magnet ring with perpendicular pole configuration which is more compact compared to conventional radial ring magnets.
   - Torque multiplication using harmonic gearing:
     The use of passive locking mechanism (eletromechanical brake) coupled with transmission system (harmonic gearing) provides instantaneous locking/releasing function for an articulated clamp. The inherent backdrive friction of harmonic gearing is beneficial for prevention of sudden movements during operation.
   - Torque estimation:
     Harmonic gearing has a small degree of flexibility which can be measured by a high resolution encoder. A relative torque of the

joint can be estimated from the torsion of the transmission system while the brake is locked.

2. Chapter 4
   Hamlyn Active Arm – Articulated Robotic Manipulator for Surgical Applications
   - Small lightweight robotic arm with fully integrated controller:
     The robotic arm employs brushless motors with harmonic gears to achieve high payload capability while maintaining zero-backlash and low weight (3 kg weight, 1.5 kg payload). The integrated electronics reduces the cabling and footprint of the overall system.
   - Calibration-free force control:
     Integrated force sensitive handle provides a means for user to manually manipulate the tool directly. The arm utilises a force sensor that is mounted independently from the surgical tool, enabling arbitrary tools to be used or exchanged without requiring tool mass parameters calibration. Furthermore, a gravity compensation is also achieved with this method.
   - Kinematic reconfiguration:
     Although the kinematics of the arm has limited redundancy, its control system allows “hands-on” reconfiguration that moves the joints in a semi-null-space motion. This ensures surgical tool placement and positioning is more flexible and less cluttered on the operating table.
3. Chapter 5
   Collision Detection and Object Characterisation with Robotic Manipulators
   - Low-cost on-board collision detection:
     The system detects and analyses vibration signals measured from on-board Microelectromechanical Systems (MEMS) accelerometers fitted inside the actuators.
   - Characterisation of object material from impact:
     Using signal-processing techniques, four different levels of material stiffness can be identified. Additionally, the location, magnitude, and direction of the impact can be estimated.

4. Chapter 6
   Robotic-assisted Endomicroscopy with Hamlyn Active Arm
   - Semi-automatic control:
     The system features robotic-assisted wide-area microscopy imaging that allows user to arbitrarily navigate the imaging probe to the desired scanning area using a joystick. While scanning, the robot autonomously adapts to any uneven surface by adjusting the probe to ensure robust microscopy image acquisition.
   - 3-DoF force adaptation:
     The sensing system allows adaptation of the imaging probe to achieve maximum image quality by maintaining not only the axial contact force, but also the perpendicular orientation to uneven tissue surfaces.

5. Chapter 7
   Master Manipulator for Teleoperation of Single Access Surgical Instruments
   - Instrument-specific master device with joint mapping control:
     The design is kinematically identical to the surgical instrument, allowing a direct joint-mapping control scheme. The direct correspondence of the structure between the master interface and slave instrument makes the device intuitive when operating. This effectively removes the need for a clutching mechanism (a temporary disengagement of teleoperation to allow repositioning of master device) commonly integrated into master interfaces that do not match the workspaces of the slave device. The direct mapping scheme also facilitates direct joint limit rendering and velocity damping without the need for inverse kinematic solutions.
   - Dependent joint coupling design:
     The four-bar linkage design to emulate the dependent joint is simple to build and provides high stability compared to other conventional transmission systems.
   - Feedforward gravity and friction compensation
     The use of 6-degree of freedom (DoF) force/torque sensor fitted inside the handle to compensate the effect of gravity and friction.

1.3 Publications

The work presented in this thesis were published in several international conferences, journals, and patents. These include the following publications:

Conference Proceedings

1. P. Triantafyllou, **P. Wisanuvej**, S. Giannarou, J. Liu, and G.-Z. Yang, "A Framework for Sensorless Tissue Motion Tracking in Robotic Endomicroscopy Scanning", in *IEEE International Conference on Robotics and Automation (ICRA)*, Brisbane, 2018, *in press*.

2. **P. Wisanuvej**, G. Gras, K. Leibrandt, P. Giataganas, J. Liu, and G.-Z. Yang, "Master Manipulator Designed for Highly Articulated Robotic Instruments in Single Access Surgery", in *IEEE/RSJ International Conference on Intelligent Robots and Systems (IROS)*", Vancouver, 2017, pp. 209–214.

3. C. A. Seneci, G. Gras, **P. Wisanuvej**, J. Shang, and G.-Z. Yang, "3D Printing of Improved Needle Grasping Instrument for Flexible Robotic Surgery", in *IEEE/RSJ International Conference on Intelligent Robots and Systems (IROS)*, Vancouver, 2017, pp. 2524–2530.

4. A. Schmitz, A. J. Thompson, P. B. Rayne, C. A. Seneci, **P. Wisanuvej**, and G.-Z. Yang, "Shape Sensing of Small Continuum Robots Using Optical Fibers", in *IEEE/RSJ International Conference on Intelligent Robots and Systems (IROS)*, Vancouver, 2017, pp. 947–952.

5. J. Liu, N. Penney, **P. Wisanuvej**, A. Darzi, and G.-Z. Yang, "A Case Study of a Passive Robotic Arm for Conventional Transanal Microsurgery", in *Hamlyn Symposium on Medical Robotics*, London, 2017, pp. 49–50.

6. **P. Wisanuvej**, P. Giataganas, K. Leibrandt, J. Liu, M. Hughes, and G.-Z. Yang, "Three-dimensional Robotic-assisted Endomicroscopy with a Force Adaptive Robotic Arm", in *IEEE International Conference on Robotics and Automation (ICRA)*, Singapore, 2017, pp. 2379–2384.

7. G. Gras, K. Leibrandt, **P. Wisanuvej**, P. Giataganas, C. A. Seneci, M. Ye, J. Shang, and G.-Z. Yang, "Implicit Gaze-Assisted Adaptive

Motion Scaling for Highly Articulated Instrument Manipulation", in *IEEE International Conference on Robotics and Automation (ICRA)*, Singapore, 2017, pp. 4233–4239.

8. **P. Wisanuvej**, K. Leibrandt, J. Liu, and G.-Z. Yang, "Hands-on reconfigurable robotic surgical instrument holder arm", in *IEEE/RSJ International Conference on Intelligent Robots and Systems (IROS)*, Daejeon, 2016, pp. 2471–2476.

9. C. A. Seneci, K. Leibrandt, **P. Wisanuvej**, J. Shang, and A. Darzi, "Design of a Smart 3D - printed Wristed Robotic Surgical Instrument with Embedded Force Sensing and Modularity," in *IEEE International Conference on Intelligent Robots and Systems (IROS)*, Hamburg, 2016, pp. 3677–3683.

10. **P. Wisanuvej**, J. Liu, K. Leibrandt, and G.-Z. Yang, "Calibration-free Gravity Compensation on Robotic Manipulators Using Tool-mounted Force Sensor", in *IEEE/RSJ International Conference on Intelligent Robots and Systems (IROS): Workshop on the Role of Human Sensorimotor Control in Surgical Robotics*, Hamburg, 2015.

11. **P. Wisanuvej**, J. Liu, K. Leibrandt, and G.-Z. Yang, "Calibration-free Gravity Compensation for Cooperative Manipulation", in *Hamlyn Symposium on Medical Robotics*, London, 2015.

12. **P. Wisanuvej**, J. Liu, C.-M. Chen, and G.-Z. Yang, "Blind Collision Detection and Obstacle Characterisation Using a Compliant Robotic Arm", in *IEEE International Conference on Robotics and Automation (ICRA)*, Hong Kong, 2014, pp. 2249–2254.

Journal Articles

1. P. Berthet-Rayne, G. Gras, K. Leibrandt, **P. Wisanuvej**, A. Schmitz, C. A. Seneci and G.-Z. Yang, "The i^2*Snake* Robotic Platform for Endoscopic Surgery", in *Annals of Biomedical Engineering*, 2018, *in press.*

2. P. Giataganas, M. Hughes, C. J. Payne, **P. Wisanuvej**, B. Temelkuran, and G.-Z. Yang, "Intraoperative robotic-assisted large-area high-

speed microscopic imaging and intervention", in *IEEE Transactions on Biomedical Engineering (TBME)*, 2018, *in press.*

3. K. Leibrandt, **P. Wisanuvej**, G. Gras, J. Shang, C. A. Seneci, P. Giataganas, V. Vitiello, A. Darzi, and G.-Z. Yang, "Effective Manipulation in Tight Spaces of Highly Articulated Robotic Instruments for Single Access Surgery, *IEEE Robotics and Automation Letters (RA-L)*, vol. 2, no. 3, pp. 1704–1711, 2017.

4. J. Shang, K. Leibrandt, P. Giataganas, V. Vitiello, C. A. Seneci, **P. Wisanuvej**, J. Liu, G. Gras, J. Clark, A. Darzi, and G.-Z. Yang, "A Single-Port Robotic System for Transanal Micro-Surgery—Design and Validation, *IEEE Robotics and Automation Letters (RA-L)*, vol. 2, no. 3, pp. 1510–1517, 2017.

Patents

1. G.-Z. Yang, J. Liu, and **P. Wisanuvej**, "Safety Device," UK Patent GB2554846A, April 18, 2018.

2. G.-Z. Yang, **P. Wisanuvej**, K. Leibrandt, C. A. Seneci, J. Shang, J. Liu, "Surgical instrument, robotic arm and control system for a robotic arm," International Patent WO2017203231A1, November 30, 2017.

3. G.-Z. Yang, **P. Wisanuvej**, C. A. Seneci, and K. Leibrandt, "Control system," UK Patent GB2550577A, November 29, 2017.

4. G.-Z. Yang and J. Liu, "Absolute rotary encoder," International Patent WO2016083825A1, June 2, 2016.*

*Author contributed to the systems engineering and implementation of the work, which are not part of the claims in the patent.

2 Background

2.1 Single Access Surgical Systems

While single-access surgery has been explored extensively the only robotic platform for single-access surgery currently on the market is the da Vinci Single-Site, shown in Fig. 2.1 [11]. It features two semi-rigid instruments inserted through two curved cannulae crossing each other at the port entry point to provide triangulation. This configuration is however not suitable for surgeries within a confined space like TEM. The da Vinci Sp system, shown in Fig. 2.2 [12], incorporates three 6 mm, 7 DoFs surgical tools and a stereo camera inserted through a single port. All the instruments and camera are straight during insertion to fit in the 25 mm surgical port. Once the instruments and camera are inserted, they can be reconfigured to provide off-axis camera view and instrument triangulation. The da Vinci Sp system received FDA 510(k) clearance in 2014 initially for urological procedures that are suitable for single-access surgery and is expected to be available on the market soon.

Similarly, the single-port surgical system developed by Samsung Electronics, shown in Fig. 2.3 [22] features a 6-DoF guide tube, two 7-DoF surgical tools, and a 3-DoF stereo-endoscope. The 30 mm diameter guide tube consists of two 2-DoF segments with variable stiffness rolling joints and has sufficient flexibility to reach a surgical target in an arbitrary pose within the abdomen. The multi-DoF instruments can cover 250 mm(W) x 200 mm(H) x 200 mm(D) space. The SPORT (Single Port Orifice Robotic Technology) Surgical System (Titan Medical Inc. Toronto, Canada), Fig. 2.4, is based on the IREP system [23] that has two multi-DoF continuum arms and a 3-DoF stereo camera. The system can pass through a 15 mm port and covers a large workspace of 64 mm x 103 mm. The SurgiBot by TransEnterix Inc. (Morrisville, NC), Fig. 2.5, is another single-access surgical robot based on the manual SPIDER system shown in Fig. 2.5 [24]. Studies on simulators

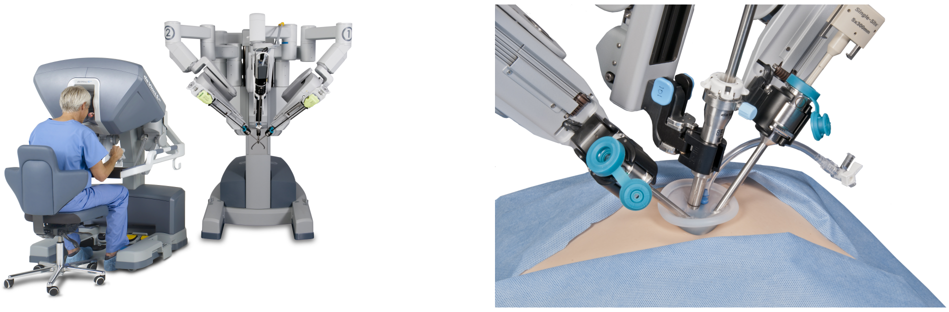

(a) surgeon's console and patient-side cart

(b) Single-Site Instrumentation

Figure 2.1: da Vinci Si with Single-Site Instrumentation robotic system from Intuitive Surgical. @2011 Intuitive Surgical Inc.

Figure 2.2: da Vinci Sp robotic system from Intuitive Surgical; (left) patient-side cart with a surgical port and 4 robotic tools, (centre) vision stack and (right) surgeon's console. @2014 Intuitive Surgical Inc.

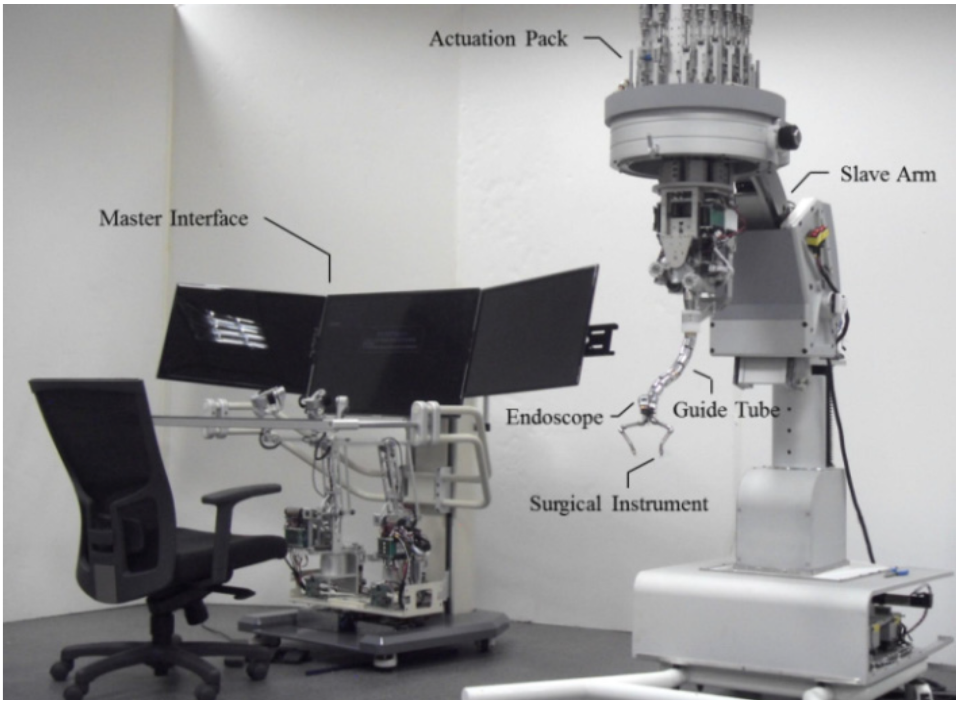

Figure 2.3: Single-port Surgical System from Samsung Electronics @2015 Samsung Electronics

presented that to use the SPIDER system is more challenging compared to the conventional multiport laparoscopic surgery approach [25]. The robotic version of this system is set to improve the shortcomings of the manual system.

Researchers from Waseda University (Kobayashi *et al.*), Japan, developed a master-slave single-port surgical robot that has a 25 mm flexible shaft, two 8 mm 6-DoF instruments, and a camera that can be manipulated to adjust the field of view [1]. Another multitasking robotic platform for single-port access surgery is presented in [26]. This system incorporates two continuum arms with surgical instruments and a 3-DoF "head" for manipulating the camera and an additional instrument. A common drawback of all these systems is that they are mainly designed for operation within the abdominal cavity. The configuration of the camera and the size of the instruments therefore prevents their deployment within such a narrow and confined space as the rectum.

A number of devices targeting flexible access applications for Natural Ori-

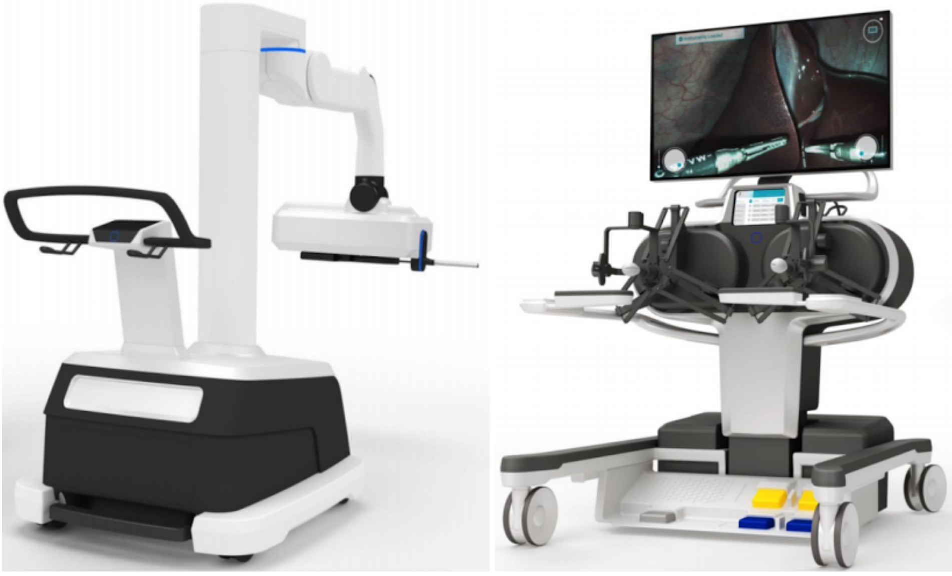

Figure 2.4: SPORT Surgical System from Titan Medical Inc.; (left) patient-side cart with surgical tools, and (right) surgeon's console. @2017 Titan Medical Inc.

Figure 2.5: Surgibot, single-access surgical robot from TransEnterix; (left) robotic interface with a surgical port and tools, and (right) system controller and endoscope vision stack. @2014 TransEnterix

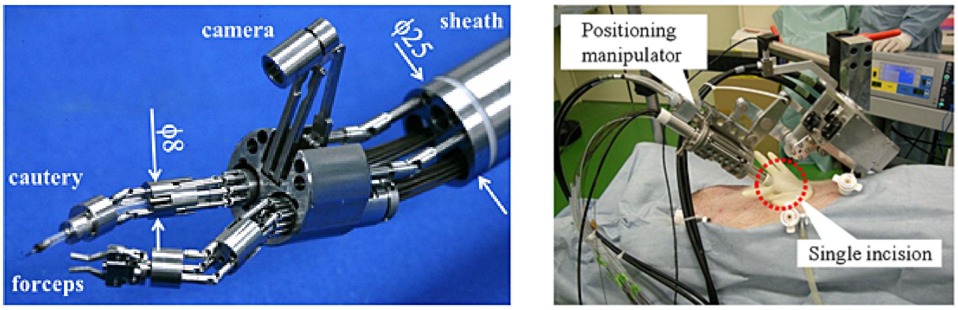

(a) Surgical Instruments (b) Patient-side Robot

Figure 2.6: Single-port Surgical Robot (Kobayashi *et al.*) [1]

fice Transluminal Endoscopic Surgery (NOTES) have surgical instruments integrated at the front of flexible endoscopes, such as the ANUBISCOPE (iCUBE STRAS) robot developed at IRCAD-Strasbourg, that is based on the Karl Storz Anubis system, the R-scope and Endo-Samurai by Olympus. A review of such flexible access NOTES systems can be found in [3]. Although promising, these systems still lack adequate stability, triangulation and force exertion capabilities to carry out complex tissue manipulation, as required during TEM.

2.2 Robotic Assisted Surgical Tool Holders

Many surgical procedures require tools to hold and maintain instruments or part of the patient body in position while the surgeon performs surgical tasks. In general, the instrument holders are made in the form of an articulated arm where one side is mounted to a fixed foundation. The arm has a control knob or lever to lock the joints in place. Examples of such holder arms include: Martin Arm System (KLS Martin Group, Germany), TEM Instrument Support Arm (Richard Wolf, Germany), Mayfield Head Clamp (Integra LifeSciences, USA). These arms are purely mechanical-based for ease of construction, robustness, and sterilisability. However, due to the lack of weight compensation, the operator has to carry both the weight of the tool and its payload which makes it difficult to be manoeuvred safely. An assistant is usually required when operating the mechanical holding arms.

Some holder arm systems use an electronic locking mechanism to reduce the time required to release and lock the joints. Such systems include Point Setter (Mitaka, Japan), EndoTAIX (SurgiTAIX AG, Germany). Although these devices are more convenient to use due to instant locking/releasing mechanism, they are still not weight compensated. There are several commercial robotic systems for tool holding with weight compensation in surgical applications, but they are usually integrated with the instrument system which is not suitable for general purpose usage.

With increasing maturity of compliant robotic arms, they are used extensively in human environments such as healthcare, rehabilitation, surgery, and social humanoid robots [27].

One of the approaches applied to robots in human environment is cooperative manipulation concept where both the robot and the operator manipulate the same tool by physical contact with the robotic arm. It is also termed as "hands-on" manipulation. Such a design has been used in industry to shorten the programming time to certain tasks. For instance, Robotiq proposed "Kinetiq Teaching" technology [28] to quickly program welding trajectories by hand guiding the robotic arm. Rethink robotics designed Baxter robot which can be taught to do pick-and-place tasks by hand guidance. KUKA and DLR produced the light-weight robot (LWR) arm for collaborative control in which the operator can guide the robot by manipulating the robot arm directly. In other robotic fields, Taylor [29, 30, 31] proposed the "Steady-Hand" robotic system to provide smooth and precise positional control of a hand-held surgical instrument in retinal microsurgery. A hip replacement surgical robot, Robodoc® [32], has been used for autonomous milling of bones. Davies proposed a hands-on Acrobot together with Active-Constriant concept for orthopaedic surgery [33]. Barrett WAM [34] robotic arm has been applied in upper limb stroke rehabilitation in which the patient can drag the end effector of the arm to exercise. DLR also proposed the MiroSurge system [35] with hands-on endoscopic instruments control capability.

Robotic arms designed to operate in a complex or dynamic environment often have redundant kinematic configurations, i.e. the robot has more degrees of freedom than necessary, in order to avoid obstacles [36, 37], prevent overturns [38], or tolerate joint failures [39], etc. Particularly, 7-DoF articulated robot arms have been widely used for manipulating objects in 6-DoF space. One common task for redundant robotic arms is to perform a null-space motion with one joint being kept stationary, particularly to keep the end effector static while allowing configuration changes to comply with the surrounding environment. In some situations, however, the number of joints in a robotic arm are limited to six or lower, such as when joint failure occurs or with limited space. It is an impossible job for these non-redundant robotic arms to perform the same null-space motion as the redundant arms. Nevertheless, it is feasible to have redundant-like motion i.e. self-motion of the joints if the end effector pose is allowed to move slightly. Six-DoF robots with redundant-like motion can be as beneficial as those redundant robots when the task requirements permit some degree of inaccuracy.

2.3 Safe Robotic Manipulators working in Human Environment

Research in compliant robots working safely in human environment is an increasingly popular research topic because of the wide range of applications under development. These cover human-robot cooperation, learning-from-demonstration, and rehabilitation and healthcare applications. The robot designed to work with human interaction must be able to operate safely and cause no harm to human or damage to properties. In particular, avoiding collision is one of the crucial components for safe robot operation. Typically, this requires vision- or laser-based perception systems. Occlusion in the field of view or very fast movement can cause visual based collision avoidance to fail. The use of integrated sensors for collision detection has many advantages, which can also complement the commonly used vision sensor to improve the overall sensitivity and robustness of the robot.

Thus far, extensive research has been carried out for equipping a robot manipulator with low-level sensors to ensure safe operation. By observing joint position and commanded joint torque, collision detection can be achieved without additional sensors [40, 41, 42]. However, this requires calculations of robot dynamics. Therefore, the method requires complex structural analysis of the robotic arm. Another detection system based on current sensing eliminates the needs of structural analysis and dynamics calculations [43]. However, the method still suffers from the drawback that it only works when the arm is moving and there is no sense of localisation of the collision point.

An alternative method achieves collision detection in a quadruped mobile robot by using an accelerometer to monitor the robot movement [44]. The statistical analysis of the signal in frequency domain enables the collision events to be detected. However, location, magnitude, and direction information of the impact are not detected.

In addition to the collision detection, being able to identify obstacle characteristics is also important in practice. The robot controller can store the object location as a static obstacle and navigate around it in subsequent motion planning. On the other hand, collision with a human could be considered as a dynamic obstacle. A robot may temporarily remember the collision point and avoid that with a certain safety distance.

We all know that humans can sense the hardness of an object by tapping [45]. In the same way, research in object identification also relied on tapping with robotic arm/hand with the obstacles. By capturing the vibration signal with an accelerometer, tapping different objects can produce different vibration patterns [46, 47, 48, 49]. As an example, a legged robot has been proposed, which can identify its walking surface from accelerometer data analysis with machine learning [50]. Despite its high accuracy in surface prediction, this method is based on a walking robot. The signal pattern is different from tapping signals, and thus cannot be used directly to perform object recognition. In addition to tactile sensing, other sensory feedback can also be used. By analysing contact sound from a robotic manipulator, the object material can also be identified [51, 52, 53]. Furthermore, object identification can be achieved by characterising its thermal property using a robotic manipulator with heat/thermal sensors [54].

By attaching sensors onto the robotic manipulators, environment exploration can be realised. Although contact-less approaches using laser range scanner [55] or time-of-flight camera [56] are commonly used, they require complex hardware/software integration. Currently, some approaches using tactile based sensors are being proposed. For example, a robot hand with 256-point piezoresistive sensor array can provide high spatial resolution for contact object identification [57]. Another method is to use a robotic arm with an optical waveguide tactile sensor to identify characteristic features on test objects [58].

2.4 Robotic-Assisted Endomicroscopy Systems

In cancer surgery, there is an increasing demand for intraoperative tissue assessment and tumour margin identification. Histopathological examination is still the "gold standard" but is a discrete, invasive process and the results are available typically in 1-2 weeks after the operation. Other techniques, such as cryosection, assist in generating the results sooner but they are still not real-time as they take a significant amount of operating time to be prepared. Usually, it takes more than 20 minutes, and suffers from reliability issues due to freezing artefacts. Advances in fibre optic technology, miniaturised optics and mechanics enable the acquisition of high resolution images at a cellular level *in vivo* and *in situ*, a process known as optical biopsy. Optical biopsy techniques, such as confocal laser endomicroscopy [59], and endocytoscopy [60] combined with flexible endoscopes or minimally invasive surgical instruments provide *in vivo* real-time morphological details about the tissue under examination.

These probe-based endomicroscopes present several significant limitations that hinder their clinical adoption. Manipulating these miniature fibre bundles (typically $< 3\,\text{mm}$) with a manual instrument is challenging, as well as maintaining sufficient contact while imaging within deformable tissue structures and cavities. This is amplified by the demand for wide surface area scanning as the interpretation of individual images is not adequate for histology-like assessment and tissue interpretation [61]. High-resolution fibre bundle endomicroscopes have a limited field of view (FoV) in the order of $240\,\mu\text{m}$, a size not comparable to large high-resolution histology images, making the surveillance of mm-scale areas challenging. Mosaicking techniques have been developed to increase the FoV of individual images, i.e. stitching adjacent image frames together as the probe moves across the tissue surface [62]. However, mosaicking is a partial solution to the effective scanning over large areas of complex tissue surfaces as the operator is required to maintain perpendicular probe pose and tissue contact while performing sub-millimetre scanning motions.

Robotic-assisted manipulation of the imaging probe has been explored recently to provide stable, precise, and consistent operation in comparison to manual manipulation [63]. Capabilities such as motion scaling, precise and tremor-free positioning, and advanced force sensing present robotic-assisted endomicroscopy as an ideal candidate to alleviate the limitations of endomicroscopic techniques and showcase the advantages of optical imaging in the operating theatre.

Initially, the importance of maintaining tissue contact to obtain good quality microscopic images was demonstrated in the early works of Latt *et al.* [64, 65] that developed handheld one DoF active force-controlled instruments. Load cells were used to sense forces applied axially to the tissue (distally [64] and proximally [65]) and linear actuation was used proximally to maintain consistent tissue contact at 100 mN (voice coil [64] and DC-servomotor [65]). Both works showcased the effects of forces on image quality of individual microscopic images, but not in terms of mosaicking or large area scanning. The latter was explored in the work of Giataganas *et al.* [66] where a cooperative robotic manipulator was used in conjunction with the 1-DoF force adaptive instrument from Latt *et al.* [65] to automatically generate large-area spiral mosaics. The quality, however, of the mosaics was limited as the instrument could only adapt to axial forces. Alternative to the active approaches, passive contact mechanisms were introduced. Giataganas *et al.* [67] developed a 1-DoF pick-up probe that can compensate for surface irregularities in robotic-assisted surgery using a pneumatic-based mechanism as an air bearing. Zuo *et al.* [68] employed a spring-based mechanism in the tip of a micro-scanning instrument and enhanced the stability further by integrating an inflatable outer balloon that stabilises the cavity structure under examination. These passive approaches demonstrated extended mosaicked areas but are limited in axial force compensation with non-linear spring-based mechanisms, while the use of balloon mechanism is limited to specific operations and dimensions. Another approach to generate local mm-scaled mosaics presented by Rosa *et al.* [69] incorporates a mechanical stabiliser on a micro-scanning tool to compensate for tissue motion and stabilise the surface under investigation. This simple and effective approach, however, increases the size of the instrument tip and is limited to local scanning since increased tissue deformation is introduced with the stabiliser. Finally, apart from bespoke instruments, the use of a large industrial robotic manipulator was explored by Rosa *et al.* [70] to build large area mosaics in flat 2D surfaces and study the tissue behaviour during endomicroscopic scanning.

2.5 Master Interfaces for Robotic Surgery

The goal of haptic technology in robot-assisted minimally invasive surgery is to provide 'transparency', in which the surgeon does not feel as if he is operating a remote mechanism, but rather that his own hands are contacting the patient. This requires artificial haptic sensors on the patient-side robot to acquire haptic information, and haptic displays to convey the information to the surgeon.

Haptic feedback systems for robotic surgery systems are still under development and evaluation. One commercially available teleoperated surgical robotic system with haptic feedback is the Sensei X Robotic Catheter System from Hansen Medical, Inc. (Mountain View, CA, USA). This robotic catheter system uses the 3-DoF omega.medical haptic device from Force Dimension to control the tip of the catheter. Force feedback information based on preoperative data is provided to the surgeon in real-time, while maintaining patient safety. Another is Senhance from TransEnterix (Morrisville, NC, USA), which is a teleoperated laparoscopic system. The system operation is based on the conventional laparoscopy, which aims to minimise the required training hours for the surgeons to make transition from a conventional procedure to a robotic one.

Force Dimension has recently developed the sigma.7 haptic device (Nyon, Switzerland) which is dedicated for medical applications. MiroSurge surgical robot from German Aerospace Centre (DLR) [71, 72] features two sigma.7 haptic devices which have force feedback in 7 DoFs including grasping.

There have been several efforts to restore the sense of touch when using the da Vinci system. For example, the VerroTouch [73] measures the impact caused by tool contacts inside patients and reproduces them at the level of the master handle. This feedback allows the surgeon to feel important tactile events such as rough surfaces as well as the beginning and the end of contact during manipulations. King et al. [6] developed a tactile feedback system to translate force distribution on the da Vinci surgical instruments to the fingers. In parallel to direct feedback, sensory substitution with imaging techniques is also proposed for restoring haptic feedback [74]. Nevertheless, this extra information should always be introduced carefully to avoid mental (or visual) overload.

2.5.1 Developments of Master Interface for Robotic Surgery

A widespread solution for the control of robotic surgical systems is to use a master-slave teleoperation paradigm, under which the operator's motions are relayed through a master device to the slave robot. This approach is particularly appealing in surgery, as it allows the user to benefit from robotic advantages such as motion scaling and tremor reduction, while retaining direct control over the robot motions.

A consequence of this paradigm is that the quality of a robotic system depends in large part on the quality of its master manipulator. An advanced slave system composed of highly dexterous instruments will ultimately not perform to its full potential if paired with an inadequate master system. To overcome this issue, a large number of systems opt to use master devices generating commands in task space. This allows such devices to be suitable for a large range of systems, while retaining an intuitive behaviour. Examples of master devices operating in task space include delta platforms such as the omega.7 and sigma.7 haptic devices (Force Dimension, Switzerland), or the master manipulator of the FLEXMIN system [75]. Other task-space master manipulators include serial-link devices such as the Geomagic Touch (Geomagic, USA), and the da Vinci surgical system master manipulator (Intuitive Surgical, USA).

While master manipulators operating in task space offer advantages in terms of generality and ease of use, their lack of specificity also present some disadvantages. In previous work [13], Shang *et al.* designed highly articulated surgical instruments with 7 DoFs for single-access surgery. An inverse kinematic control scheme was developed by Leibrandt *et al.* [18] to take advantage of the flexibility of the instruments, using two omega.7 devices as master manipulators. However, due to the mismatch between the master and slave workspaces, clutching mechanics had to be implemented, slowing down the user. Furthermore, the delta platform design of the master manipulator did not easily allow the user to perceive the joint motions and limits of the instruments. As the final joint positions are the result of the optimisation process of the inverse kinematic solver, this can lead to situations where the user is unaware of which joints have reached their limits and how to work around them to reach a specific goal.

As a result, the use of a device-specific master manipulator commanding the slave robot in joint space can be an attractive alternative. In [76], a master manipulator is presented for the control of a slave robotic device in joint space. However, the low number of DoFs used does not make it suitably scalable for the control of highly articulated surgical instruments. A number of joint-space master manipulators with a larger number of DoFs have been proposed, such as presented in [77], but do not possess active joints. This makes them unable to compensate for their own weight, or provide other forms of motion assistance. A master device with a high number of DoFs and active joints is presented in [78], but its delta structure prevents its use for the joint control of the instruments discussed. In [79] an exoskeleton-like robotic manipulator is placed on the human arm to control a surgical robot for gastrointestinal (GI) tract surgery. This passive system senses the joint-angles of the exoskeleton with rotary encoders, and hence cannot be gravity compensated or be used to give haptic feedback to the operator.

2.5.2 Commercial Haptic Interfaces

The specifications of the reviewed commercially available force feedback devices are summarised in Table 2.1. As shown in this table, not all the specifications are provided by the manufacturers. Although some specifications such as workspace and continuous force are common, important information on force resolution, transparency and frequency response characteristics is rarely provided.

2.6 Conclusions

Advances in mechatronics and computer science have enabled the development of a plethora of robotic-assisted surgical systems over the last few decades, setting new standards for surgery to be safer, more effective, and less invasive to the patients. These also enabled new operations to be performed with minimally invasive approaches, such as in single-access surgery.

In this chapter, a number of promising systems capable of performing a single-access surgery are discussed. One particular single-access surgical procedure, TEM, has been discussed and it will be featured as the main surgical procedure that this thesis will address. During the TEM procedure, the surgeon manipulates a heavy set of instruments via a mechanical clamp

Manufacturer	3D Systems		Novint	Force Dimension			Entact	Moog	CMU RI
Device	Phantom Omni	Phantom Premium	Falcon	delta.6	omega.7	sigma.7	W7D	Haptic Master	Maglev 200
Structure	Serial	Serial	Parallel	Parallel	Parallel	Parallel	Hybrid	Serial	
DoF (Total/Active)	6/3	6/6	3/3	6/3	6/3	6/6	6/6	3/3	6/6
Workspace (10^{-3} m^3)	1.3	199	1.1	32.6	2.2	3.7	3	80	0.01
Resolution (μm)	55	20	10	20	10	1.5	20	4	2
Peak Force (N)	3.3	22					4	250	40
Continuous Force (N)	0.9	3	9	20	12	20	1.4	100	
Stiffness (N/mm)	2	1	8	14.5	14.5		10	50	50
Friction (N)	0.26	0.2							0
Peak Torque (mNm)		188							
Continuous Torque (mNm)		48				400			
Bandwidth (kHz)				8	8	8	1		

Table 2.1: Manufacturer specifications of the commercially available haptic devices

inserted in the patient's body through a surgical port, resulting in imprecise movements, increased patient risks, and prolonged operating time. Several surgical tool holder designs to address the issue are discussed. These designs acted as the background work which led to the development, by the author of two robotic manipulators presented in Chapter 3 and Chapter 4.

Another clinical application that can benefit from having a precise surgical tool holder is optical biopsy and specifically the large-area endomicroscopy scanning. Advantages of intraoperative optical biopsy approaches over histopathological examination are discussed. Some related work using robotic manipulators to enhance the precision of real-time endomicroscopy imaging is presented. Some of these background works lack 3D surface adaptation capability. Other related works are hand-held robots which are not stable enough for such a precise microscopic imaging modality. Those issues lead to a development of a cooperative controlled robotic manipulator presented in Chapter 6.

One key aspect of any robotic manipulator working in an operating room, or any human environment, is the safety of its operation. Various different approaches of safety implementations in robotic manipulators are discussed. These are relevant research that led to the development of a blind collision detection method presented in Chapter 5.

Finally, most of the robotic manipulators mentioned earlier are designed to be manipulated directly, i.e. cooperative controlled. A different approach to this is telemanipulated robotics, where a slave robot is being controlled by the user moving a master interface. This paradigm is often used in surgical system as outlined in this chapter. Master interfaces for robotic surgery will be discussed in Chapter 7.

3 Articulated Dock with Passive Joints for Surgical Instruments[†]

3.1 Introduction

The local excision of lesions from within the rectal lumen using surgical platforms such as the Richard Wolf TEM system [80], shown in Fig. 3.1, offers a more stable and reliable method, as well as a much less invasive alternative for excising large benign lesions relative to radical excision of the rectum from within the pelvis via anterior or abdominoperineal excision. One of the challenges of TEM is to manipulate a heavy instrument set ($\sim$2 kg) including a rectoscope, surgical port, endoscope and two laparoscopic instruments. The current clinical solution is to apply a multi-linkage metal arm attached to the port that the surgeon can lock/unlock via a rotating knob. This is both inaccurate and time consuming, as the surgeon has to hold the instrument set in one hand while repeatedly loosening/tightening the lock with the other. To address these issues a lightweight robotic arm is developed, named the Hamlyn Lightweight Robot Arm, Fig. 3.2, for transanal microsurgery in order to help surgeons to position the port and its whole instrument set in an intuitive way. The versatile design of the arm allows it to be used for other procedures such as ear, nose, and throat (ENT) surgery as well. Comparing to the conventional supporting accessary, i.e. Martin's Arm [81], and other endoscope-holders [82], the Hamlyn Lightweight Robot Arm is ergonomically intuitive to operate with larger payload, greater stiffness and weight compensation. Four clinical trials in humans have been accomplished and the results show that the surgeon benefits from instant tool positioning, sufficient adjustment during lumen observation and firm

[†] Part of this chapter was initially presented at:
J. Liu, N. Penney, P. Wisanuvej, A. Darzi, and G.-Z. Yang, **A Case Study of a Passive Robotic Arm for Conventional Transanal Microsurgery**, in *Hamlyn Symposium on Medical Robotics*, London, 2017, pp. 49–50.

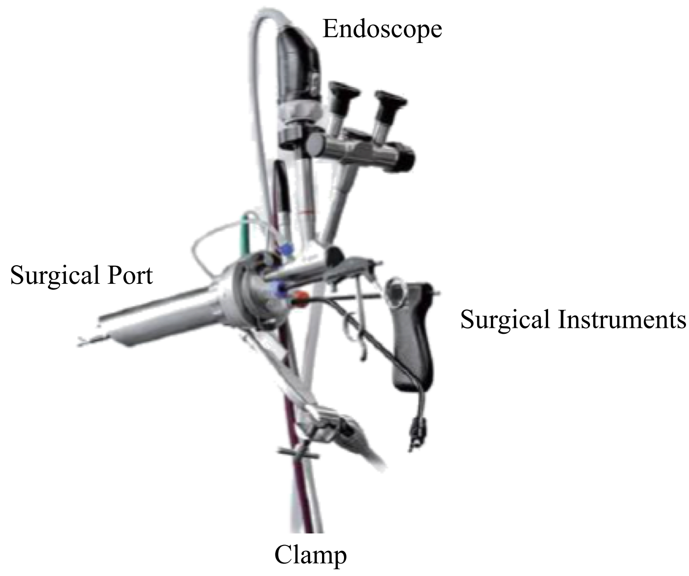

Figure 3.1: Richard Wolf instrument set for TEM.

tool locking.

3.2 Design

Fig. 3.2 illustrates an outline of the Hamlyn Lightweight Robot Arm and its intuitive operation method. The arm is a mechanical support which is designed to clamp onto a compatible operating table. The Richard Wolf TEM Port or other instruments can be fitted to the end of the device for use with conventional transanal surgery tools such as Wolf TEM tools with associated endoscopic equipment. It is designed with six joints to provide a large range of positioning movement. Fig. 3.3 illustrates the dimensions of the arm and its motion ranges.

The arm is electrically powered from a mains supply power outlet through a 24 V AC/DC power adaptor. The power supply controls an electromagnetic brake at each of the device's joints, locking all the joints in place when the control handle is released. For safety, two buttons are designed on the handle and the arm is activated only if both buttons are pressed. A counterbalance weight is designed so that the weight of the port and the arm is not a burden to the surgeon when manipulating the arm. The assembly

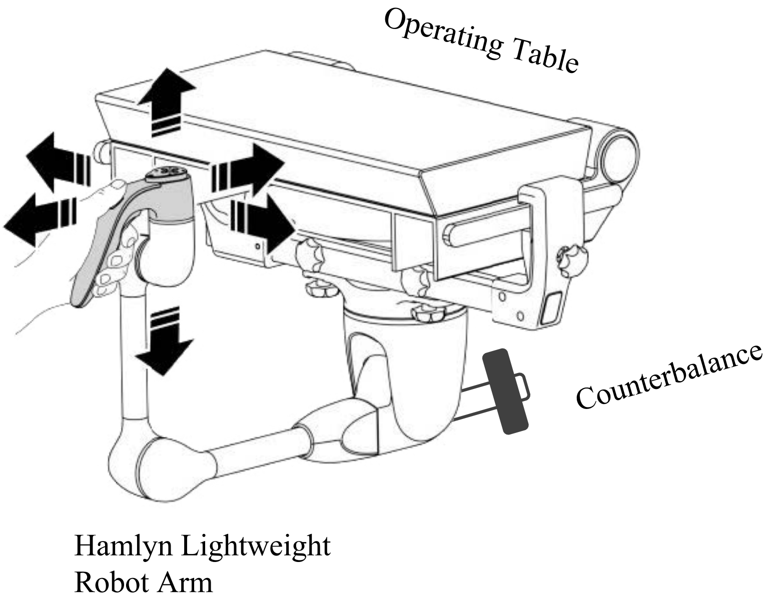

Figure 3.2: Overview and operation of the Hamlyn Lightweight Robot Arm. The arm is attached to the operating table at the patient's leg end of the table.

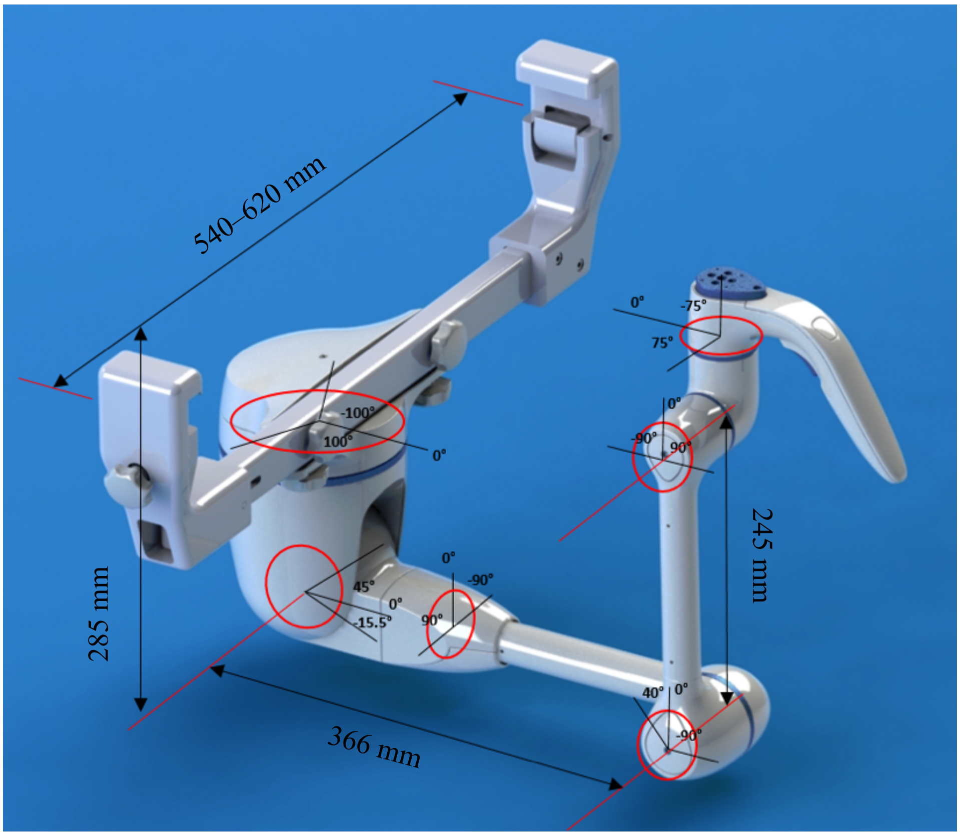

Figure 3.3: Dimensions and motion ranges of the Hamlyn Lightweight Robot Arm.

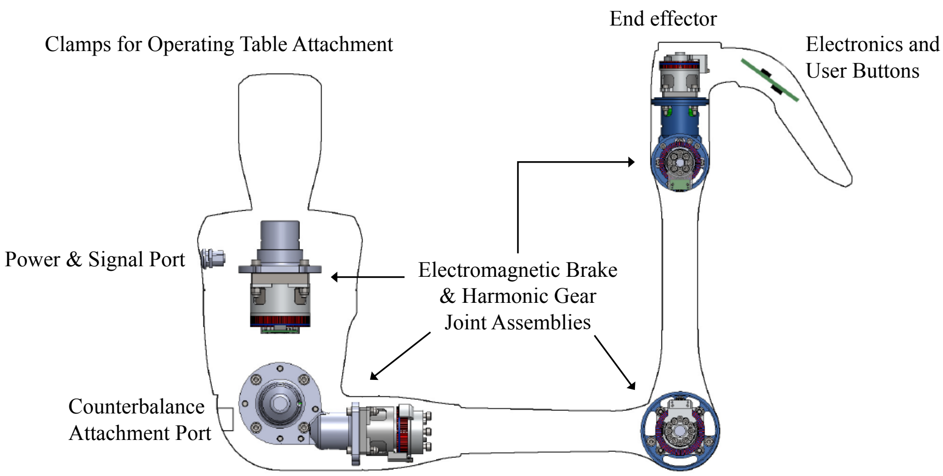

Figure 3.4: Components inside the Hamlyn Lightweight Robot Arm.

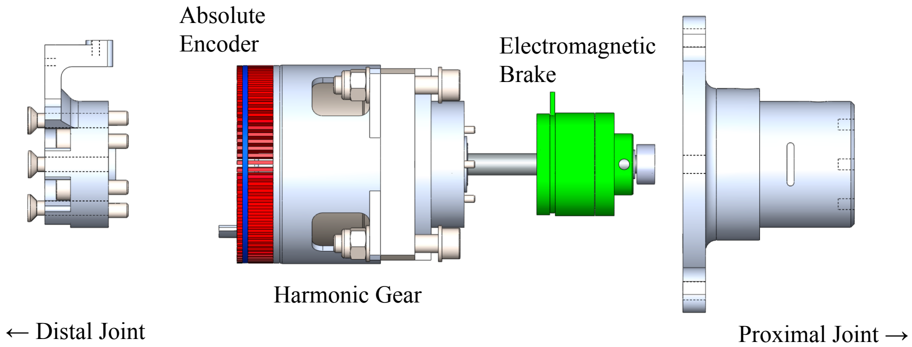

Figure 3.5: Exploded view of each rotational joint inside the Hamlyn Lightweight Robot Arm.

diagram of internal components is shown in Fig. 3.4. The payload limit of arm is 5 kg. The arm has been fully tested to comply EN 60601-1 standard and is granted as a CE-mark Grade-I medical device in 2015.

The internal assembly of each rotational joint is depicted in Fig. 3.5. Dual track multi-pole magnetic ring provides rotary position sensing. The number of pole pairs of both tracks are chosen so that the greatest common divisor of both numbers is one. Therefore, the combination of their phase angles is unique throughout the rotation range of the joint, providing absolute angle measurement [21]. A demonstration of the position tracking during the clinical trial is shown in Fig. 3.9. The torque estimation is implemented by measuring a slight movement of the harmonic drive transmission when the arm is locked [83].

The use of passive locking mechanism (eletromechanical brake) coupled with transmission system (harmonic gearing) provides instantaneous locking/releasing function for an articulated clamp. The response time of the brake is 7 milliseconds according to the manufacturer's specifications. The inherent backdrive friction of harmonic gearing is beneficial for prevention of sudden movements during operation.

3.3 Characterisation

A structural stiffness test is performed to measure the arm's stability under rated payload in different configurations. An optical tracking system Optotrak Certus (Northern Digital, Canada) is used to capture the movement

Configuration	Stiffness (mm/kg)	R^2
(a)	0.73	0.9944
(b)	0.39	0.9935
(c)	1.37	0.9900
(d)	0.26	0.9968
(e)	2.66	0.9961

Table 3.1: Structural stiffness test results based on different arm configurations shown in Fig. 3.7. The stiffness values are obtained from linear regression using deformation and force information, with R^2 showing the coefficient of determination.

of the arm while being pressed downward with predefined forces, as shown in Fig. 3.6. The tracking system's absolute 3D accuracy is 0.1 mm and its resolution is 0.01 mm.

The test setup uses two identical rigid bodies (probes) to measure the arm's structural deformation when a known load is applied at the end effector. Each probe, shown in Fig. 3.6, is 15 x 15 x 15 cm in size. It utilises five optical markers and is calibrated using the same tracking system. During the test, one probe is placed at the base of the arm, near one of the rails where the arm is attached to. Another probe is placed at the end effector, where the load is applied. The measurement is taken when user manually applies a known load to the end effector verified by a force gauge. The force gauge used is Sauter FK 250 (Balingen, Germany), which has an accuracy of 0.5% and a resolution of 0.1 N. The deformation is measured by a change in distance from the end effector to the base with no load and with a load. The base of the arm is used as a reference point as the desk where the arm is mounted on can also be deformed due to the payload. The tests were performed on the arm with various configurations depicted in Fig. 3.7. Table 3.1 lists the test result of each configuration. In each configuration, six different amount of forces are applied: 0, 10, 20, 30, 40, 50 N. The data is collected twice for each load application. The stiffness value is obtained by a linear regression.

The measured positioning stiffness is 0.39 mm/kg in normal TEM configuration as shown in Fig. 3.7 (b).

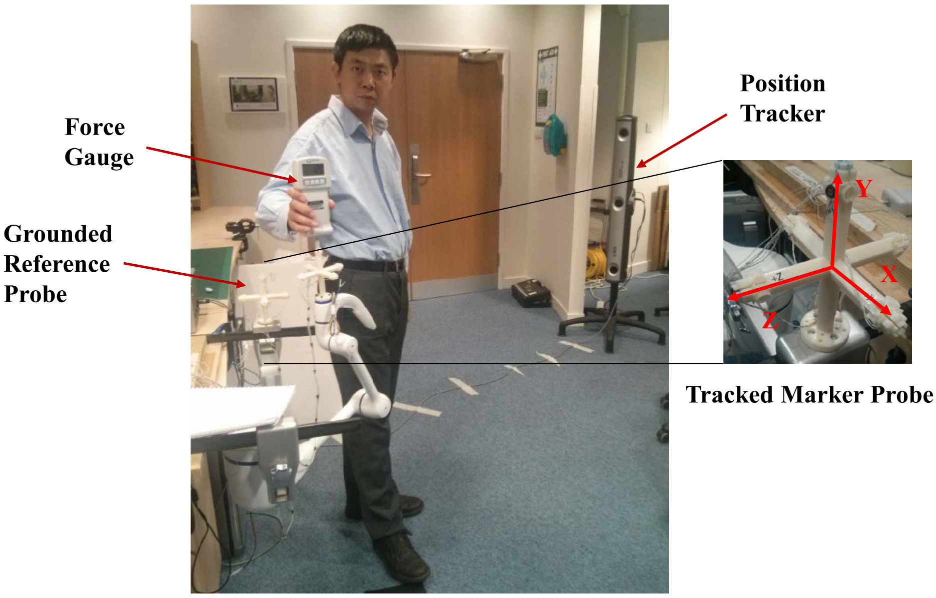

Figure 3.6: Experiment setup for the measurement of structural stiffness of the Hamlyn Lightweight Robot Arm.

3.4 Clinical Trials

An ethical approval for patient trials on the Hamlyn Lightweight Robot Arm were obtained and trials on four suitable patients requiring a transanal procedure have taken place.

Prior to the procedure, the arm is mounted on the end of the operating table. During the procedure, the surgeon first mounts the Wolf TEM Port and an endoscopic camera on the arm and then inserts them into the patient's rectal lumen by manipulating the support arm and observing through the endoscope. During the insertion, the surgeon can pause and observe from time to time by locking the arm. When the port is in place, the surgeon can then insert TEM instrument tools to perform the operation as required. The arm can be repositioned at any time during the surgery in order to obtain a better view of the lumen or to adjust the port's orientation for a convenient tissue manipulation. The transit time between locking and unlocking the arm is instant. Due to the instant locking and high stiffness of the arm, the surgeon can achieve a "what you see is what you get (WYSIWYG)" result from positioning the port.

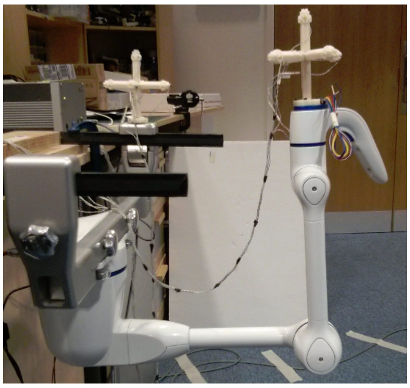

(a)

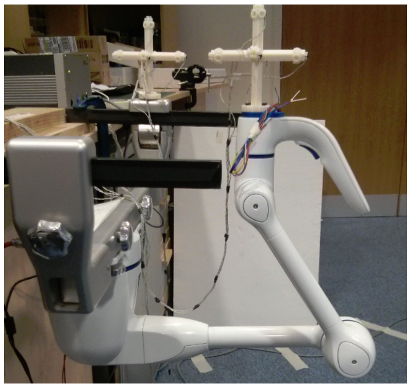

(b)

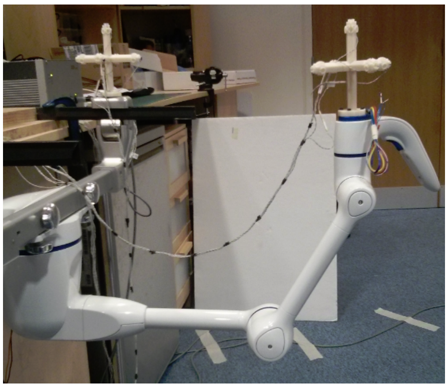

(c)

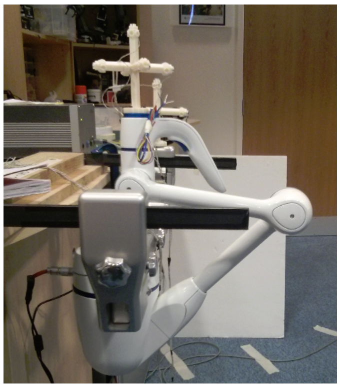

(d)

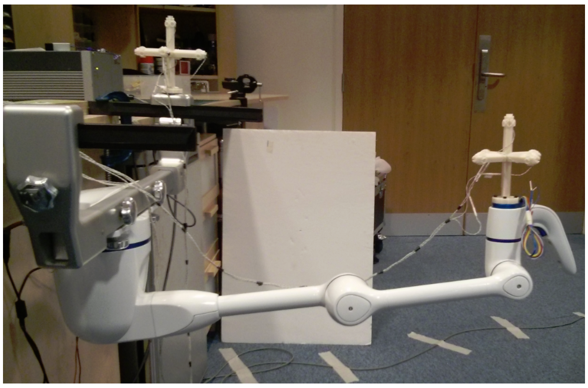

(e)

Figure 3.7: Configurations of the arm that the tests were performed on.

Figure 3.8: *In vivo* human trial of the Hamlyn Lightweight Robot Arm.

To assess the performance of the robotic arm, several factors including setup and procedure time were measured. During the operation, videos of the operating theatre and the endoscope feed were recorded, as shown in Fig. 3.8.

3.5 Results

Table 3.2 outlines the results from four clinical trials in chronological order. One case (#2) was a full TEM case which consists of three steps: *visual rectal examination*, *polyp excision*, and *closure by suturing*. Two of the cases (#1 and #4) included only the *visual rectal examinations* and *biopsy* for potential TEM operations. The last case (#3) was a *visual rectal examination* only to judge whether a TEM procedure or an abdominoperineal procedure was suitable for the patient.

The setup of the robot arm was timed from its unboxing until securely mounting to the operating table. The mounting time included docking the TEM port on the arm, connecting the endoscope and the camera system, and draping the whole arm. The adjustment time was measured covering a

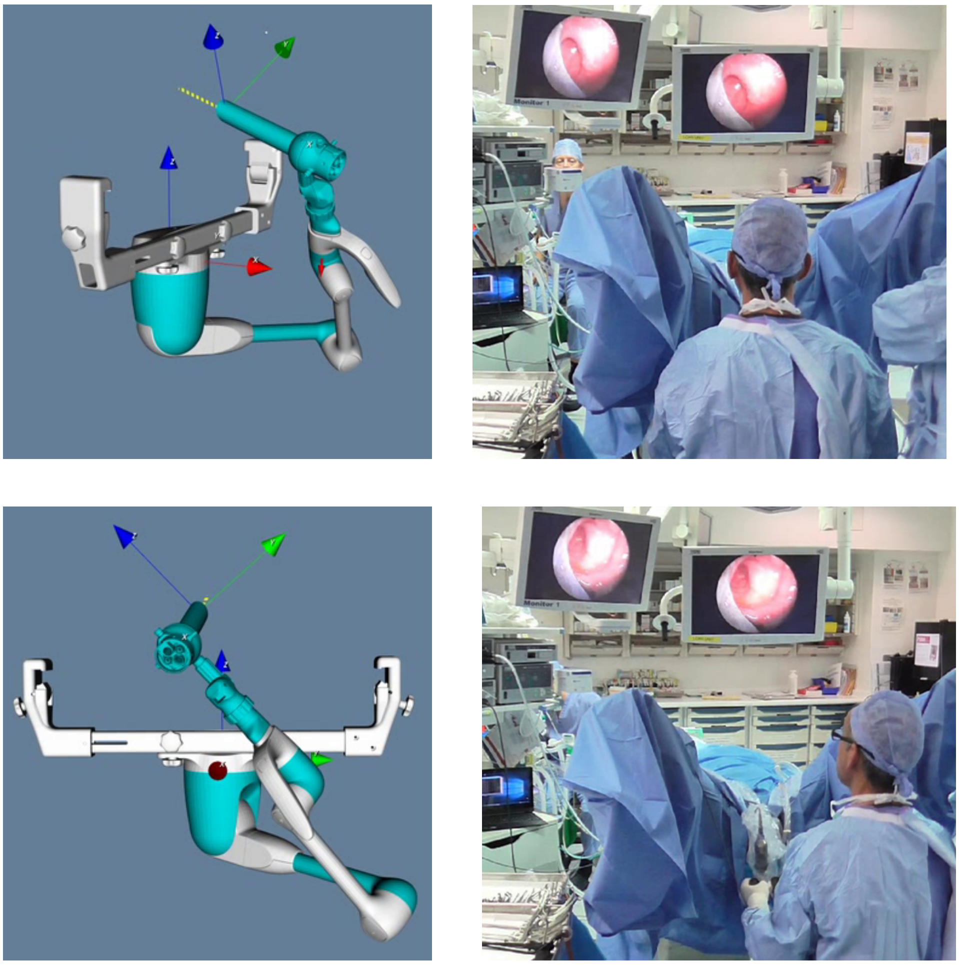

Figure 3.9: 3D rendering of the Hamlyn Lightweight Robot Arm based on the position tracking data from the absolute encoders inside the arm during the clinical trial.

Trial No.	Procedure	Time (s)				*Duration of Operation (s) [number of arm activations]			Total Number of Activations
		Setup	Mounting	Adjustment	Activation	I	II	III	
#1	Examination and biopsy	56	62	82	124	150 [5]	201 [0]	7 [0]	5
#2	TEM, excisions of polyps	61	55	22	44	187 [2]	2061 [5]	5 [0]	7
#3	Examination before laparoscopy	60	52	15	22	195 [3]	NA	NA	3
#4	Examination and biopsy	55	50	17	191	753 [8]	248 [0]	6 [1]	9

Table 3.2: Statistics of the Hamlyn Lightweight Robot Arm in human trials. *Surgical Phases: I–visual rectal examination, II–main procedure, III–post-procedure assessment.

brief arm test and checking all connections prior to the insertion. The activation time was the total manipulating time of the arm during the entire operation from the port insertion until finishing the operation. Activation time was measured only when the arm is manipulated (activated). The activation count was the total number of manipulations for the entire operation.

The entire operation procedure was divided into three phases, i.e. phase *I–examination*, from inserting the port into the rectum to start the examination until starting the main procedure; phase *II–main procedure* such as the biopsy or excision; and phase *III–post-procedure assessment*, i.e. to check the outcome of the main procedure. These phases were timed and the activation of the arm was counted.

The average setup of the arm was 58 s and the average mounting time was 55 s. The adjustment period was long in the first trial (82 s) but decreased quickly in the following trials. The mean time was 34 s. The arm's activation time was over 120 s with an average of about 20 s per activation in the 1^{st} and 4^{th} trial. The main reason was that the arm helped in phase I for examination and choosing the optimal place for a biopsy. In the 2^{nd} and 3^{rd} trial, the arm was activated briefly each time with average of 7 s per activation. In the phase II of both biopsy cases, there was no arm activation as the operation was straightforward. In contrast, the arm was moved 5 times in the phase II of the 2^{nd} trial in which the surgeon had to adjust the arm for a more complex operation including excision and suturing.

3.6 Conclusions

In this chapter, the development of an articulated global positioning robot that functions as a docking platform for instrumentation in single-access surgery is presented. The design is described and its stiffness characterisation are carried out. The arm's design is optimised for a low weight-to-payload ratio by utilising a passive electromagnetic locking mechanism. It is equipped with absolute encoders to enable tracking of the surgical tool in relation to the operating table.

The clinical trial results show that the arm was successfully tested and helped the surgeon to position the port or adjust the endoscope both intuitively and instantly.

4 Hamlyn Active Arm – Articulated Robotic Manipulator for Surgical Applications[†]

4.1 Introduction

The use of conventional surgical tool holders often requires manual positioning and adjustment due to a lack of weight compensation. In this chapter, we introduce a robotic arm with hands-on control. The robot incorporates a force sensor at the end effector which realises tool weight compensation as well as hands-on manipulation. On the operating table, the required workspace can be limited due to a number of instruments required. There are situations where the surgical tool is at the desired location but the pose of the holding arm is not ideal due to space constraints or obstacles. Although the arm is a non-redundant robot because of the limited degrees of freedom, the *pseudo-null-space inverse kinematics* can be used to constrain a particular joint of the robot to a specific angle while the other joints compensate in order to minimise the tool movement. This allows the operator to adjust the arm configuration conveniently together with weight compensation. Experimental results demonstrated that our robotic arm can maintain the tool position during reconfiguration much more stably than a conventional one. Another advantage of having robotic holding system is the capability of sensing of the tool position which enables an integration with imaging or navigation system.

[†] Part of this chapter was initially presented at:
P. Wisanuvej, K. Leibrandt, J. Liu, and G.-Z. Yang, **Hands-on reconfigurable robotic surgical instrument holder arm**, in *IEEE/RSJ International Conference on Intelligent Robots and Systems (IROS)*, Daejeon, 2016, pp. 2471–2476.

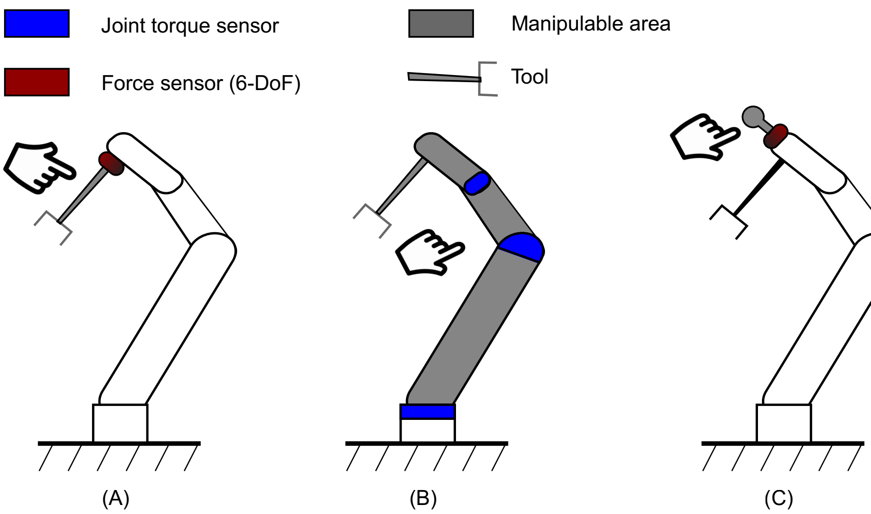

Figure 4.1: Different methods of using force/torque sensors to implement hands-on cooperative manipulation on an articulated robot arm.

Fig. 4.1 summarised three typical methods to implement hands-on cooperative manipulation on an articulated robot arm. It should be mentioned that these configurations may be mixed and combined in some robots, such as in [34]. They are different in the aspects of sensors, hand manipulation area and sensitivity, etc. A qualitative comparison between our method and another two methods is shown in the Table 4.1. The term "calibration-free" means the mass parameters; *e.g.* centre of mass (CoM), mass, moment of inertia; of the attached tool are not required. In summary, the proposed configuration as shown in Fig. 4.1 (C) overcomes another two in aspects of being calibration-free, insensitive to payload/contact force and highly sensitive while it sacrifices on full body manipulation area and contacting force sensing on the tool. In some applications, such configuration is beneficial. For instance, in an upper limb rehabilitation exercise, a patient may grab the robot to pick and place objects in which the payload can vary and high sensitivity is required for a smooth human-robot interaction while the contact force sensing of the tool is unnecessary.

In this chapter, a method allowing hands-on manipulation with weight compensation is introduced. This addresses common issues found in conventional (purely mechanical) surgical positioning arms which is the lack of weight compensation. Such compensations can make manipulation more

Table 4.1: Comparison between configurations for cooperative manipulation

Configuration	A	B	C
Calibration-free	No	No	**Yes**
Insensitive to load/contact	No	No	Yes
Full arm manipulation	No	**Yes**	No
Manipulation sensitivity	**High**	Low	**High**
Tool contact force sensing	**Yes**	**Yes**	No

convenient and require less effort from the user. This method is verified in an experiment using Lightweight Robot 4+ (LWR4+) by KUKA Roboter GmbH (Augsburg, Germany). Then, in Section 4.2, a robotic positioning arm designed for surgical instrument holding applications is introduced, the Hamlyn Active Arm. Its hardware designs and system integration are described. It implements the same method to allow hands-on manipulation with weight compensation as in LWR4+, but with one less DoF. In many surgical procedures, there can be multiple surgical instruments occupying the operating table workspace. Occasionally, when the surgical tools are repositioned to a preferred location, the resulting holder arm pose might obstruct the required workspace. In this case, the user has to reposition the holder arm linkages while keeping the surgical tool in place, i.e. reconfiguration. This task can be demanding, hence it is often done with multiple operators. To address this issue, we implement a hands-on reconfiguration technique. This enables user to change the arm body while it automatically maintains the mounted tool in place. Although the Hamlyn Active Arm is not a redundant robot, the pseudo-null space inverse kinematics (Section 4.4.1) allows user to change the joint position while the robot tries to compensate and keep the end effector movement minimal.

The remainder of this chapter is organised as follows. Section 4.4.2 shows some test results obtained from the proposed inverse kinematics. Section 4.4.3 explains the joint compliant control scheme for hands-on reconfiguration. In Section 4.5, two experiments involving participants to evaluate our methods are presented. The first experiment evaluates the performance of positioning tasks given the different tool weights, as well as the workload required by the users. This study compares the performance of using the holder arm with and without the weight compensation. The second experiment demonstrates how the Hamlyn Active Arm performed compared to a conventional tool holder in targeting and reconfiguration tasks.

4.2 Hamlyn Active Arm

The Hamlyn Active Arm, presented in Fig. 4.2, is an articulated robot with six DoFs. It is actuated by brushless DC motors coupled with harmonic drive gears. On-board controllers perform position, velocity, and current regulation. The arm weights 3.0 kg and reaches 780 mm at extended pose. The combination of motors and gears are selected so that the arm can handle a maximum payload of 1.5 kg with limited speed and acceleration. Each joint can also be backdriven by an operator in case of power loss. The internal CAD rendering is depicted in Fig. 4.3.

The robot communicates via CANopen bus with a computer system in which we have our control system implemented. The high level control software runs on Linux operating system. It perform several tasks including: motion generation, inverse kinematics, and communication with the motor controllers. Cartesian and joint trajectories generation is done using Reflexxes Motion Libraries [84].

The Hamlyn Active Arm incorporates an ATI Mini40 6-DoF force/torque sensor by ATI Industrial Automation (NC, USA) at the end effector. The data is sampled with a Data Acquisition (DAQ) PCIe card by National Instrument (TX, USA) running at 32 kHz sampling rate. The measurements are then filtered with a moving average filter with 100-sample window size. Fig. 4.2 shows the Hamlyn Active Arm with a mounted endoscopic instrument.

4.3 Methods

4.4 Hands-on Positioning with Weight Compensation

Positioning is one of the most common purpose of robotic manipulators where users can command the robot end effector to the desired position and orientation. The hands-on approach allows user to cooperatively guide the robot by hand to the desired location. The robot passively follows

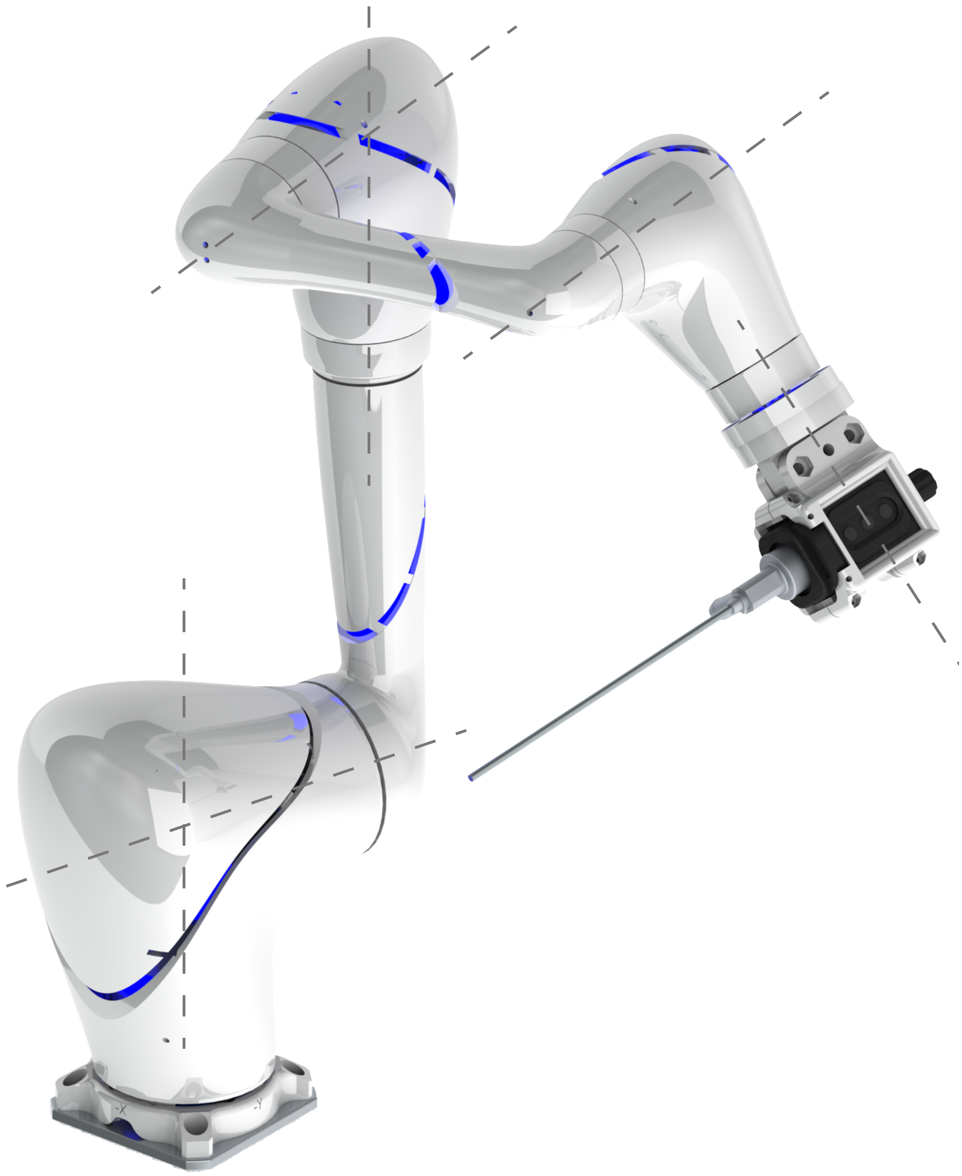

Figure 4.2: The Hamlyn Active Arm with an endoscopic instrument attached. Its axes of rotation are shown in dashed lines.

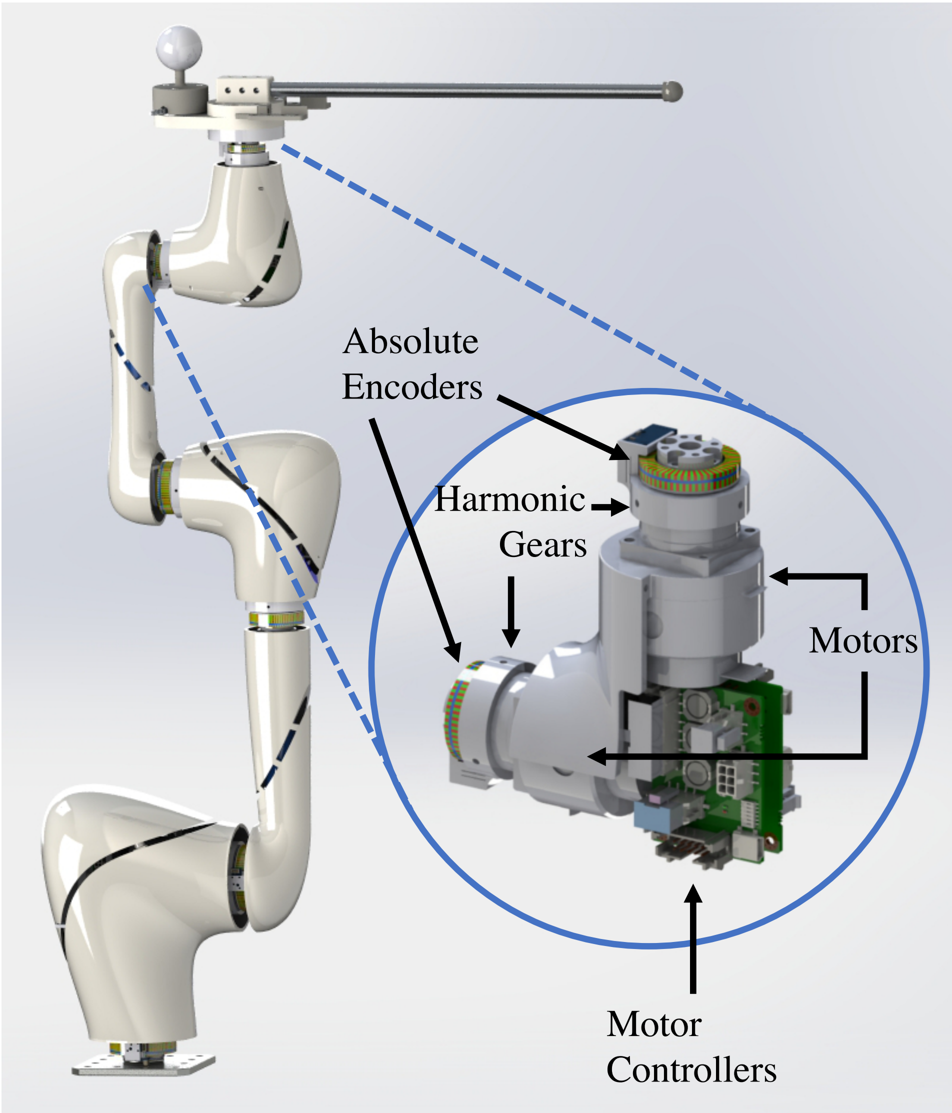

Figure 4.3: Internal components of a 2-axis sub-assembly of the Hamlyn Active Arm.

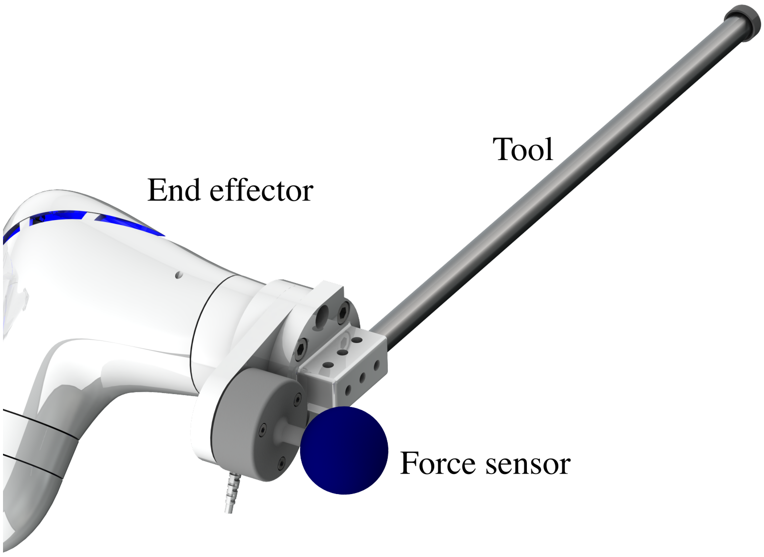

Figure 4.4: An example showing an end effector of an articulated robot with a tool and a force sensor mounted for hands-on positioning.

the user guidance and holds position when the user releases control. To sense external manipulation forces, a force sensor is installed to the end effector. The force sensor is placed such that the manipulation force is decoupled from the tool's weight. An example of such setup is shown in Fig. 4.4. The control scheme for hands-on manipulation is implemented by commanding the robotic end effector position according to the force measurements of the sensor. Due to the placement of the sensor, tool's weight and robot's weight do not affect the measurements. Therefore, the user perceive minimal force during manipulation and the tool can maintain position when released. Moreover, this configuration allows tool exchange without required calibration.

Our implementation is as follows. The raw reading from the sensor is subtracted with the baseline force to account for sensor's offset and the weight of the handle. The robot end effector movement is modelled as a virtual mass with a uniform friction in all directions. The force reading **F** in Cartesian space is converted to acceleration **A** by Newton's Law of motion and classical Coulomb friction model [85]. Resulting velocity from an integration of **A** is fed into a trajectory generator. The resulting robot pose is sent to the robot as a position command. The inverse kinematics

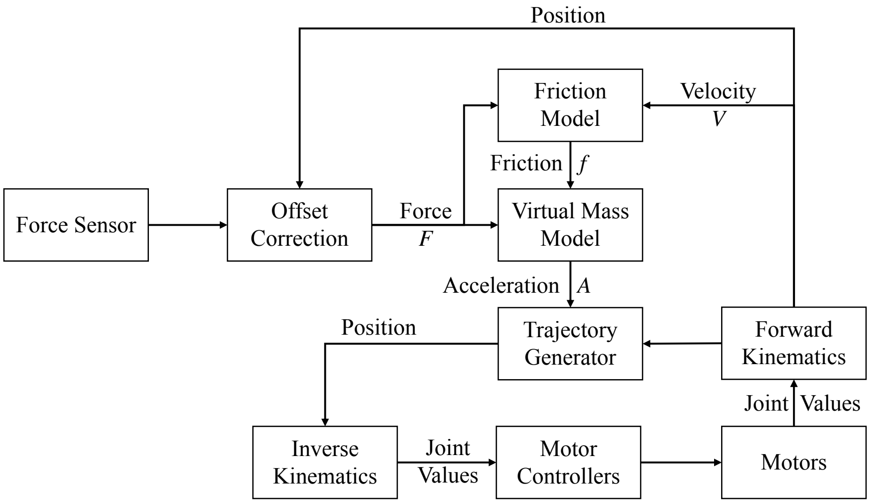

Figure 4.5: Block diagram of the control software for the hands-on positioning function.

routine then converts the Cartesian-space into joint-space trajectory for the motor controllers. The architecture of this control system is depicted in Fig. 4.5.

$$\mathbf{A} = \frac{\mathbf{F} - \mathbf{f}}{M} \tag{4.1}$$

$$\mathbf{f} = \begin{cases} \mathbf{f_c} sign(\mathbf{V}) & \text{if } \mathbf{V} \neq \mathbf{0} \\ \mathbf{F} & \text{if } \mathbf{V} = \mathbf{0} \text{ and } \mathbf{F} \leq \mathbf{f_c} \\ \mathbf{f_c} sign(\mathbf{F}) & \text{if } \mathbf{V} = \mathbf{0} \text{ and } \mathbf{F} > \mathbf{f_c} \end{cases} \tag{4.2}$$

where:

M = mass constant
$\mathbf{A}$ = acceleration
$\mathbf{V}$ = current velocity
$\mathbf{f}$ = Coulomb friction
$\mathbf{f_c}$ = friction constant
$\mathbf{F}$ = external force

4.4.1 Pseudo-null-space Inverse Kinematics†

The standard approach to solve the local inverse kinematics of a redundant robots is to combine the Moore-Penrose pseudoinverse together with a mapping of secondary goals into the *null* space [86]. Whereas, usually the primary goal is to reach a desired end effector pose $\boldsymbol{T}_d$, classical secondary goals include singularity, joint limit, and collision avoidance. *Null*-space mapping allows to use the redundant DoFs to follow secondary goals without impairing the achievement of primary goals. The pseudoinverse matrix $\boldsymbol{J}^\dagger$, can be calculated as:

$$\boldsymbol{J}^\dagger = \boldsymbol{V}\text{diag}\left(\frac{1}{\sigma_1}, \ldots, \frac{1}{\sigma_n}\right) \boldsymbol{U}^T, \tag{4.3}$$

where σ_i are the singular values of $\boldsymbol{J}$ resulting from singular value decomposition and $\boldsymbol{U}, \boldsymbol{V}$ are the left-singular and right-singular vectors respectively (i.e. $\boldsymbol{J} = \boldsymbol{U}\text{diag}(\sigma_1, \ldots, \sigma_n)\boldsymbol{V}^T$). $\boldsymbol{J}^\dagger$ is further used to calculate the joint velocities of the redundant manipulator;

$$\dot{\boldsymbol{q}} = \boldsymbol{J}^\dagger \dot{\boldsymbol{x}} + \left(\boldsymbol{I}_n - \boldsymbol{J}^\dagger \boldsymbol{J}\right) \dot{\boldsymbol{q}}_0 \tag{4.4}$$

where $\boldsymbol{I}_n$ is the n-dimensional identity matrix, and $\dot{\boldsymbol{x}} \in \mathbb{R}^6$ the desired end effector velocity to reach the pose $\boldsymbol{T}_d$. The second summand of (4.4) is used to map secondary goals $\dot{\boldsymbol{q}}_0$ into the *null* space. $\dot{\boldsymbol{q}}_0$, is defined as:

$$\dot{\boldsymbol{q}}_0 = k_{\omega 0} \left(\frac{\partial \omega(\boldsymbol{q})}{\partial \boldsymbol{q}}\right)^T \tag{4.5}$$

where $k_{\omega 0}$ is a goal weighting factor and $\omega\left(q\right)$ is the objective function for the secondary goals.

To overcome the problem of singular robot configurations the damped least squares (DLS)-inverse $\boldsymbol{J}^\star$ can be used at the expense of slower convergence in comparison to the pseudoinverse Jacobian $\boldsymbol{J}^\dagger$:

$$\boldsymbol{J}^\star = \boldsymbol{V}\text{diag}\left(\frac{\sigma_1}{\sigma_1^2 + \lambda^2}, \ldots, \frac{\sigma_n}{\sigma_n^2 + \lambda^2}\right) \boldsymbol{U}^T, \tag{4.6}$$

where λ is the damping factor. Finally, the robot end effector $\boldsymbol{T}_{ee}$ pose can

† This section is the work of *Konrad Leibrandt*. It is included in this thesis for completeness.

be calculated using:

$$\boldsymbol{T}_{ee} = \boldsymbol{f}_{\text{FW}} \left(\boldsymbol{q} + \dot{\boldsymbol{q}} \Delta t \right), \tag{4.7}$$

where $\boldsymbol{f}_{\text{FW}}$ denotes the closed-form forward kinematic function.

In order to perform a pseudo-*null*-space motion, one of the joint is fixed at a desired angle, hence, it becomes an underactuated robot with one less DoFs. To control an underactuated robot with n-joints (n=5 in our case) the proposed pseudo-*null* space concept considers task-space primary goals as $\boldsymbol{x}_{pri} = [t_x, t_y, t_z]$ and the remaining three DoFs are considered as secondary goals $\boldsymbol{x}_{sec} = [r_x, r_y, r_z]$. Therefore, we split the Jacobian $\boldsymbol{J} \in \mathbb{R}^{6\times n}$ into $\boldsymbol{J}_{pri}$, $\boldsymbol{J}_{sec} \in \mathbb{R}^{3\times n}$ with,

$$\boldsymbol{J} = \left[\boldsymbol{J}_{pri}^T, \boldsymbol{J}_{sec}^T \right]^T \tag{4.8}$$

as well as the task-space velocities $\dot{\boldsymbol{x}} = \left[\dot{\boldsymbol{x}}_{pri}^T, \dot{\boldsymbol{x}}_{sec}^T \right]^T$ and calculate the DLS-inverse $\boldsymbol{J}_{pri}^\star$ and $\boldsymbol{J}_{sec}^\star$, according to (4.6). Following,

$$\dot{\boldsymbol{q}}_0 = f_k \left(\Delta \boldsymbol{x}_{pri} \right) \boldsymbol{J}_{sec}^\star \dot{\boldsymbol{x}}_{sec}, \tag{4.9}$$

the secondary goals can be computed, where $f_k \left(\Delta \boldsymbol{x}_{pri} \right)$ is a scalar weighting function depending on the deviation from the primary goals. Combining (4.4) with (4.9) where $\boldsymbol{J}_{pri}^\star$ is used instead of $\boldsymbol{J}^\dagger$ the joint velocities for the underactuated manipulator can be calculated. Note that using a DLS-inverse results in deviations from the primary goals and furthermore introduces an error into the *null*-space mapping. The scaling function in (4.9) is chosen as:

$$f_k = 1 - \frac{\min \left(\| \Delta \boldsymbol{x}_{pri} \|, \Delta x_{pri,max} \right)}{\Delta x_{pri,max}}, \tag{4.10}$$

where $\Delta x_{pri,max}$ denotes a threshold for the maximum deviation from the primary goals for which secondary goals are considered. For small $\Delta x_{pri,max}$ secondary goals are quickly ignored and errors in the *null*-space mapping introduced by the DLS-inverse are mitigated, a large value in contrast represent a looser following of the primary goals.

4.4.2 Inverse Kinematics Experimental Results

In the following two use cases for the presented pseudo-*null*-space mapping implemented on the Hamlyn Active Arm are presented. First, multiple joint configurations can result in the same end effector pose. Workspace

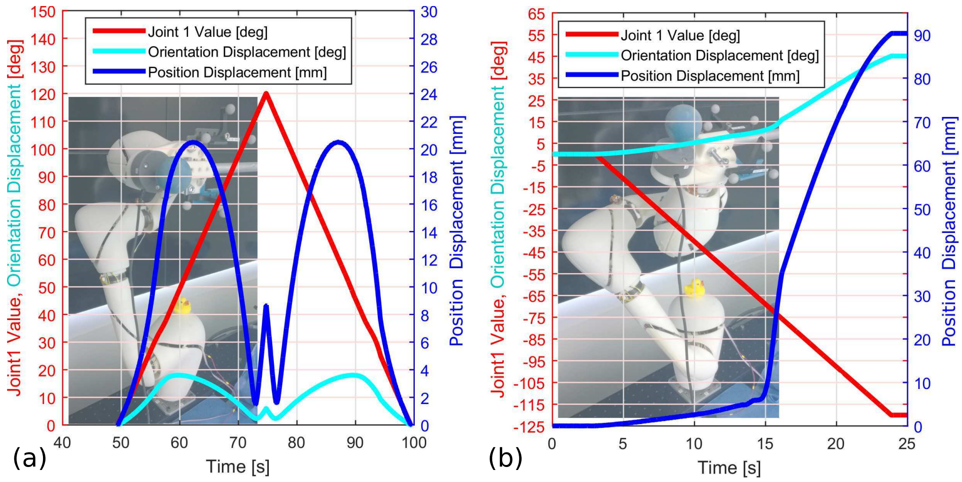

Figure 4.6: Pseudo-*null*-space mapping. Maintenance of a reference end effector pose while rotating its base joint. Background image: reference configuration.

considerations could require to change between these configurations (e.g. lower elbow vs. upper elbow), whereas a fixed end effector pose might not be strictly required loose maintenance of the pose could be advantageous. Fig. 4.6 (a) shows such a use case. The base joint (J1) is rotated from 0° position to 120° position while the remaining five joints try to maintain the end effector position. A maximal position displacement of 22 mm and an maximal orientation displacement of 20° are achieved. At an approximate base joint value change of 110°, an alternative joint configuration (switching from lower to upper elbow) for the desired pose is found.
The second experiment shows that certain configurations allow to maintain over a wide range a small position and orientation displacement. The configuration depicted in Fig. 4.6 (b) shows that the base joint can be turned from 0° to $-65°$ while maintaining a reference end effector pose with a position and orientation accuracy of 5 mm and 10°, respectively. However, higher changes of the base joint cannot be compensated.

4.4.3 Hands-on Manipulator Reconfiguration

Hands-on positioning the robot via an external force sensor is one way to command the robot cooperatively. However, relying on this alone would constrain the robot in the configuration provided by the inverse kinematics calculation. There are situations where the kinematics solutions are not ideal due to space constraints or obstacles. Using the pseudo-null space inverse kinematics can constrain a particular joint of the robot to a specific angle. This can allow the user to change the robot configuration to better suit the space requirements. However, changing this null-space constraint via computer interface might interrupt the user's workflow when performing tasks. Hence, we introduce another hands-on manipulation mode where user can directly reconfigure the robot by pushing its linkages. This is complementary to the hands-on positioning and can be used together to perform manipulation tasks more intuitively.

To implement compliant control on joints, an external joint torque measurement is required. For simplification, our implementation uses motor current measurements provided by the joint controllers. This is a crude measurement which does not take into account the transmission loss and friction. The gravity torque τ_g can be computed using an inverse dynamics function if the mass parameters (mass and CoM) of the robot is known, similar to Section 7.3.2. A thresholding on the measured current is used to determine whether a joint is pushed by the user. This threshold is tuned manually to suit a certain range of velocity and acceleration settings. Since the method is oversimplified and inaccurate, the joint output velocity is smoothen by a trajectory generator before being sent to the kinematics calculation.

$$I = k_t \tau \tag{4.11}$$

$$\tau = \tau_f + \tau_\alpha + \tau_g + \tau_{ext} \tag{4.12}$$

$$\omega = \begin{cases} 0 & \text{if } \tau_{ext} \leq T \\ K(\tau_{ext} - T) & \text{if } \tau_{ext} > T \end{cases} \tag{4.13}$$

where:

I = measured motor current
k_t = torque constant of the motor
τ = output torque of the motor
τ_f = torque due to friction
τ_α = torque due to acceleration
τ_g = torque due to the weight of the joint
τ_{ext} = external torque
ω = joint output velocity
K = gain
T = external torque threshold

4.5 Experiments and Results

4.5.1 Hands-on Positioning User Study

An experiment is setup to evaluate hands-on positioning performance on a commercially available robot designed for this purpose using its built-in gravity and payload compensation in comparison to our approach described in this section.

The Lightweight Robot 4+ (LWR4+) is chosen due to its built-in gravity compensation mode. This compensation is done via precise robot modelling and friction compensation by the joint torque sensors. Still, this requires correct payload parameters in order to compensate correctly. In the same time, we can easily equip a force sensor to the end effector and switch the robot operation to position control mode to emulate the Hamlyn Active Arm. Therefore, it allows experimenting with the same robot hardware for both configurations.

The setup is illustrated in Fig. 4.7, which consists of a LWR robot and a Mini40 Force/Torque Sensor. Another Lightweight Robot *iiwa 14 R820* is used to hold the tube for the experiments. Dummy tool with variable weights is mounted on the tool to mimic different tool weights.

A tool insertion task is used to validate the hands-on manipulation method. As illustrated in Fig. 4.8, the task for each participant is to pick-up and move the tool tip from a starting point far from the tube to the entry point of the tube by holding only the knob with one hand. The tool should be guided along the centreline of the tube until the tooltip reaches the exit

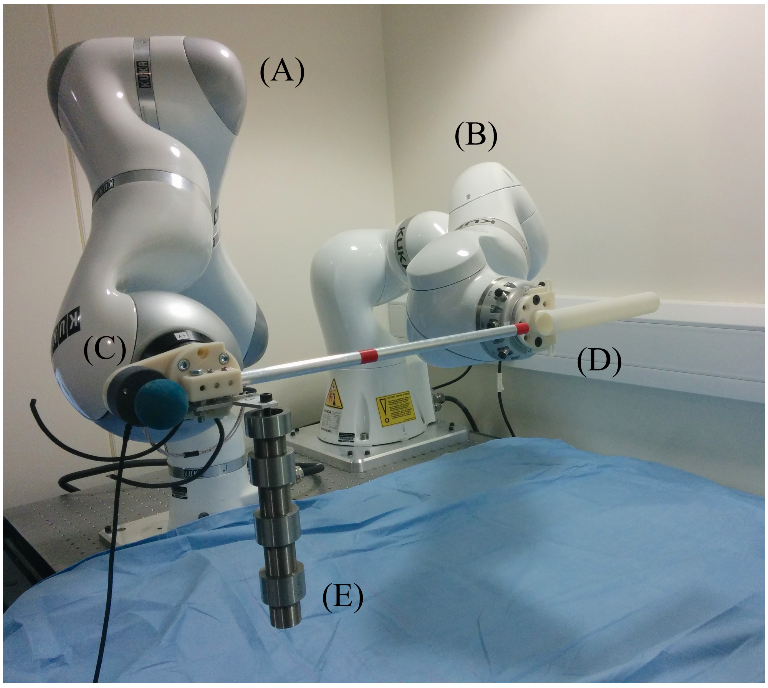

Figure 4.7: System components: A) KUKA LWR4+, B) KUKA LBR iiwa, C) ATI Mini40, D) Tool, E) Tube, F) Adjustable weights

point. Participants are asked to perform the task three times, with different tool weights and compensation modes between tasks.

This experiment aims to test the effect of using uncompensated tool holding robotic arm with hands-on manipulation to demonstrate whether or not the calibration-free feature is beneficial. The task measures accuracy, precision, and time for the user to perform precise tool insertion. A real-world example of this task would be a (robotic-assisted) component assembly in manufacturing industry.

The light and heavy tool are weighted 0.8 kg and 1.4 kg respectively. The compensation methods used are the LWR's built-in gravity compensation and our external force sensor based method. Therefore, there are four variations of parameters for this experiment in total. They are denoted as $LWR - Light$, $LWR - Heavy$, $FT - Light$, and $FT - Heavy$. The task is repeated three times for each participant.

In order to evaluate the effects of manipulating an un-calibrated tool, the LWR has only the correct tool parameters for the light tool. Hence, the user is expected to perceive 0.6 kg of equivalent tool weight with $LWR - Heavy$

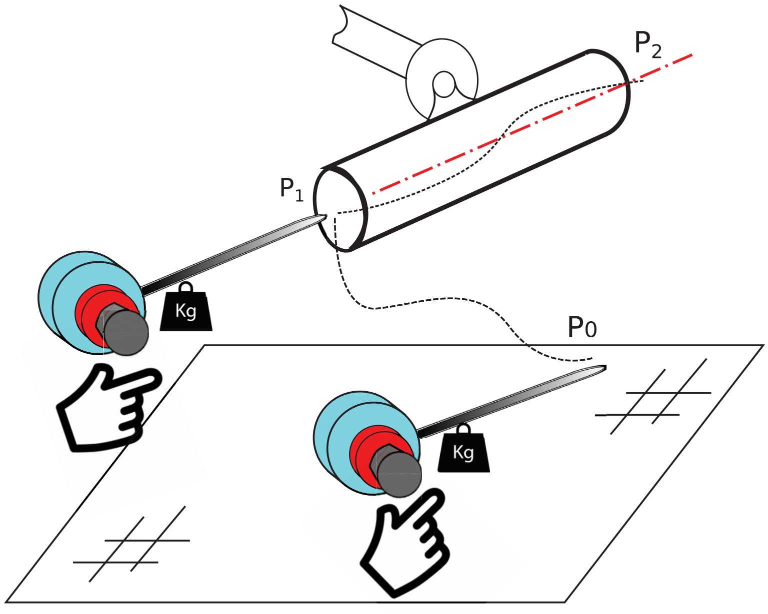

Figure 4.8: Experiment setup showing initial tool position P_0, tool entry position P_1, and tool exit position P_2

manipulation task.

Each participant is given 10 minutes to get familiar with the system in all task variations. There are total of 5 participants who took part in the experiments, resulting in 60 recorded tasks. Only the manipulation within the tube region is analysed while the rest is discarded. Three performance metrics for each are calculated: completion time, position deviation from the tube centreline, and manipulation force.

4.5.2 Hands-on Positioning – Experimental Results

Comparison of results from all four tasks with time, force, and position metrics are shown in Table 4.2. We observed only small difference between methods in terms of task completion time, ranging from 4.33 to 5.5 seconds, with $LWR - Light$ being the fastest. The distribution of tool tip's position within the tube from all the recordings are shown in Fig. 4.9. Also, it is observed that all the tasks have similar positional deviation, with the FT-tasks having slightly smaller deviation. However, there is a significant difference in manipulation force between LWR and FT methods. The force required to move the tool is always under 1.5 N for the FT methods, while

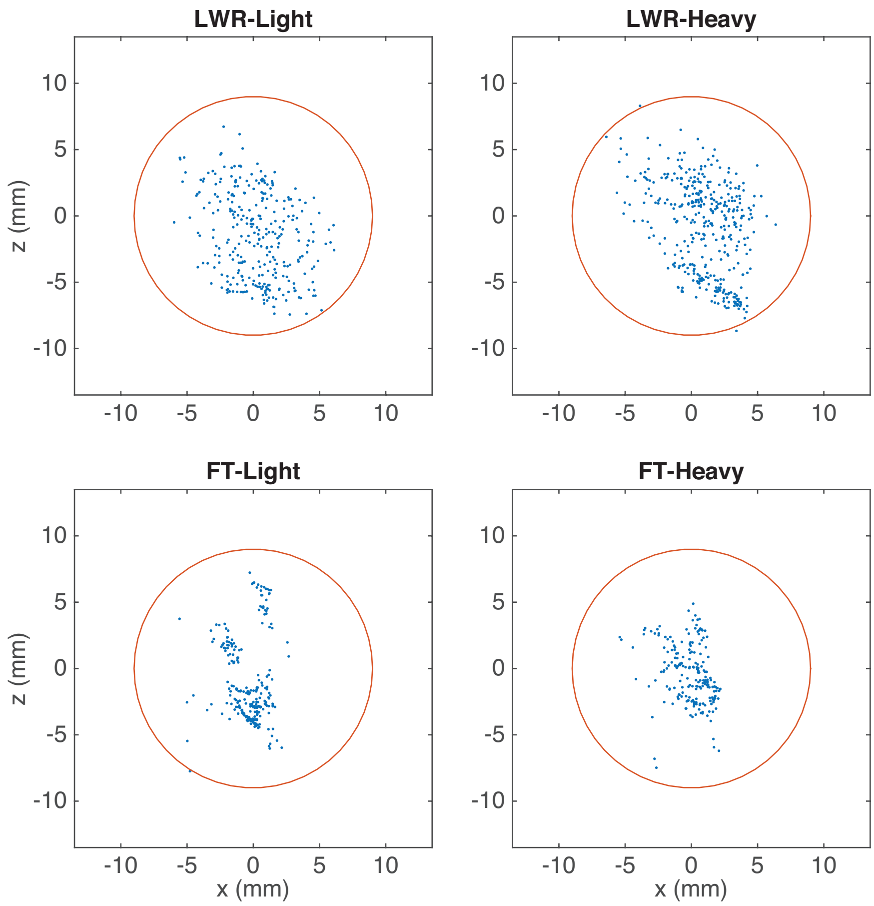

Figure 4.9: Recorded tool tip positions from all participants from all trials during the experiment 4.5.1. The points are evenly sampled from the continuous trajectories.

LWR's gravity compensation method requires around 7 N with calibrated tool and 12 N with un-calibrated tool as depicted in Fig. 4.10.

4.5.3 Hands-on Reconfiguration User Study

We setup a comparative study to evaluate the benefit of using the compensated robotic tool holder in contrast to manually operated operating table arms when the workspace is limited and a reconfiguration is required. The task chosen is a targeting task where the user is asked to move a long dummy surgical tool from an initial position to three different targets. After reaching the target, the user has to reconfigure the arm base joint to a spe-

Table 4.2: Results from hands-on positioning experiment showing $MEAN \pm SD$ and $(MIN - MAX)$

	LWR-Light	**LWR-Heavy**	**FT-Light**	**FT-Heavy**
Time (s)	$\mathbf{4.33} \pm 1.94$ $(2.67 - 9.47)$	5.30 ± 3.06 $(2.25 - 12.54)$	5.50 ± 2.20 $(2.89 - 8.46)$	4.64 ± 1.14 $(3.59 - 7.33)$
Deviation (mm)	3.89 ± 1.84 $(0.14 - 9.27)$	3.83 ± 1.90 $(0.06 - 9.63)$	3.39 ± 1.41 $(0.57 - 9.11)$	$\mathbf{2.35} \pm 1.31$ $(0.15 - 7.97)$
Force (N)	7.32 ± 0.91 $(3.88 - 11.66)$	11.98 ± 1.53 $(6.20 - 15.28)$	$\mathbf{1.36} \pm 0.25$ $(0.44 - 2.56)$	1.46 ± 0.23 $(0.49 - 2.20)$

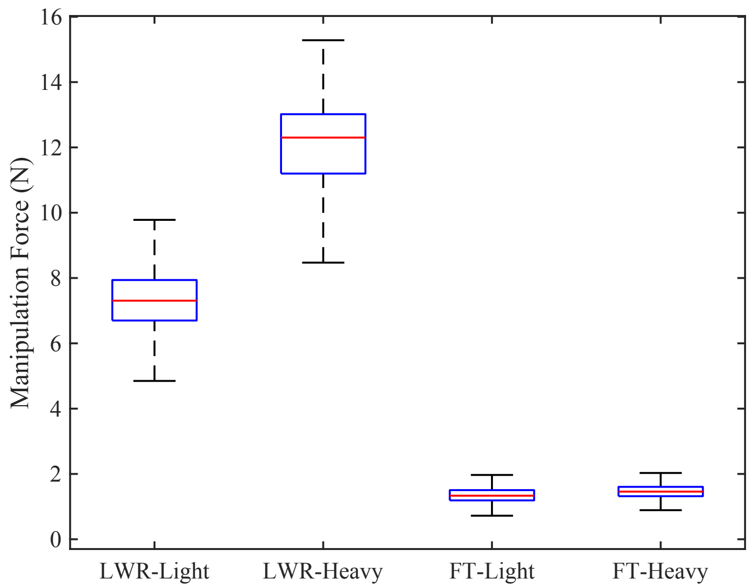

Figure 4.10: Comparison of user manipulation force

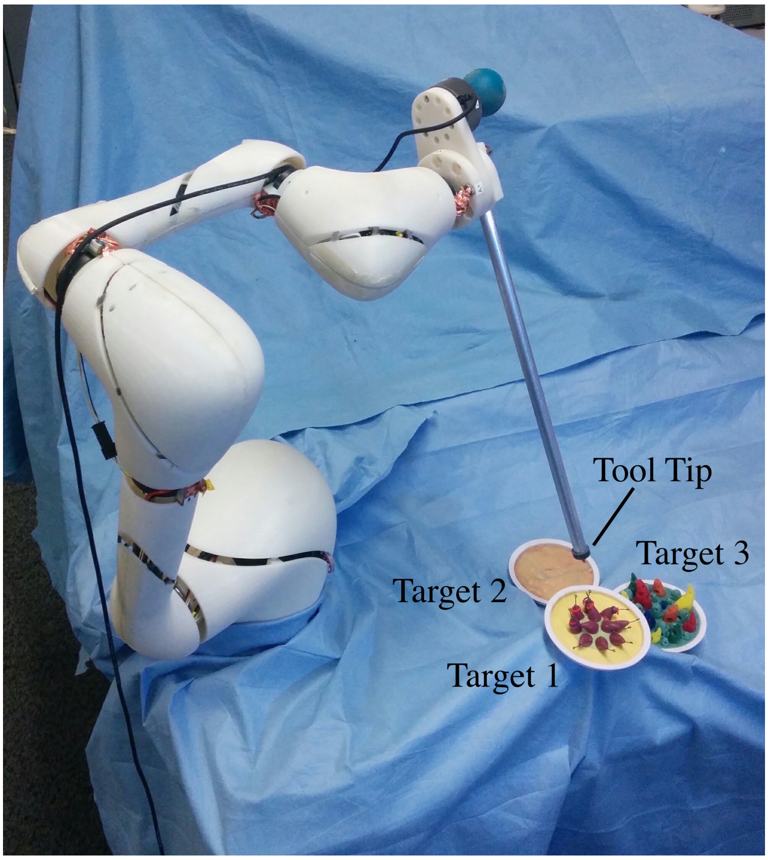

Figure 4.11: Experiment setup for targeting and reconfiguration tasks

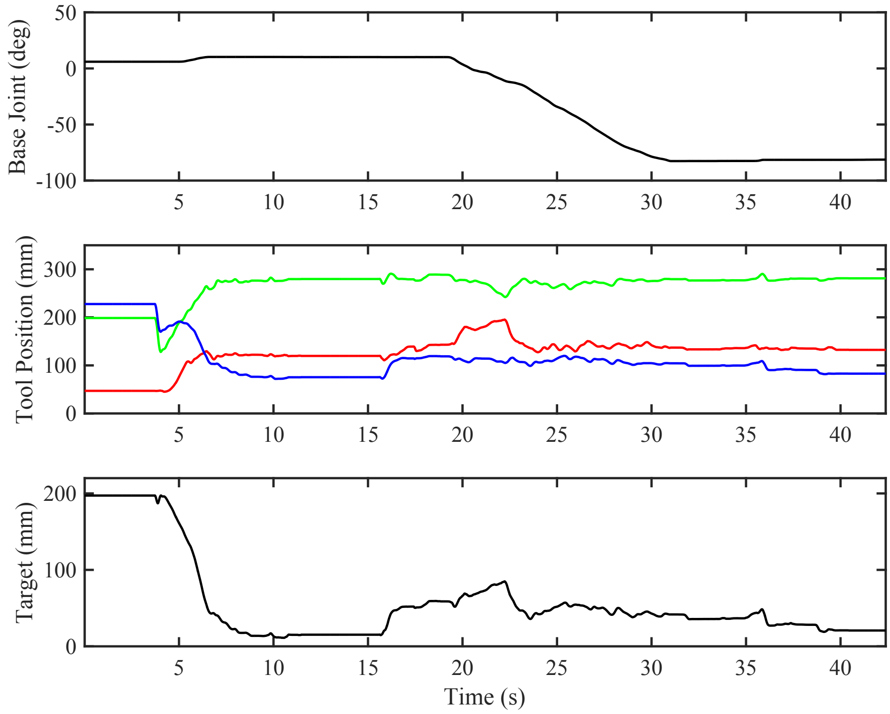

(a) *manual* mode

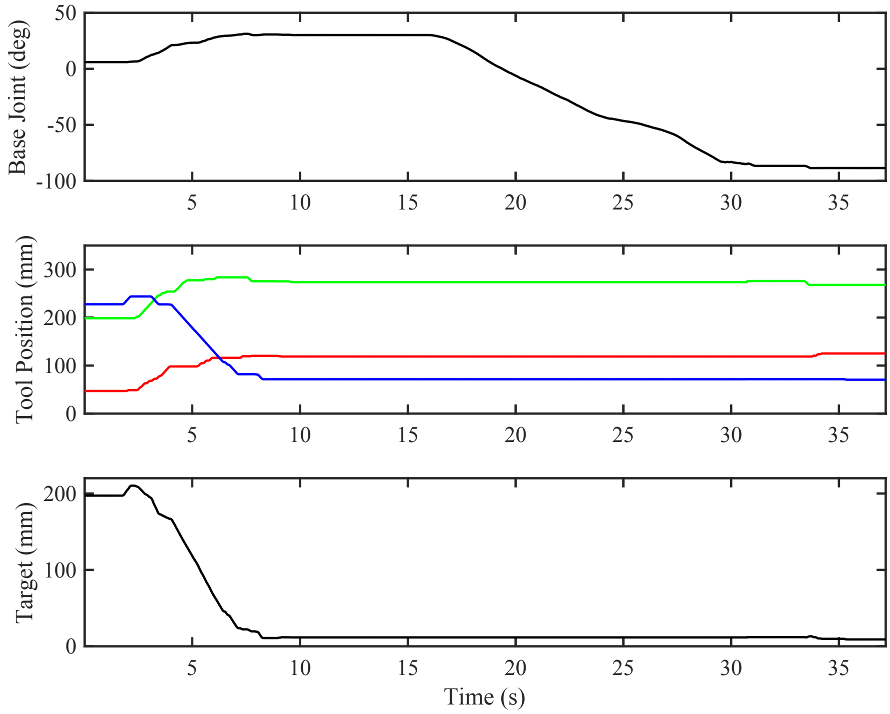

(b) *compensated* mode

Figure 4.12: Examples of collected data from experimental tasks with different operation modes.

cific angle in order to keep the workspace around the base joint clear while maintaining the tool position. The experiment setup is shown in Fig. 4.11.

Tasks are performed using the Hamlyn Active Arm working in two different modes. A *manual* mode, where the arm can be locked and released with a foot pedal, emulates the functionality of a conventional surgical instrument holder arm. A *compensated* mode, where the arm exhibits hands-on positioning and reconfiguration capabilities. All reconfigurations requires the base joint to be moved more than 90°. For each participant, the experiment is done twice with tool weights of 0.8 kg and 1.4 kg respectively. Fig. 4.12 shows examples of collected data where the target position is reached approximately within 8 seconds. Then, the robot is reconfigured. In the compensated case, the robot movement appears smoother and less deviated from the target. Additionally, in the *manual* mode, a fast drop of the tool position is observed in Fig. 4.12a at approximately t=4 seconds when the user pressed the release button (red=X, green=Y, blue=Z). This is due to the lack of gravity compensation. Similarly to the previous experiment, each participant is given a certain time to learn the system before the actual task. There are 5 participants who performed the experiment. In summary, there are 2 operation modes, 3 targets, 2 tool weights. Therefore, 60 tasks were performed in total.

4.5.4 Hands-on Reconfiguration – Experimental Results

The metrics used to evaluate the performance are: the time used to perform reconfiguration, the maximum displacement from the target during reconfiguration, and the total distance moved during reconfiguration. The quantitative results are listed in Table 4.3. We observed very similar results in the time required which is around 21 seconds. However, the displacement and movement are significantly lower in the compensated mode. The mean of maximum displacement is decreased more than 5 times and the mean of total movement is decreased 17 times with the compensation. Fig. 4.13 shows the performance improvement of the compensated mode.

Table 4.3: Results from hands-on reconfiguration experiment showing $MEAN \pm SD$ and $(MIN - MAX)$

	Manual	**Compensated**
Time (s)	21.3 ± 10.5 (5.7 – 45.2)	21.2 ± 4.8 (13.0 – 31.7)
Maximum displacement (mm)	83.8 ± 99.1 (16.4 – 394)	$\mathbf{16.0} \pm 7.6$ (0 – 32.8)
Total movement (mm)	805 ± 406 (240 – 1900)	$\mathbf{46.4} \pm 26.7$ (0 – 118)

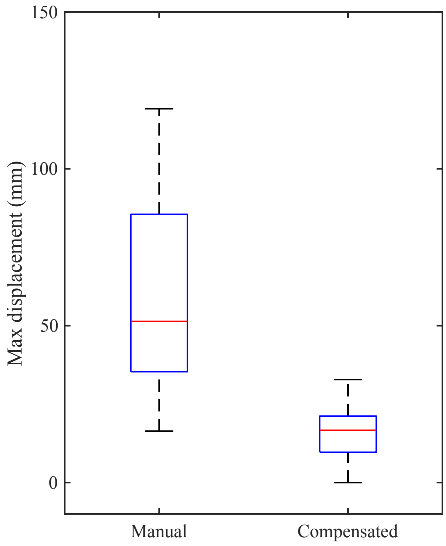

(a) maximum target displacement

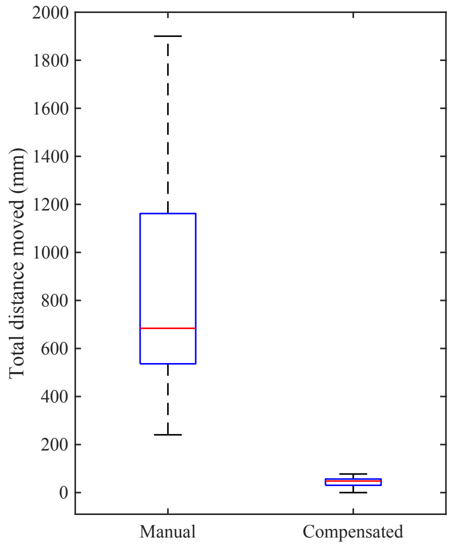

(b) total distance moved

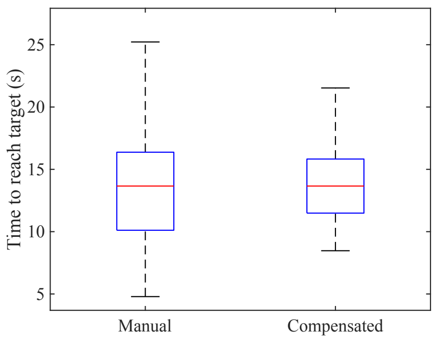

(c) Time to reach target

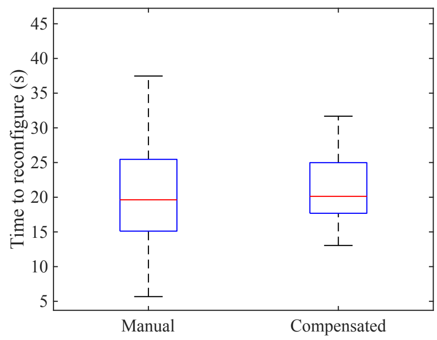

(d) Time to reconfigure

Figure 4.13: Results from reconfiguration experiments

4.6 Conclusions

In this chapter, we have presented the Hamlyn Active Arm, a robotic holder arm system that allows hands-on manipulation and reconfiguration based on a tool-mounted force sensor and joint current sensors. The arm is targeted at surgical instrument holding applications where mechanical articulated arms are generally used. Our experimental results show the advantage of using this arm where the weight compensation can reduce the workload of the operator. The placement of the sensor decouples the tool weight from the measurement. Therefore, it allows tool changes during the operation without calibration.

In several surgical procedures, multiple surgical instruments occupy the workspace around the operating table. Another advantage of our system is that the user can reconfigure the holder arm linkages while maintaining the position of the surgical tool. The pseudo-null-space inverse kinematics allows the Hamlyn Active Arm, which is non-redundant, to perform a reconfiguration while minimising the tool movement with the aid of current sensing-based joint compliant control. Our experiment shows that performing reconfiguration with a purely mechanical holding arm is a difficult task. With our method in the Hamlyn Active Arm, the amount of tool movement is significantly decreased. In the surgical context, it potentially leads to less damage to the surrounding anatomy.

5 Collision Detection and Object Characterisation with Robotic Manipulators†

5.1 Introduction

This chapter presents a novel blind collision detection and material characterisation scheme for a compliant robotic arm. By the incorporation of a simple MEMS accelerometer at each joint, the robot is able to detect collision, identify the material of an obstacle, and create a map of the environment. Detailed hardware design is provided, illustrating its value for building a compact and economical robot platform. The proposed method does not require the additional use of vision sensor for mapping the environment, and hence is termed as ‘blind’ collision detection and environment mapping. Based on the shock wave and vibration signals, the proposed algorithm is able to classify a range of materials encountered. Detailed laboratory evaluation was performed with controlled obstacle collision from different orientation and locations with varying force and materials. Furthermore, by using sound feature extraction and machine learning techniques, the classifier can classify four different materials which differ in hardness. In this chapter, we also demonstrate its use for detailed environment mapping by using the proposed method.

MEMS accelerometers are commonly used in aforementioned methods because of its compact size, low cost, high bandwidth and high sensitivity. This chapter proposes an approach by using MEMS accelerometers integrated with the robotic manipulator for:

† Part of this chapter was initially presented at:
P. Wisanuvej, J. Liu, C.-M. Chen, and G.-Z. Yang, **Blind Collision Detection and Obstacle Characterisation Using a Compliant Robotic Arm**, in *IEEE International Conference on Robotics and Automation (ICRA)*, Hong Kong, 2014, pp. 2249–2254.

1. Collision detection, impact location, direction, and magnitude estimation
2. Material property (hardness) identification
3. Unknown environment exploration and mapping

In this chapter, we perform a modification of an off-the-shelf robotic arm by rebuilding all the control electronics. By adding current sensor as a means of torque sensing, the arm becomes compliant with a torque controller. The accelerometer on board is used to capture the contact vibration of this compliant arm. By processing the acceleration data, the arm can detect the collision and estimates its location, direction, and magnitude. Additionally, the signal is processed further by using machine-learning algorithms to identify the material characteristics of the object. Finally, a blind exploration technique is implemented by using the proposed collision detection method.

5.2 Methodology

This section describes the implementation of the robotic arm. Details on hardware construction are presented along with the software implementation considerations for solving the blind collision detection, material identification, and exploration problems.

5.2.1 Robot Hardware

A 7 degree-of-freedom robotic arm *Cyton Alpha 7D 1G* (Robai, Philadelphia, PA) is used as the basis of our robot design, but with several major modifications. This is shown in Fig. 5.1. Its axes and range of motion are: *Shoulder Base,Pitch,Yaw* $180°, 170°, 180°$; *Elbow Pitch* $170°$; *Wrist Roll,Yaw,Pitch* $180°, 130°, 135°$. The arm is rated for 200 g of payload and 480 mm of maximum reach. Originally, each joint of the robot is equipped with a hobby servo motor, with the exception of *Shoulder Pitch* joint which has two servo motors (for doubled torque output). The improved version of the electronic boards for the motors are built to accommodate the required sensors including the current sensor, accelerometer, and magnetic encoder. The motor is driven by PID controllers with current and position control

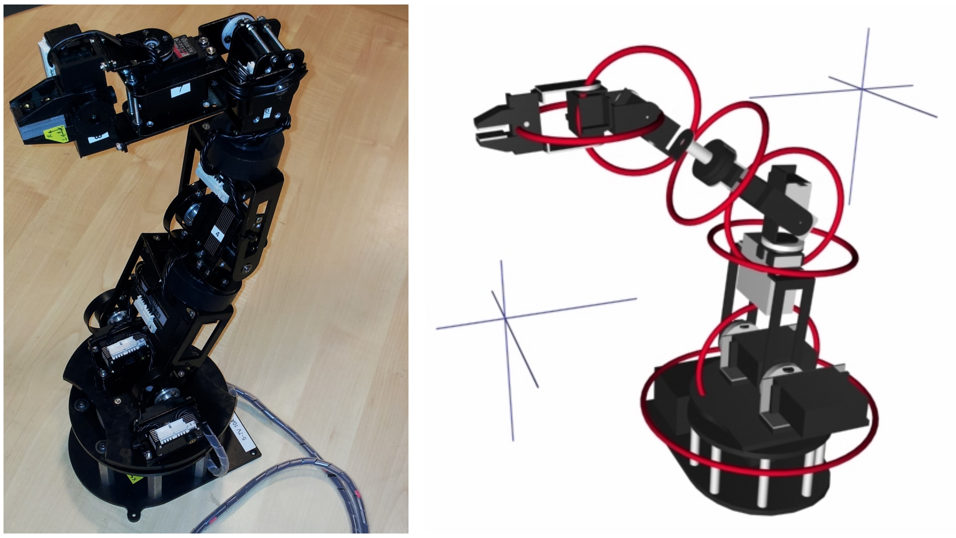

(a) Actual Arm (b) Axes of rotation

Figure 5.1: Cyton Alpha 7D 1G robotic arm by Robai. It has 7 DoFs with a gripper.

loops. The motor current is limited at a preset level to provide compliant control. The complete electronics is fitted inside each joint of the robot as shown in Fig. 5.2. The 3-axis accelerometer (Analog Devices ADXL346) is configured for ±16g measurement range and 3200 Hz data rate.

5.2.2 Blind Collision Detection

Accelerometers inside the robot joints give detailed readings of acceleration from each joint. In normal operating condition, the only source of acceleration signal is from the arm movement itself. This acceleration due to movement usually has a low frequency less than 100 Hz. In case of collision events, external force applied to the arm affects the acceleration significantly. The sudden impact with an external object causes vibration with much higher frequencies. Fig. 5.3 shows the acceleration signal due to arm movement with collisions. An example of high frequency vibration from the impact is shown in Fig. 5.4, the parameters are explained in the following.

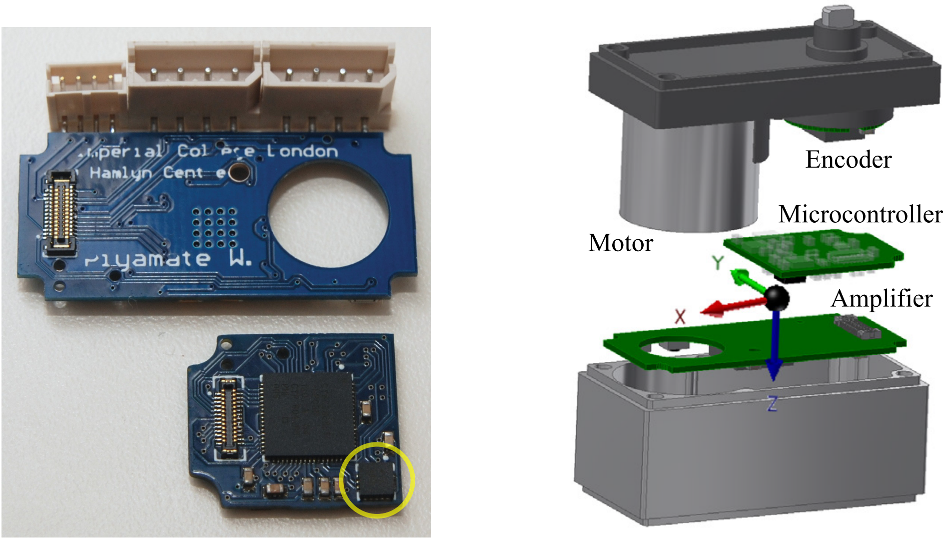

(a) Motor amplifier board (top)
Microcontroller board (bottom)

(b) Circuit assembly

Figure 5.2: The circuit board assembly of the customised servo motor for the robotic arm. The yellow circle indicates the location of the accelerometer. The axes illustrate the alignment of the sensor's coordinate frame.

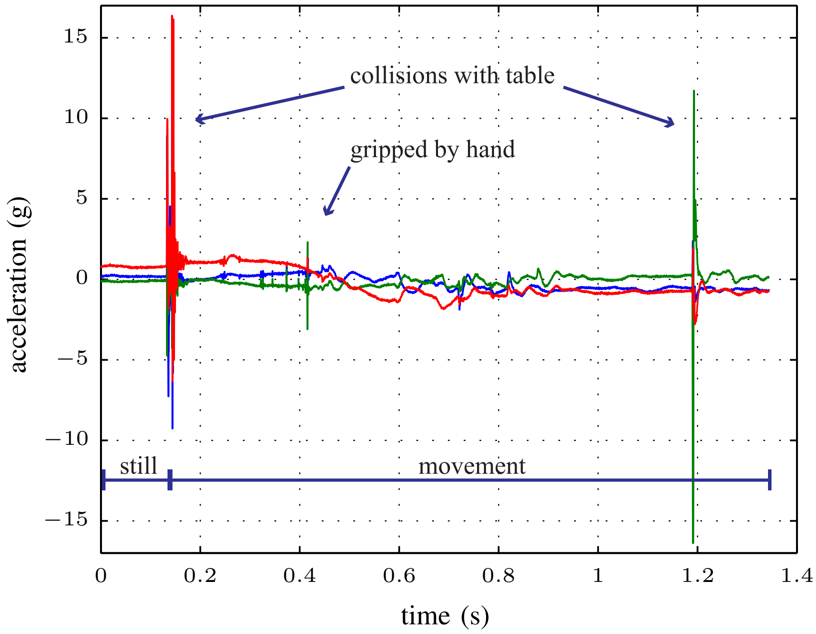

Figure 5.3: Acceleration signals of the arm's end effector showing hard collisions (with wooden table) and general collision (with finger) along with an arm movement

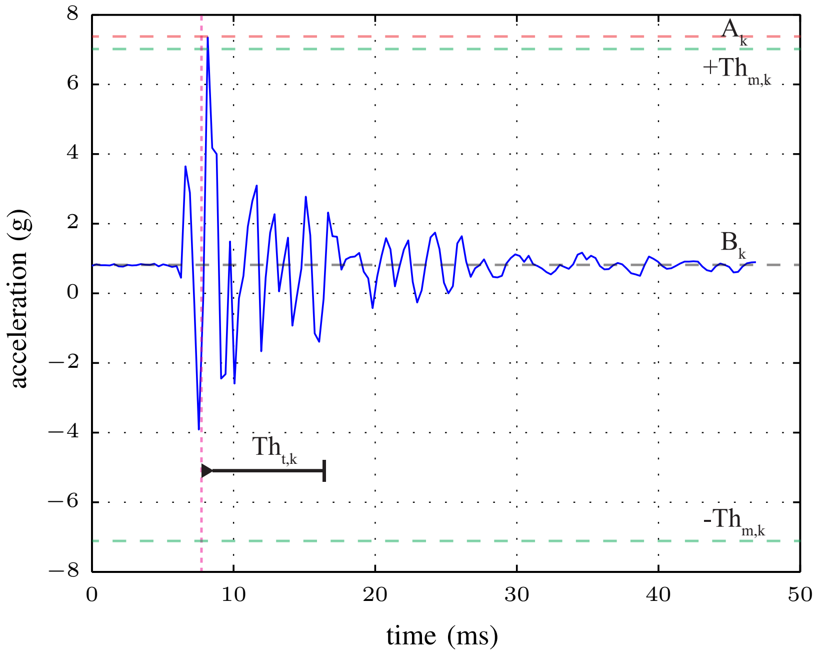

Figure 5.4: Parameters of a collision signal in k^{th} axis: Magnitude A_k, Baseline Acceleration B_k, Amplitude Threshold $\pm Tm_k$, and Time Threshold Tt_k

Detection

Due to the large difference in signal patterns from movement and collision signals, the peak pulse from collision can be easily detected using two criteria: Magnitude Threshold Tm and Time Threshold Tt. The time window is a threshold to accept only short peaks. This effectively filters out the acceleration peak from jittery robot movement causing false positives. The magnitude threshold is for filtering out the low joint vibration from the motor and gear system themselves.

Since each actuator has its own sensor, a total of 9 acceleration readings are obtained in real-time (7-DoF actuators + 2$^{\text{nd}}$ *shoulder pitch* + gripper). This provides redundancy in the system, as each part of the arm is being monitored. By having sensors on different parts throughout the robot, the collision events can also be localised. When a collision occurs, the vibration propagates from the point of impact through the links and joints that connect together.

Consider the case of a collision occurred in the i^{th} link, the circuit board and sensor is rigidly connected to the i^{th} joint casing and i^{th} link, whereas the $i+1^{th}$ and $i-1^{th}$ link connect to the i^{th} link through the gearing system. The vibration propagation via a rigid connection loses less energy than via a loose connection. The reduction gearing in the robot joint has around 4-5 stages with the ratio in ranges of 1:30-1:500. This causes the vibration magnitude to be greatly decreased because of the reduced torque when transferred through the gearing system, effectively damping the vibration signal propagation. With this simplified model, it suggests that the joint closest to the impact gets the highest signal. Thus, by comparing the signal magnitude the link-level localisation can be achieved. The magnitudes of the signal ($A_k : A_x, A_y, A_z$) are obtained from the peak amplitude of the collision signal.

$$m = \sqrt{A_x^2 + A_y^2 + A_z^2} \tag{5.1}$$

Direction and magnitude estimation

Each accelerometer sensor has 3 axes, arranged in XYZ Cartesian coordinates. This gives directional information of the collision. Since the sensor provides Cartesian output format, the absolute magnitude m of the signal can be calculated by Equation 5.1. Additionally, the impact direction can be obtained by the coordinate transformations of the sensor's coordinate frame inside the joint to the global reference frame using the following calculations (5.2)-(5.11).

It is important to note that the accelerometer signal contains earth's gravitational acceleration component. This measurement should be subtracted because it affects the calculation by shifting the whole signal with this offset. From the sensor's point of view, this Baseline Acceleration B_i changes according to the orientation of the sensor relative to the ground, including its movement. This can be determined from the kinematics calculation. A simpler approach can also be used. Since the vibration from any impact is typically very short (less than 20 milliseconds) compared to the change of acceleration from the arm movement, the baseline gravitational acceleration (including the sensor's offset) can be determine temporarily in each collision event. This signal baseline can then be obtained by calculating the median of the signal within the 50-ms window before the collision is detected. As this method assumes steady measurement within the time window, it only works with non-moving or slow-moving robots.

$$A_k = A_{k'} - B_k \tag{5.2}$$

where A_k, B_k are the magnitude of acceleration and the signal baseline in the k^{th} axis

The direction of impact in sensor's frame can be represented by Euler's angles (θ, ϕ, ψ). These angles are obtained from acceleration magnitudes using these equations derived in [87].

$$\theta = \arctan\left(\frac{A_x}{\sqrt{A_y^2 + A_z^2}}\right) \tag{5.3a}$$

$$\phi = \arctan\left(\frac{A_y}{\sqrt{A_x^2 + A_z^2}}\right) \tag{5.3b}$$

$$\psi = \arctan\left(\frac{\sqrt{A_x^2 + A_y^2}}{A_z}\right) \tag{5.3c}$$

The direction of impact is converted to a rotation $\mathbf{R_a}$ matrix as follows:

$$\mathbf{R_x}(\phi) = \begin{bmatrix} 1 & 0 & 0 \\ 0 & \cos\phi & \sin\phi \\ 0 & -\sin\phi & \cos\phi \end{bmatrix} \tag{5.4a}$$

$$\mathbf{R_y}(\theta) = \begin{bmatrix} \cos\theta & 0 & -\sin\theta \\ 0 & 1 & 0 \\ \sin\theta & 0 & \cos\theta \end{bmatrix} \tag{5.4b}$$

$$\mathbf{R_z}(\psi) = \begin{bmatrix} \cos\psi & \sin\psi & 0 \\ -\sin\psi & \cos\psi & 0 \\ 0 & 0 & 1 \end{bmatrix} \tag{5.4c}$$

$$\mathbf{R_a} = R_x(\phi)R_y(\theta)R_z(\psi) \tag{5.5}$$

The homogeneous transform of the impact direction in sensor's reference frame $\mathbf{^sp}$ is represented by

$$\mathbf{^sp} = \left[\begin{array}{ccc|c} & & & 0 \\ & \mathbf{R_a} & & 0 \\ & & & 0 \\ \hline 0 & 0 & 0 & 1 \end{array}\right] \tag{5.6}$$

At each link i, the collision $^{s_i}\mathbf{p}$ is transformed to the direction and location $\mathbf{p}$ in global reference frame.

$$\mathbf{p} \;=\; {}^0T_i \; {}^iT_{s_i} \, \mathbf{^{s_i}p} \tag{5.7}$$

where ^0T_i is the robot's homogeneous transform at link i in global reference frame, and $^iT_{s_i}$ is the transformation of sensor's orientation in i^{th} joint's reference frame as in Equation 5.10.

The robot link's transformation ^0T_i is derived by multiplying successive homogeneous transformations of each joint as follows:

$${}^0T_i \;=\; {}^0T_1 \; {}^1T_2 \; {}^2T_3 \; \cdots \; {}^{i-1}T_i \tag{5.8}$$

Each homogeneous transformation $^{i-1}T_i$ is derived using Denavit-Hartenberg (DH) convention. This convention uses four parameters to describe the transformation matrix from one joint frame to another: Link Length a_i, Link Twist α_i, Joint Distance d_i, and Joint Angle θ_i.

$$
{}^{i-1}T_i = \begin{bmatrix} \cos\theta_i & -\sin\theta_i\cos\alpha_i & \sin\theta_i\sin\alpha_i & a_i\cos\theta_i \\ \sin\theta_i & \cos\theta_i\cos\alpha_i & -\cos\theta_i\sin\alpha_i & a_i\sin\theta_i \\ 0 & \sin\alpha_i & \cos\alpha_i & d_i \\ 0 & 0 & 0 & 1 \end{bmatrix} \tag{5.9}
$$

Each sensor's coordinate is transformed to its joint's reference frame. The accelerometer is inside the joint, hence results in rotation component only. $\mathbf{R_{s_i}}$ can be derived in a similar way as in Equation 5.5.

$$
{}^{i}T_{s_i} = \left[\begin{array}{ccc|c} & & & 0 \\ & \mathbf{R_{s_i}} & & 0 \\ & & & 0 \\ \hline 0 & 0 & 0 & 1 \end{array}\right] \tag{5.10}
$$

As a result, the direction and location of collision signal $\mathbf{p}$ is obtained in Equation 5.7.

$$
\mathbf{p} = \left[\begin{array}{ccc|c} & & & x \\ & \mathbf{R} & & y \\ & & & z \\ \hline 0 & 0 & 0 & 1 \end{array}\right] \tag{5.11}
$$

where $\mathbf{R}$ is the rotation matrix representing impact direction, and x, y, z represent the impact location.

5.2.3 Object Identification

When different materials hit an object, varying sound signatures are produced. Human can roughly identify the material by the impact sound ourselves. This suggests that impact vibration caused by collision has its own characteristics based on the material. Since the acceleration from impact vibration follows a similar pattern as in impact sound [88], similar techniques of sound processing can be used. Sample signal from collision with different materials are shown in Fig. 5.5. The vibration signal can be processed using the machine learning techniques. Using the previous detection method, the collision signal can be segmented. By considering the vibration signal as

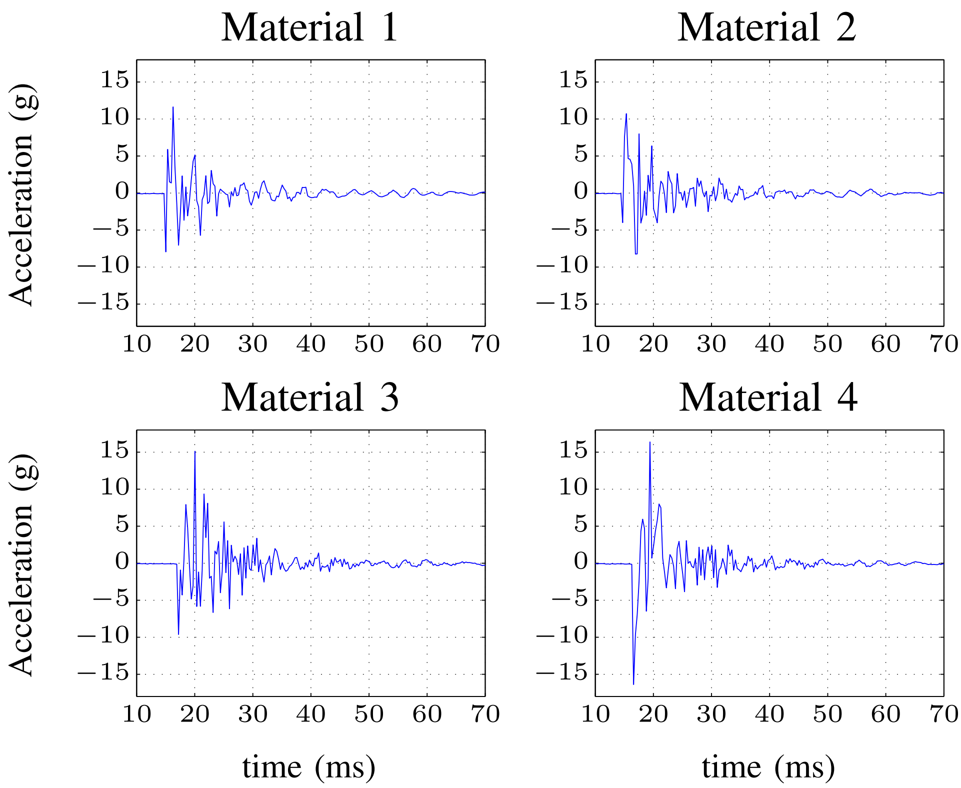

Figure 5.5: Acceleration signals for collisions from different materials used in experiments

a sound, its characteristics can be described by comprehensive amount of sound features. These features can be extracted by sound processing software. Then classifiers are used to build a model of material classification based on the vibration features.

The diagram 5.6 shows the data flow of the classification process. Due to nature of the data capturing, the hardware has limited memory capable of holding 10 impacts at a time. The data capture for each variable combination is split into 10 captures to get total of 100 hits. To process the signal, each impact needs to be segmented individually. This can be done easily since the time interval of each impact is programmed and consistent throughout the experiment.

In order to process the signal with the classifiers, its features need to be extracted. As the vibration signal is a time-domain signal similar to the voice signal (with lower frequency), the audio features extraction library is used to obtain those features. The *YAAFE – Yet Another Audio Feature*

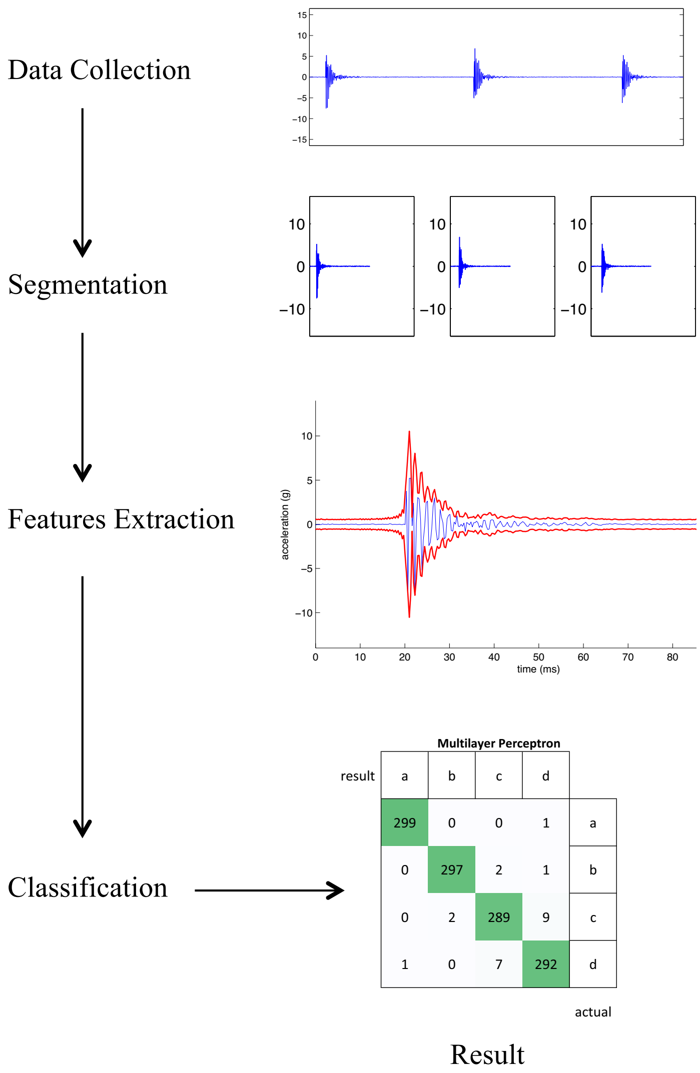

Figure 5.6: Material classification pipeline.

Extractor [89] is used. The list of features used are shown in Table 5.4. The chosen features considered to be related to the material properties are described here.

1. **Spectral Flatness**
   This is a ratio between geometric and arithmetic mean of the frequency spectrum. It provides a way to quantify how tone-like a sound is, as opposed to being noise-like. It has been used as a measurement of song similarity [90].

2. **Spectral Rolloff**
   This is the frequency so that 99% of the energy is contained below. This has been used as one of the feature in a speech/music discriminator [91].

3. **Zero Crossing Rate**
   Zero Crossing Rate, the number of zero crossings of the signal. This has been used as one of the feature in a speech/music discriminator [91].

4. **Envelope Shape Statistics**
   This provides statistical measurements of the signal envelope in time-domain. It contains centroid, spread, skewness and kurtosis of the signal's amplitude envelope. It has been used in similar application to classify the floor surface by quadruped robot [50].

5. **Temporal Shape Statistics**
   Similar to *EnvelopeShapeStatistics*, but this computes statistics from the original signal rather than the signal's envelope.

6. **Spectral Shape Statistics**
   Similar to *Envelope Shape Statistics*, but this computes statistics from the magnitude spectrum of the frequency-domain signal. It has been used in this work [92] about music information retrieval.

7. **Auto Correlation**
   This is a computation of cross-correlation of a signal with itself. It is the similarity between observations as a function of the time lag between them. It has been used in many signal processing applications including music, as a pitch detection algorithm [93].

8. **Energy**
   This is the total energy computed by calculating the Root Mean Square of the time-domain signal. It generally describe the vibration energy produced. This has been used as a main feature for localising the impact location using multiple accelerometers in [94].

9. **tPeak and fPeak**
   These two features are related to the peak of the collision signal. *tPeak* is the time when the signal reaches its peak amplitude. *fPeak* is the frequency component of the signal that has the highest signal intensity.

With these waveform features extracted, all the attributes are fed into 5 classifiers to perform the classification. The dataset is split into 90% training set and 10% testing set. The data splitting is performed using the cross-validation method so the splitting is randomised and distributed equally. The classification is done using *Weka – Waikato Environment for Knowledge Analysis* software [95]. The parameters used in the classifiers are default values supplied by the software. Following is the list of classifiers used.

- Naive Bayes
- J48 Decision Tree
- Support Vector Machine (SVM)
- Regression
- Neural Network : Multilayer Perceptron

5.2.4 Environment Exploration

As the manipulator has capability of collision detection, this can be extended further to perform blind exploration (without visual sensors). With the known robot kinematics, each joint location in space can be calculated. When the robot hits an unknown obstacle within the environment, its position based on location of impact can be determined. By simultaneously moving the robot around in space to collect collision data, the point cloud of the environment can be created. With the information of impact direction, each collision point is tagged with a normal vector. The plane can be estimated with this vector to build a surface mesh of the environment.

5.3 Experiments

To evaluate the accuracy of each of the proposed methodologies, detailed laboratory experiments have been performed. The experiments conducted contain three parts. In the first two experiments, arm is configured to be stationary, whereas the arm is manually controlled in the third experiment.

5.3.1 Collision Detection

The experiment is carried out as shown in Fig. 5.7. A solenoid is used as a tool to hit the robotic arm in different locations. It is rigidly fixed to the table with a clamp. The tip of the solenoid is a round shaped rigid plastic. In each hit, the experiment is configured with three variables: link number, direction, hit magnitude. The robot has six links. Each link is hit with two directions perpendicular to the link's surface. Three impact magnitudes are controlled by energising the solenoid with 35V DC power supply using pulse widths of 6, 10, and 15 milliseconds respectively. Each combination of location and direction is hit with three different magnitudes and repeated for 10 times. This experiment format collected a total of 360 collisions.

5.3.2 Object Identification

The experiment is setup in a similar way as previous. The only difference is that the tip of the solenoid is also a controlled variable. Four different tips are built from a 3D printer using different materials. We call these material M_1, M_2, M_3, M_4. The material properties are shown in Table 5.1. All tips have identical shape.

Mat.	Tensile strength(MPa)	Shore hardness	Elongation at break (%)	Equivalent Material
1	0.8-1.5	26-28 (A)	170-220	Rubber band
2	2-4	55-65 (A)	80-100	Eraser
3	15-25	90-100 (A)	25-35	Tyre
4	50-65	83-86 (D)	10-25	Plastic helmet

Table 5.1: Material properties of the solenoid tips used in the object identification experiment

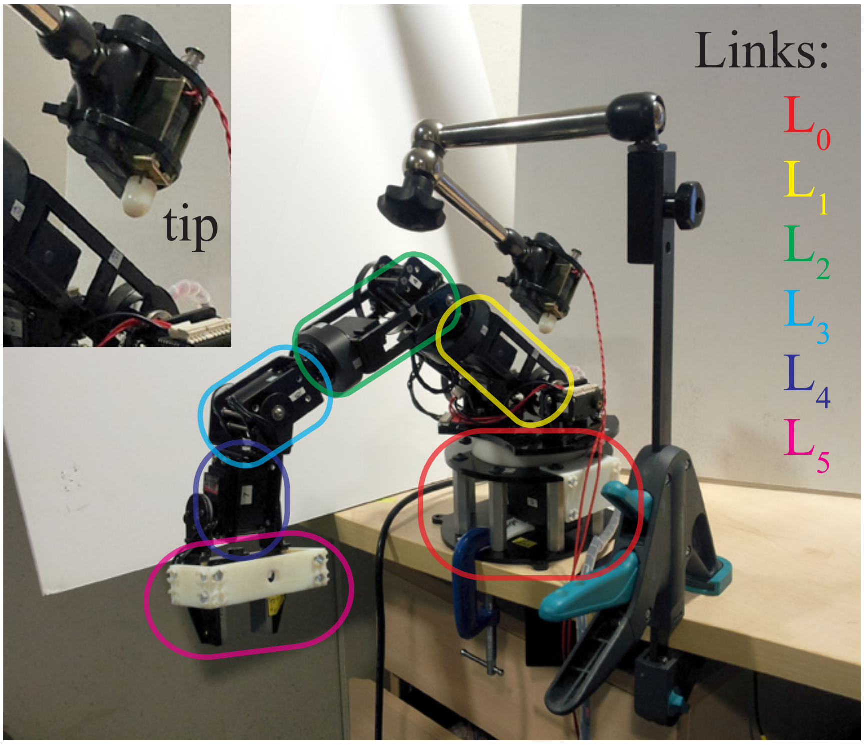

Figure 5.7: The experiment setup using *Cyton Alpha 7D 1G* robotic arm and a solenoid with interchangeable hardness tips (showing the white tip in enlarged image). The arm is divided into 6 links (L0-L5) for the purpose of location identification of collisions.

Figure 5.8: Solenoid tip materials, showing material M_1, M_2, M_3, M_4 respectively

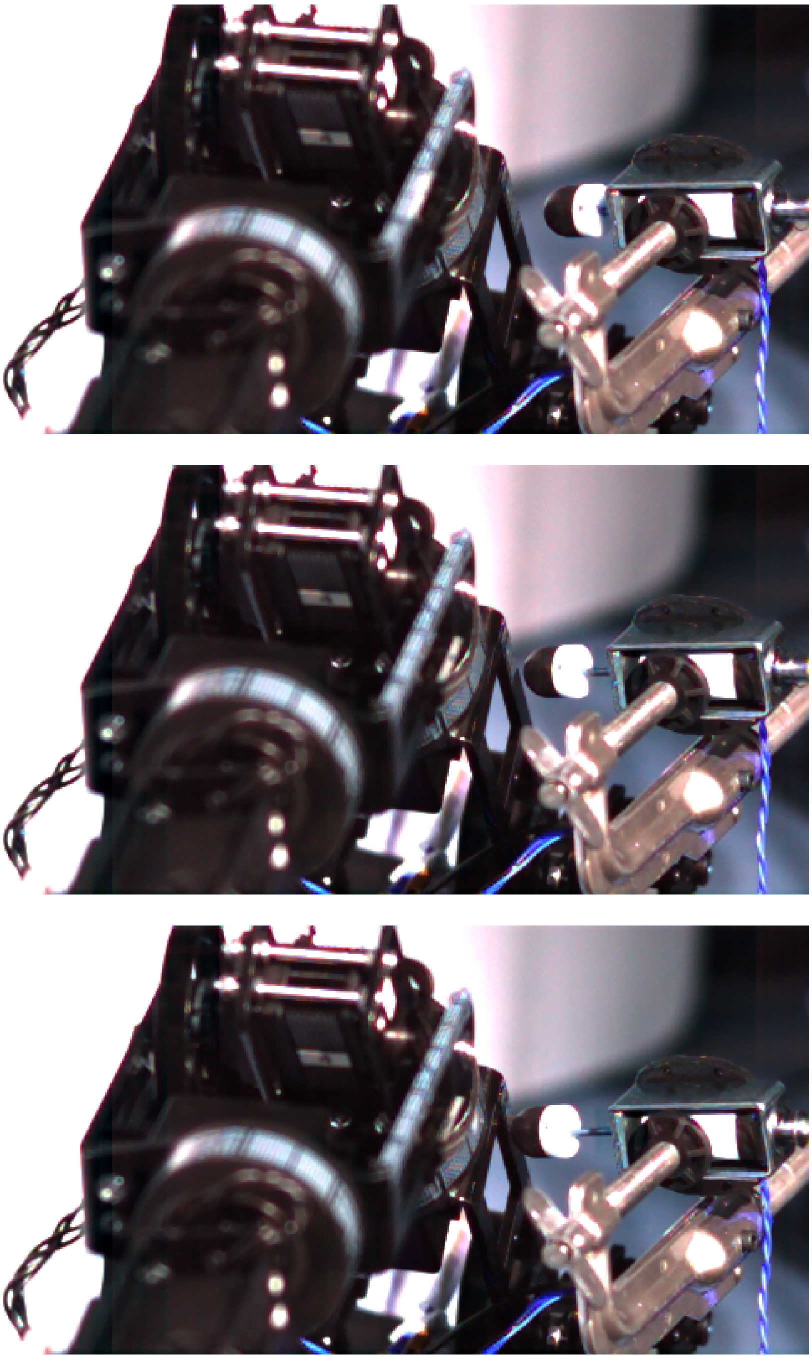

Figure 5.9: Collision sequence captured at 4000 frames/sec, this entire sequence takes 15 milliseconds

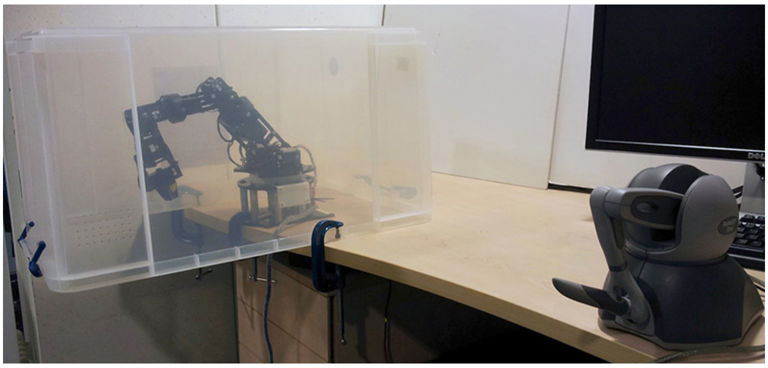

(a) Scenario 1

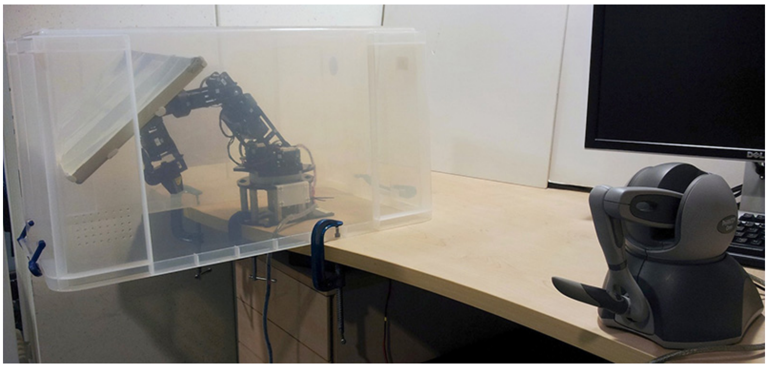

(b) Scenario 2

Figure 5.10: Experiment setups of environment exploration, Scenario 1: arm in an empty box, Scenario 2: an obstacle is added into the box

In this experiment, each object hits the robotic arm repeatedly 100 times on the same spot. Together with 12 possible combinations of variables, the total number of datasets are 1200. Each material is considered as a class, hence there are total of 4 classes with 300 datasets for each class. Fig. 5.9 depicts the sequence of this experiment captured at high speed of 4000 frames per second.

With the extracted features from *YAAFE*, the total number of attributes for each dataset is 397. All datasets are fed into 5 classifiers to perform the classification.

5.3.3 Environment Exploration

For environment exploration, the experiment setup includes two scenarios. For the first scenario, the rectangular box is placed to cover the arm workspace. Additional sloped plastic plate is added as another obstacle for the second scenario. The flat surface is chosen for the simplicity for data collection and result evaluation. To simplify the arm trajectory generation, the arm is controlled manually by a human operator. A Phantom Omni (Sensable, Wilmington, MA) haptic device is used as a controller. It has 6 degrees of freedom. All of the degrees of freedom are mapped to the joint angle of the robotic arm. Scaling is applied to make the operating range of the haptic device matches the joint range of the robot. Since the arm has an extra degree of freedom, compared to the controller, one of the arm's joint is kept stationary.

The translucent plastic box is used. The inside dimension of the box is $62.7 \times 39 \times 35.3$ cm. Obstacle in the first scenario is the box itself. Due to workspace constraint, only 4 of the sides are reachable. The second scenario involves one sloped plane as an obstacle in addition to the box. This makes the second scenario have 5 reachable sides. The data collection is performed by capturing the joint angles and the acceleration signal at the same time. The movement of the robotic arm is determined by user's decision, with best effort to reach as many faces of the obstacle as possible. Fig. 5.10 shows the experiment setup in two scenarios.

5.4 Results

5.4.1 Collision Detection

The experiment evaluations can be divided into four parts: *Collision Detection, Collided Link Location Identification, Magnitude Estimation, and Direction Estimation*. These experimental results are shown in Fig. 5.11. To identify the collided link, simply the joint that has strongest signal amplitude is identified. This can only identify the joint that has collided, not the exact location of impact. Regarding the *Collision Detection*, the sensitivity of 98% and specificity of 77% are achieved. The magnitudes and directions are estimated using methods described in the previous section. They values are then sorted into ranges of three (magnitudes) and two (directions). They are compared with the ground truth and result in percentage of accuracy.

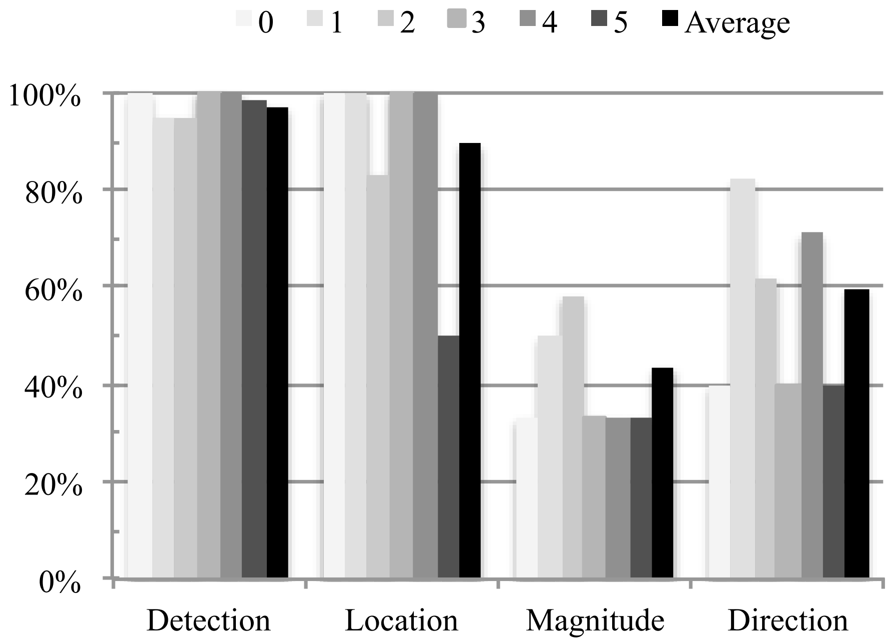

Figure 5.11: Collision detection and estimations accuracy for each robot's link corresponding to Fig. 5.7

Measurement	Scale	RMSE Link 0	Link 1	Link 2	Link 3	Link 4	Link 5	**Mean**
Direction	3.14	0.98	0.21	0.54	0.85	0.40	0.90	**0.65**
Magnitude	3.00	2.26	1.05	0.58	0.71	1.89	1.70	**1.36**

Table 5.2: RMSE values for the direction and magnitude estimations between the estimated and actual value in the experiments

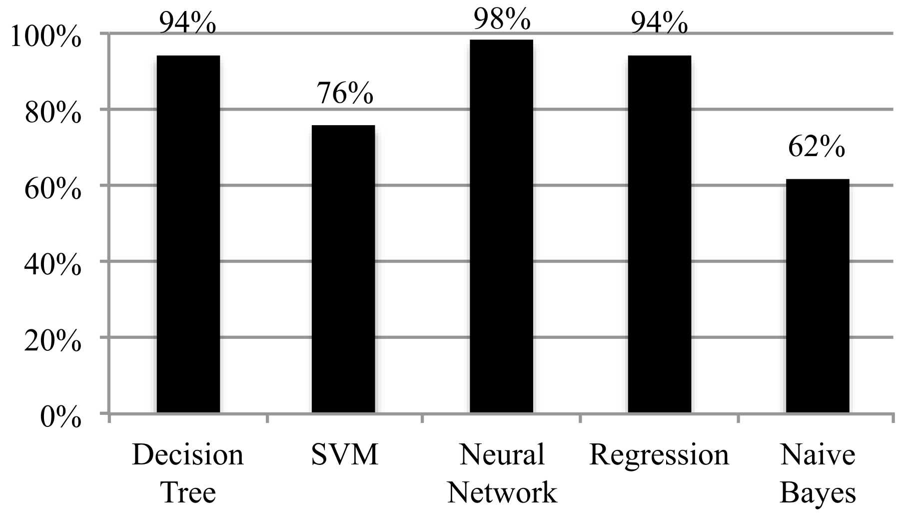

Figure 5.12: Object identification accuracy

5.4.2 Object Identification

Fig. 5.12 shows a comparison of the classification accuracy. Three of them give very accurate results, with the highest of 98%. The confusion matrix obtained from highest classifier, Neural Network (Multilayer Perceptron), is shown in Table 5.3. With further analysis from the attribute selection tool in Weka, it is shown that some of the features contribute a major part of the accurate result, and some are not contributing at all. By using Ranker attribute selection, the result shown in Table 5.4 is the list of ranking value sorted by *InfoGain* evaluation [95]. This gives a rough clue of which features contribute most to the classification accuracy.

5.4.3 Environment Exploration

Captured data points from two scenarios are shown in Fig. 5.13. It also shows the superimposed location of the actual obstacle surface. Both scenarios have approximately 160 collision points. Each colour of the points represents each surface of the learned environment. The Root Mean Square Error of the collected data compared to the nearest obstacle's surface are 26.7mm and 14.9 mm for the first and second scenario respectively.

		Predicted material				
		M_1	M_2	M_3	M_4	Total
Actual material	M_1	**299**	0	0	1	300
	M_2	0	**297**	2	1	300
	M_3	0	2	**289**	9	300
	M_4	1	0	7	**292**	300
	Total	300	299	298	303	1200

Table 5.3: Confusion matrix for the highest-accuracy classifier, Neural Network (overall 98% correct)

Ranking	Feature
0.92	Auto Correlation
0.91	Energy
0.84	Temporal Shape Statistics
0.79	f_p
0.68	Spectral Shape Statistics
0.51	Envelope Shape Statistics
0.50	Zero Crossing Rate
0.32	t_p
0.23	Spectral Rolloff

Table 5.4: *InfoGain* ranking values for the signal features used, higher values mean higher contribution to classification accuracy

Scenario	RMSE
1	26.7 mm
2	14.9 mm
Total	22.2 mm

Table 5.5: Root mean square values of the distance between the estimated environment points and the actual environment surface in blind environment exploration experiments

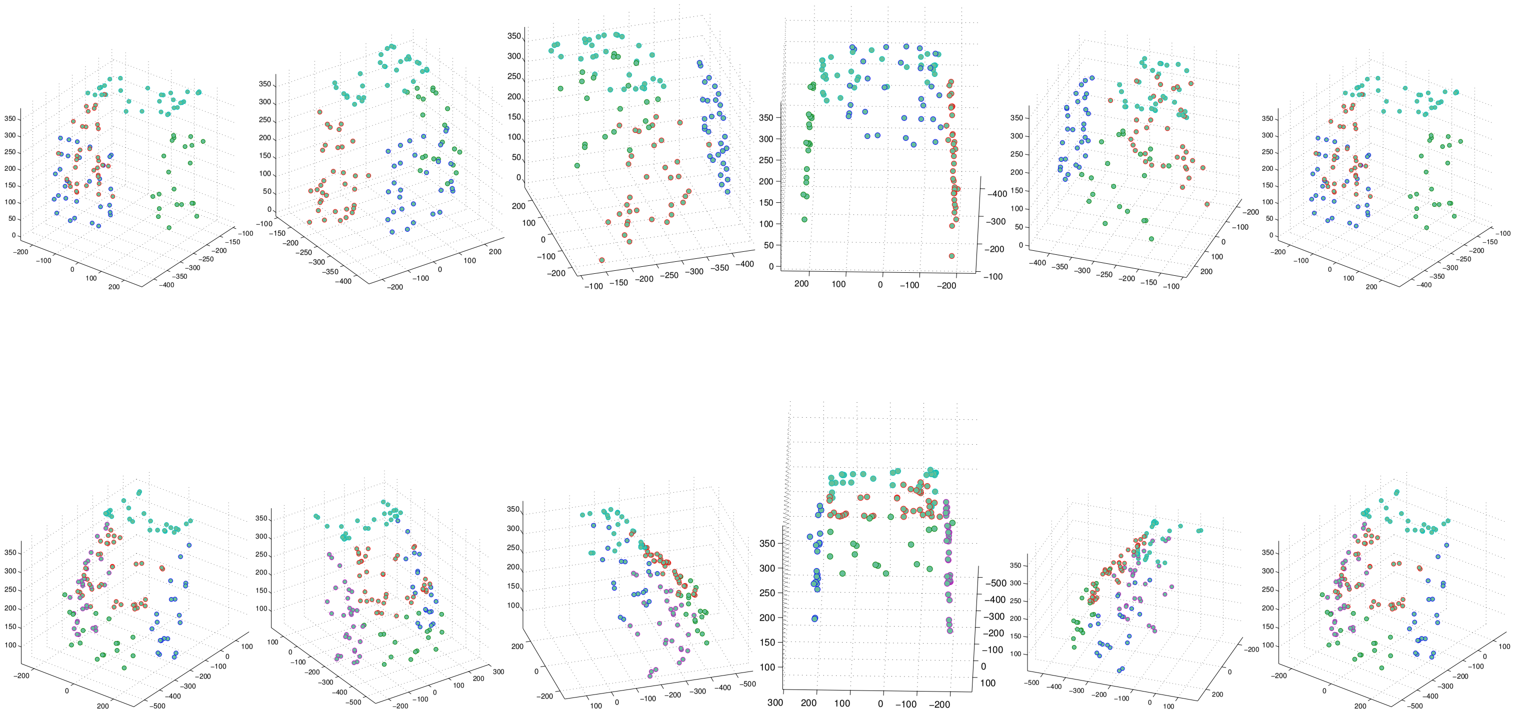

Figure 5.13: Exploration results viewed from different angles, top plots show the 1st scenario, bottom plots show the 2nd scenario, axes are in millimetres

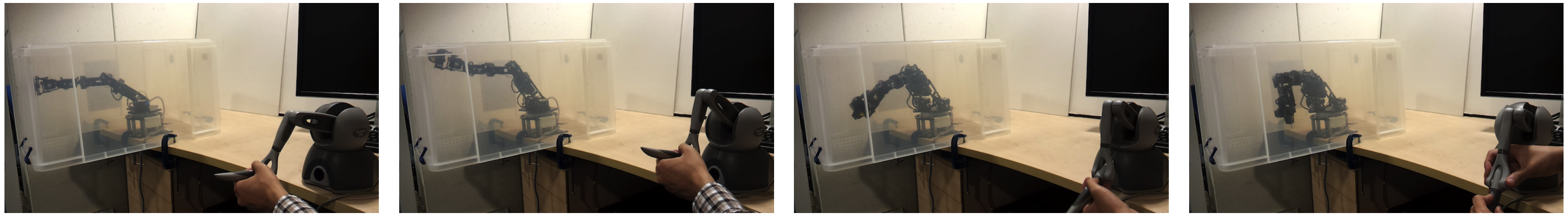

Figure 5.14: Exploration experiment image sequence, scenario 1

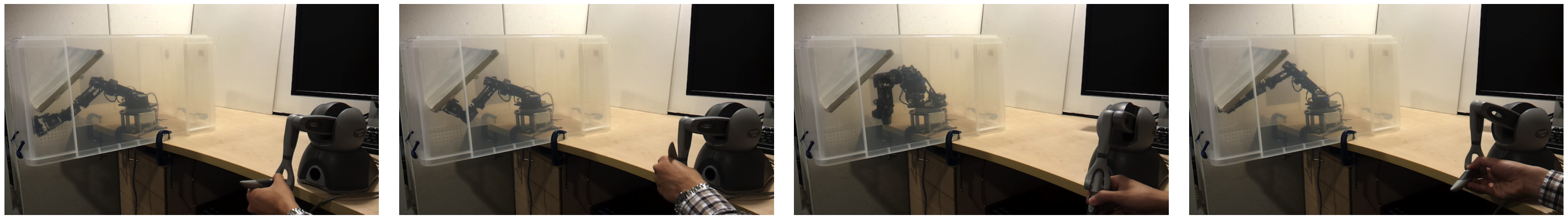

Figure 5.15: Exploration experiment image sequence, scenario 2

5.5 Conclusions

In this chapter we have presented a blind approach of collision detection for a robotic arm using accelerometers. The system detect and analyses vibration signal measured from on-board MEMS accelerometers fitted inside the actuators. The result shows that the proposed method has accurate detection (98%) while maintaining a reasonable specificity level (77%). The impact location can be also determined in terms of collided link, with a considerable accuracy. Furthermore, by using sound feature extraction and machine learning techniques, the classifier produces an accuracy of 98% for classifying four different impact materials. However, the estimation of impact direction and magnitude are not yet satisfying. This deserves further investigation. We believe that the mechanical configuration of robot makes the vibration signal distorted. Therefore, the magnitude and direction calculations can become problematic. Furthermore, there are some limitation with the presented methods. The estimated location of impact only limits the result to "the joint that collided" not "exact location of collision". All the experiements were performed with either static or slow-moving robot (less than 50 mm/s).

The experimental results demonstrated that the processed data can be used to perform environment exploration without visual sensors. When the robot hits an unknown obstacle within the environment, the location of impact point in space is calculated from the kinematics. By simultaneously moving the robot around in space to collect collision data, the point cloud of the environment is then created. The preliminary results from this experiment shows that the robot successfully mapped simple shapes by collecting around 160 data points under 3 minutes.

This chapter demonstrates how accelerometer can be used to implement a collision detection and environment characterisation on a robotic arm. The concept was tested on a small and low-cost 7-DoF robotic arm. Because of the simplicity of the MEMS sensor electronics, this technique can be applied to the Hamlyn Active Arm presented in Chapter 4, as well as any other robotic manipulators.

6 Robotic-assisted Endomicroscopy with Hamlyn Active Arm†

6.1 Introduction

Effective *in situ*, *in vivo* tumour margin definition is an important, yet unmet, clinical demand in surgical oncology. Recent advances in probe-based optical imaging tools such as confocal endomicroscopy is making inroads in clinical applications. In practice, maintaining consistent tissue contact whilst ensuring large area surveillance is crucial for its practical adoption and for this reason there is a great demand for robotic assistance so that high-speed probes can be combined with autonomous scanning, thus simplifying its incorporation in routine surgical workflows. In this chapter, a cooperatively controlled robotic manipulator is developed, which provides a stable mechatronically-enhanced platform for micro-scanning tools in performing local high resolution mosaics over 3D undulating moving surfaces. Detailed kinematic and overall system performance analyses are provided and the results demonstrate the adaptability in terms of both contact and orientation force control of the system, and thus its simplicity in practical deployment and value for clinical adoption.

In this chapter, a significant improvement over the aforementioned approaches in Chapter 2, Section 2.4 is presented as a cooperatively controlled robotic manipulator. It showcases a 3-DoF force adaptive scheme that allows complex deformable 3D surfaces to be scanned and wide area mosaics to

† Part of this chapter was initially presented at:
P. Wisanuvej, P. Giataganas, K. Leibrandt, J. Liu, M. Hughes, and G.-Z. Yang, **Three-dimensional Robotic-assisted Endomicroscopy with a Force Adaptive Robotic Arm**, in *IEEE International Conference on Robotics and Automation (ICRA)*, Singapore, 2017, pp. 2379–2384.

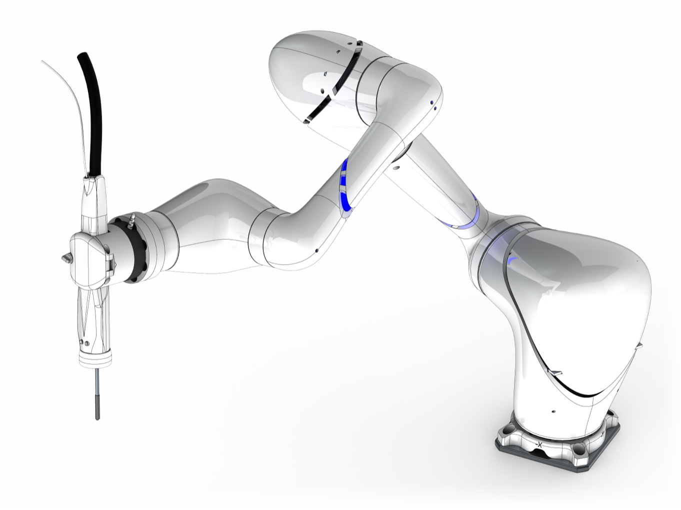

Figure 6.1: Hamlyn Active Arm with a micro-scanning robotic tool.

be generated. This robotic manipulator provides a stable mechatronically-enhanced platform for micro-scanning tools to acquire high resolution mosaics over 3D uneven moving surfaces. The force control method used to scan 3D surfaces are based on many previous works in the field, for example by *Merlet* [96], *Kazanzides* [97], and *Sudou* [98]. This chapter presents the use of 3D force control in clinical application with the experimental evaluation that shows the improved quality of the image mosaics obtained.

6.2 Materials and Methods

6.2.1 Hamlyn Active Arm

The Hamlyn Active Arm, shown in Fig. 6.1, is an articulated robot with 6 DoFs. It is actuated by brushless DC motors coupled with harmonic drive gears. Each axis is controlled by an embedded motion controller EPOS2 by Maxon motor (Sachseln, Switzerland) which perform position, velocity, and current regulations. The arm weights 3.0 kg and reaches 780 mm in a straight configuration. The drive components are chosen so that the arm can manipulate a maximum payload of 1.5 kg with limited speed and acceleration. The joints can be backdriven by the operator in case of power loss. The arm communicates via a CANopen bus with the computer system in which the control system is implemented. The control software runs on a Linux operating system which performs several tasks including: motion generation, inverse kinematics, and force control. Cartesian and joint trajectories are generated using the Reflexxes Motion Libraries [84]. In comparison to the robotic arm presented in Chapter 4, the work in this chapter utilises the same arm with a different end effector. It also uses a different mounting scheme, which resembles Fig. 4.1 (A).

6.2.2 Endomicroscopy

The microscope used in conjunction with this platform is an in-house high-speed line scanning endomicroscopy system. It can be used to obtain high-resolution images of stained tissue *in situ* through a flexible fibre bundle (probe).

The endomicroscopy system generates optically-sectioned fluorescence microscopy images at 120 fps. It consists of a Cellvizio UHD probe (Mauna Kea Technologies, France), coupled to an in-house laser scanning and detector system, described fully in [99]. The probe contains a 30,000-core Fujikura fibre imaging bundle coupled to a distal micro-objective lens, providing a FoV of approximately 240 µm, a resolution of approximately 2.4 µm (based on Nyquist criteria) and a working distance of approximately 50 µm. It has 2.6 mm maximum diameter at the distal tip and it can be used in direct contact with the tissue surface.

The endomicroscopy probe is routed through a rigid tubular channel of a micro-scanning robotic tool and fixed proximally at the entry point. The channel allows other types of probes to be used as long as their diameter is smaller than 2.8 mm. The tool is mounted on a force sensor which is attached to the end effector of the robotic arm. As a result, any force exerted at the tool tip is measured by the sensor. The demonstrated work can be used with any rigid instrument. Hence, the micro-scanning capability and further details of this tool are not presented in this work. Fig. 6.2 shows a 3D rendering of the micro-scanning robotic tool. Details on this particular micro-scanning tool can be found on [100].

The imaging system is controlled via a dedicated software interface developed mainly in Labview (National Instruments, USA). Raw images are processed in real-time to remove the pixelation artefact (honeycomb pat-

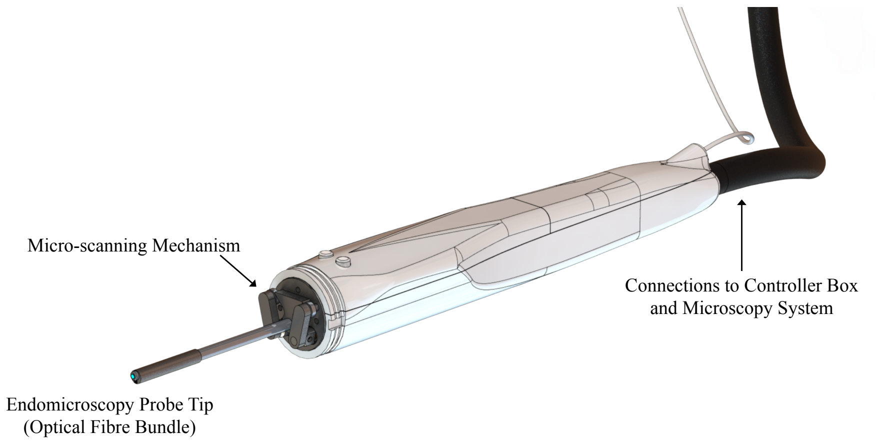

Figure 6.2: Micro-scanning robotic tool with an endomicroscopy probe inside the working channel.

tern) from the fibre cores using a Gaussian filter. A background image subtraction is then performed to remove the fluorescence signal from the optical fibres. Real-time mosaic preview (of limited size) is generated by performing a simple pair-wise registration of image frames using normalised cross-correlation (NCC), similar to [101], but is adapted to perform real-time mosaics at 120 fps. Further processing is performed to reduce the non-uniform light intensity between overlapping images using distance-weighted alpha blending. Videos are stored for post-processing to generate very large area mosaics using a similar approach.

6.2.3 Differential Inverse Kinematics†

To manipulate the 6-DoF robotic arm, a Jacobian ($\boldsymbol{J} \in \mathbb{R}^{6\times n}, n = 6$) based differential inverse kinematics is used.

$$\boldsymbol{J} = \frac{\partial \boldsymbol{x}}{\partial \boldsymbol{q}},\ \dot{\boldsymbol{x}} = \boldsymbol{J}\,\dot{\boldsymbol{q}},\ \boldsymbol{F}_x = \boldsymbol{J}\,\boldsymbol{F}_q \tag{6.1}$$

relates joint-space ($\dot{\boldsymbol{q}} \in \mathbb{R}^{n\times 1}$) velocities and task-space velocities ($\dot{\boldsymbol{x}} \in \mathbb{R}^{6\times 1}$), as well as forces and torques ($\boldsymbol{F}_x$) in task and joint space ($\boldsymbol{F}_q$).

Based on the distance between desired pose $\boldsymbol{T}_{e,d}$ and operative pose $\boldsymbol{T}_{e,t}$ an end effector velocity $\dot{\boldsymbol{x}} \in \mathbb{R}^{6\times 1}$ is calculated. The end effector velocity $\dot{\boldsymbol{x}}$ is computed based on velocity, and acceleration limiting path-planning in task space [84]. Using the pseudo-inverse Jacobian $\boldsymbol{J}^\star \in \mathbb{R}^{n\times 6}$ an update of

† This section is the work of Konrad Leibrandt. It is included in this thesis for completeness.

the joint values is performed using the update equation

$$\boldsymbol{q}_{t+1} = \boldsymbol{q}_t + \Delta\boldsymbol{q}_{t+1} = \boldsymbol{q}_t + \dot{\boldsymbol{q}}_t\Delta t, \tag{6.2}$$

where the joint velocity is calculated as,

$$\dot{\boldsymbol{q}}_t = \boldsymbol{J}^\star\,\dot{\boldsymbol{x}}_t. \tag{6.3}$$

The standard iterative Newton-Raphson method is chosen to optimise the joint values such that the desired end effector pose is reached [86].

In each iteration, joint values are computed using the DLS inverse Jacobian ($\boldsymbol{J}^\star$):

$$\boldsymbol{J}^\star = \boldsymbol{V}\,\mathrm{diag}\left(\hat{\sigma}_1^{-1}, \ldots, \hat{\sigma}_n^{-1}\right)\boldsymbol{U}^T,\ \boldsymbol{J}^\star \in \mathbb{R}^{n\times 6}, \tag{6.4}$$

where $\boldsymbol{V}$, $\boldsymbol{U}$ are the right and left singular vectors obtained by a singular value decomposition (SVD) of the Jacobian, i and j are indices of the singular values, and $\hat{\sigma}_i^2$ are the i^{th} damped eigenvalues calculated as,

$$\hat{\sigma}_i = \begin{cases} \sigma_i & \text{, if } \min\limits_j\left(|\sigma_j|\right) \geq \sigma_{\min} \\ \left({\sigma_i}^2 + {\lambda_t}^2\right){\sigma_i}^{-1} & \text{, else} \end{cases}, \tag{6.5}$$

and where

$${\lambda_t}^2 = {\lambda_{\max}}^2\big(1 - \big(\min_j(|\sigma_j|)\big)^2{\sigma_{\min}}^{-2}\big), \tag{6.6}$$

$i, j \in \{1, \ldots n\}$, and $n = 6$. For critically low singular values of the Jacobian, smaller than $\sigma_{\min}$, this approach provides damping to avoid high joint velocities. Otherwise, the damping is not applied when singular values are sufficiently large. This optimisation takes ~10 µs per iteration to compute.

6.2.4 Workspace Analysis

The dexterity of the robot is depending on the placement of the scanning probe within the workspace of the robot. To ensure precise motion and a fast converging inverse kinematics, a probe placement within workspace volumes of high dexterity is desirable. The dexterity measure $\mathcal{D}$ is based on the manipulability measure:

$$\mathcal{M}(q) = \sqrt{|\boldsymbol{J}(\boldsymbol{q})\boldsymbol{J}(\boldsymbol{q})^T|}, \tag{6.7}$$

and augmented by the joint limit measure:

$$\mathcal{L}(q) = 1 - \exp\left\{-\kappa \prod_{i=1}^{n} \frac{(q_i - q_{i,\min})(q_{i,\max} - q_i)}{(q_{i,\max} - q_{i,\min})^2}\right\}, \tag{6.8}$$

such that it is obtained as:

$$\mathcal{D}(q) = \mathcal{L}(q)\,\mathcal{M}(q), \tag{6.9}$$

and where $q_{i,\min}, q_{i,\max}$ are the lower and upper joint limits of the i^{th} joint respectively [102]. A workspace analysis, depicted in Fig. 6.3, was conducted to allow an optimum placement of the robotic system to the target anatomy.

The analysis is obtained by calculating the dexterity measure $\mathcal{D}$ for 10^{10} random robot configurations. In Fig. 6.3, each voxel of 6-millimetre edge represents the maximum dexterity of configurations whose end effector position falls into it. The dexterity measure is not symmetric about the z-axis due to the limits of the base joint. Hence, the front-facing configurations have higher dexterity than rear-facing ones.

6.2.5 Contact Force and Orientation Control

The quality of microscopic image and the visibility of cellular structures are highly dependent on the probe-tissue contact force during image acquisition. A study has shown that the range of acceptable contact force is in the region of 5 mN–500 mN [103]. Maintenance of the probe orientation to be perpendicular to the contact surface can also drastically improve the image quality. For the robotic arm to be able to maintain the correct orientation with a steady contact force, a Mini40 force/torque sensor (ATI Industrial Automation, USA) is incorporated at the end effector. The sensor can measure torques as high as 1 Nm with 125 µNm of resolution and forces as high as 20 N with 5 mN of resolution, which is within the optimal range for endomicroscopy imaging. The force/torque data is sampled and converted with a data acquisition PCI adapter (National Instrument, USA) running at 32 kHz sampling rate. The digitised data is then filtered with an infinite impulse response (IIR) low-pass filter.

Fig. 6.4 presents the placement of the endomicroscopy probe and the force/torque sensor with respect to the Hamlyn Active Arm. The tool

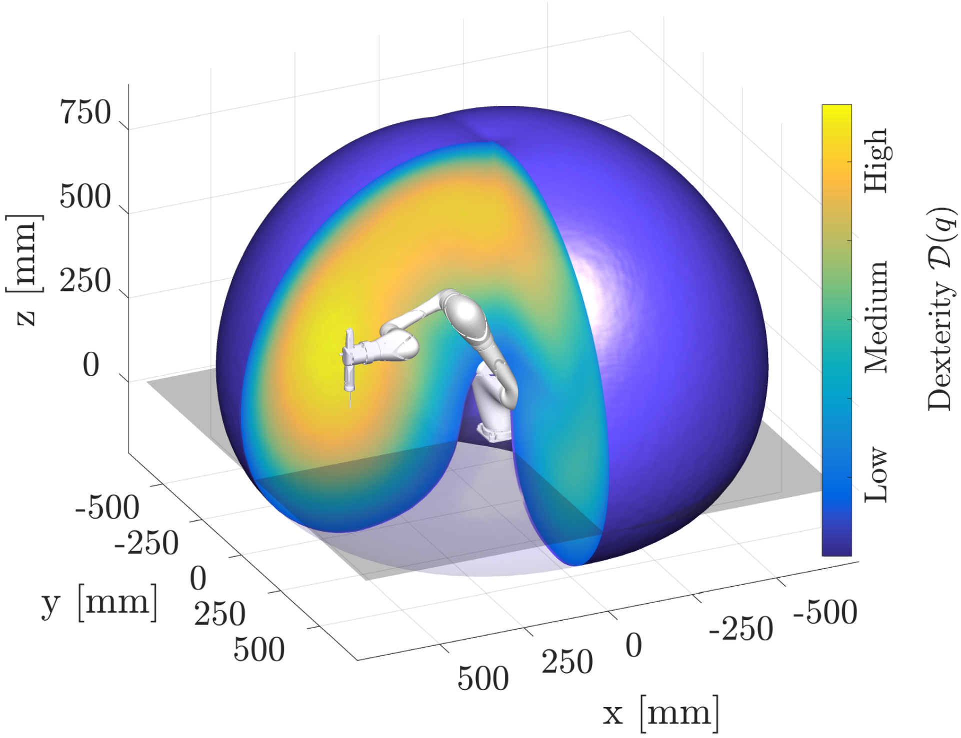

Figure 6.3: Dexterity of the manipulator with the scanning probe within the reachable workspace calculated using the dexterity measure $\mathcal{D}$ in (6.9).

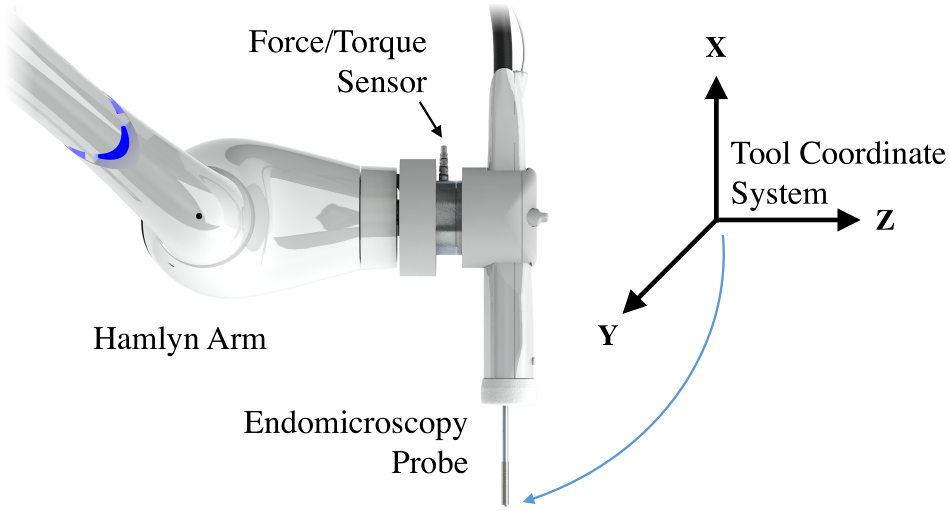

Figure 6.4: Placement of the microscopy probe and the force/torque sensor at the end effector. A tool coordinate system is defined at the tip.

reference frame of the robot is defined at the tip of the imaging probe, where the x-axis is defined along the shaft of the probe. The z-axis is parallel to the normal of the end effector flange. During a scan, the probe automatically translates along the x-axis to establish a contact to the tissue. The orientation controller rotates the tool about the y, z axes. Translation in yz-plane is manually controlled by the operator according to the area of interest.

The contact force exerted axially on the shaft of the imaging probe is regulated by a closed-loop controller. This controller translates the imaging probe along the shaft in order to maintain the desired force. The block diagram of the force controller is shown in Fig. 6.5. The contact force is measured and compared with the desired force. The difference is then fed into a Proportional-Integral-Derivative (PID) controller through a clamp function, which limits the amount of this input to a predefined range to prevent large movements in events of contact with excessive force. The output of the PID controller is then used to set the translation velocity of the probe V_x.

The reference frame of the force/torque sensor is located at the middle of the microscopy probe and intersects with the x-axis of tool. When a perpendicular tool contact is established, the contact force that acts on the probe shaft is parallel to the shaft itself. Hence, there is no torque exerted at the reference point. However, when the probe orientation is not parallel to

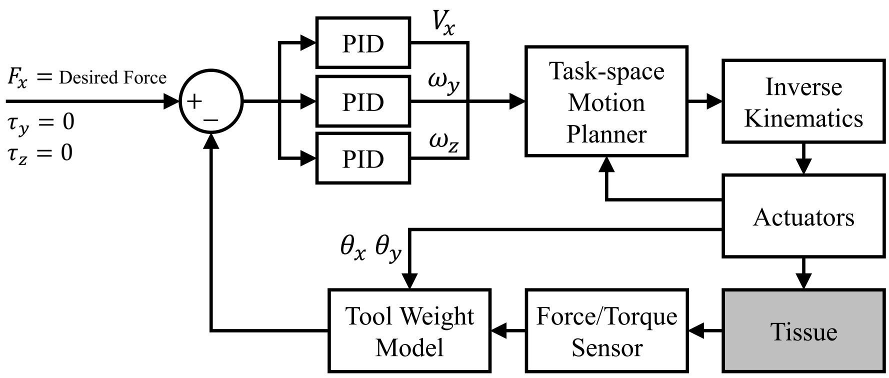

Figure 6.5: Architecture of the 3-DoF force and orientation controller.

independent closed-loop controllers. The architecture of these controllers are similar to the contact force controller as shown in Fig. 6.5. The torque feedbacks τ_y and τ_z are used to set the angular velocities of the probe, ω_y and ω_z respectively. The torque setpoints for the orientation controller are zero in order to maintain perpendicular probe contact to the tissue surface. The friction from translational movement of the probe along the surface can also contribute to these torques as well, which could trigger the unnecessary rotational movement. However, from the experimentatal data, a linear scan of a flat porcine tissue surface caused negligible amount of torques compared to a scan on a curved tissue surface. Therefore, a deadband is used to filter out the torque caused by friction from translational movements.

The scanning operation is semi-autonomous. The user controls two-dimensional (2D) translation of the tool in yz-plane with respect to the *Tool Coordinate Frame.* The robot adapts the tool in 3D: x-translation and θ_y and θ_z rotations. The roll of the tool, θ_x, is fixed. In addition to the semi-autonomous scanning mode, all the 6 DoFs can be manually controlled as well. The user interface is a wireless game controller with buttons, analogue sticks, and analogue triggers.

6.2.6 Modelling and Calibration

With the placement of the force/torque sensor between the end effector and the microscopy probe, the sensor measures not only the contact force/torque, but also the weight of the tool itself. The tissue contact force required for microscopy is in the range of 50-100 mN. On the other hand, the weight of the tool is in a much larger range of 3-5 N. Before performing a scan, an initial bias value is applied to the force/torque acquisition system to subtract this amount of force. However, this bias value is dependent on the tool orientation since the probe's centre of mass is not at the reference point of the sensor. In order to get a useful contact force information to make the force control scheme effective, the variations of force and torque due to gravity are modelled and subtracted out from the measurements. Different cabling and attachment schemes can also affect the behaviour of this orientation-dependent offset. Based on these scenarios, a calibration method is implemented to model the baseline correction.

For the calibration, the tool is positioned in a dexterous region of the workspace with a sufficient clearance from the surrounding to eliminate external contact force. At this initial position, bias values are subtracted from the force/torque measurements. Then the tool is rotated arbitrarily along y and z axes about the tip while the force/torque data is recorded. The movement is performed throughout the available workspace of those two DoFs. Since this model is gravity dependent, the orientation parameters are defined as the angles of the tool with respect to the gravity vector. The robotic arm is assumed to be grounded. The orientation of the tool shaft (x-axis), θ_x and θ_y, correspond to the angle between the shaft and the gravity vector projected onto the xz- and yz-plane in the world coordinate system (Fig.6.3) respectively. In this setup, only the force and torques used for the closed-loop controllers are of interest for modelling. The gravity-related force F_x and torques τ_y, τ_z are defined as functions of θ_x, θ_y. The offset force/torque models are then generated from collected data using polynomial regression.

6.3 Experimental Results

6.3.1 Microscopy Probe Weight Modelling

The trajectory for the calibration is preprogrammed to move the probe throughout the available workspace. The same trajectory is repeated five times and was performed under five minutes. Each dimension of the collected data according to section 6.2.6 is fitted to a surface defined by a polynomial equation using regressions. From the experiment, F_x fits well with a second-degree polynomial, whereas τ_y,τ_z fit well with first-degree polynomials, which are shown in Fig. 6.6. The RMSE of the fits are 3.60 mN, 0.849 Nmm, and 0.256 Nmm respectively. The comparison before and after applying the correction model for F_x is shown in Table 6.1 and Fig.6.7. This comparison was performed on a separate test data. It was collected from a trajectory manually generated by a user input.

6.3.2 Force Controller

A bench test was performed with a silicone tissue phantom in order to evaluate the response of the force controller. In this experiment, the Hamlyn Active Arm with the micro-scanning tool performs a contact force control

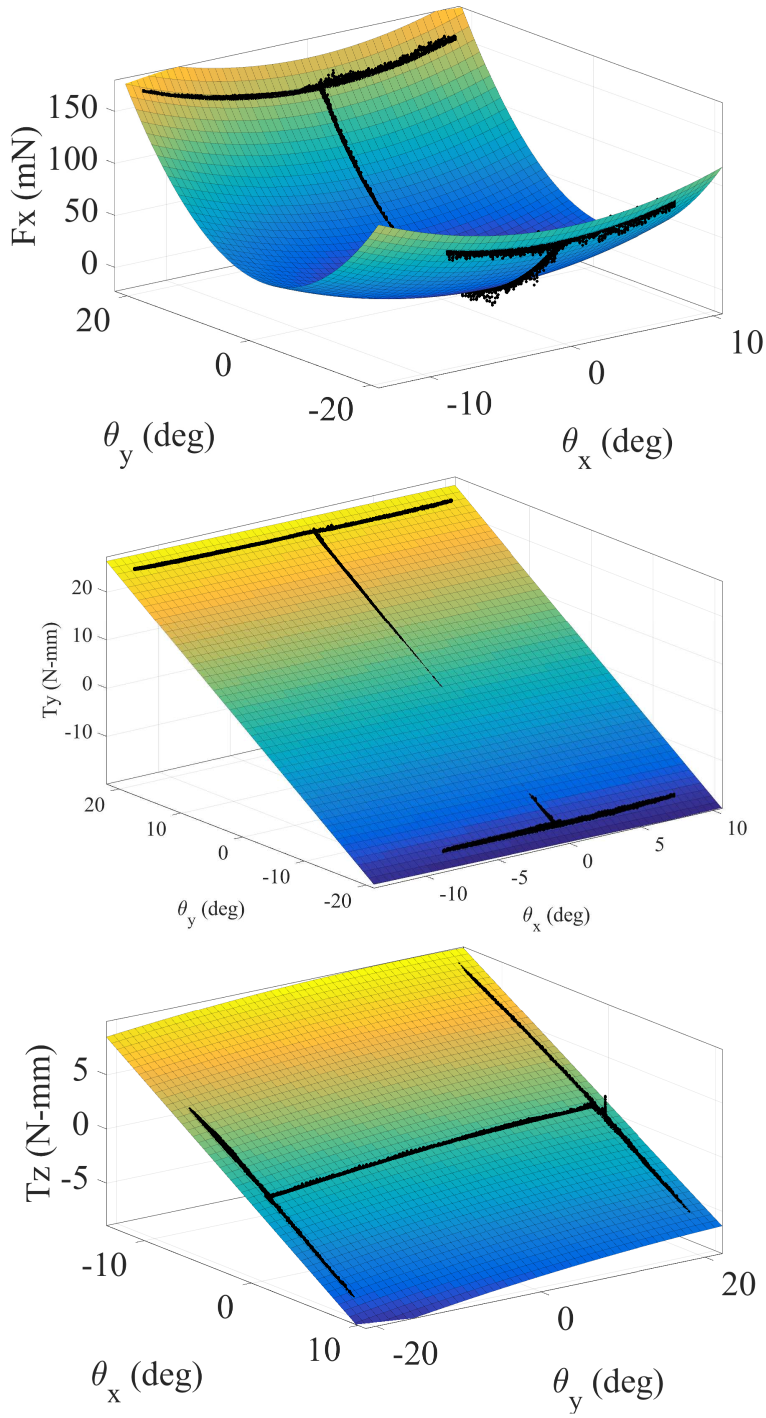

Figure 6.6: Calibration of the probe offset weight in different sensor axes (F_x,τ_y,τ_z) due to orientation changes. The black dots represent the measurement from the force/torque sensor using preprogrammed trajectory with five repetitions. The fitted models are shown with coloured surfaces.

Table 6.1: Comparison of probe weight compensation results between the measured and corrected values of force and torques.

	Range		Average	
	Measured	**Corrected**	**Measured**	**Corrected**
F_x (mN)	176.2	14.1	77.6	-0.0020
τ_y (N-mm)	42.2	3.5	3.1	0.0047
τ_z (N-mm)	16.6	1.6	0.083	-0.000028

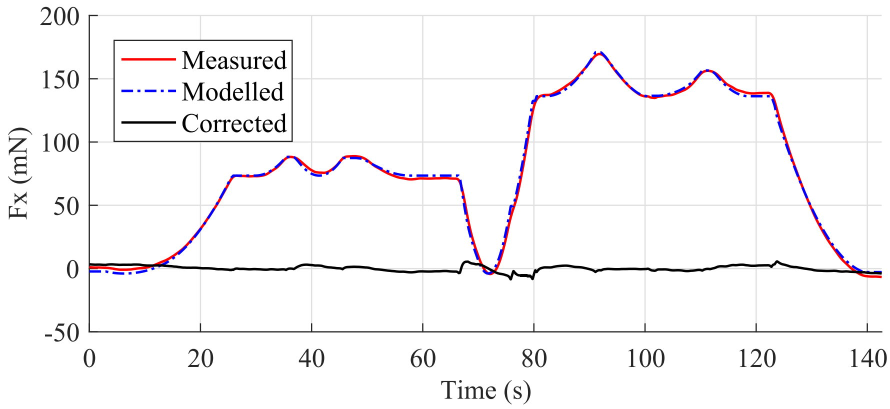

Figure 6.7: Comparison of the measured force, modelled probe weight, and the corrected force F_x during orientation changes.

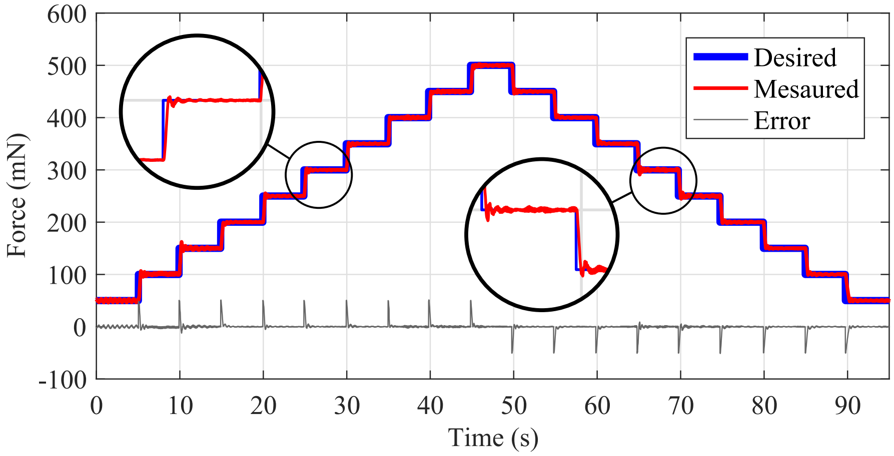

Figure 6.8: Step response from the contact force controller on a tissue sample, showing the desired contact force, the measured force, and their difference.

in a configuration similar to Fig. 6.3. The tool weight model is calibrated to eliminate the force offset due to the gravity. The force controller is then activated with varying setpoints from 50 to 500 mN. The step response of the force controller is shown in Fig. 6.8. This shows that the robotic system is capable of maintaining constant contact force to the tissue within a practical force range and be able to instantaneously change the amount of force as required.

6.3.3 Wide-area Microscopy Scanning

The robotic-assisted endomicroscopy system is tested on a porcine stomach tissue sample, shown in Fig. 6.9a. The task for this experiment is to complete a straight line scanning on a spherical tissue surface. It is performed with 3 modes: *A) 3D Contact Force and Orientation Control*, *B) one-dimensional (1D) Force Control*, and *C) Manual Control*. In the first mode, all the closed-loop controllers in Fig. 6.5 are used as the user moves the probe across the sample in xy-plane. In *Mode B*, only the contact force control is activated with a fixed vertical probe pose. Lastly, in the manual mode, the operator controls all 5-DoF movements $(x, y, z, \theta_y, \theta_z)$ of the robotic arm. Since our aim is to obtain high quality images and also large area mosaics, the quality of mosaicking is selected to evaluate the performance of each experimental mode. Image quality can be derived not only using image criteria, such as entropy or blur metrics, but also using the NCC metric. The closer the NCC value is to 1, the better is the correlation between sequential images. It is a factor that gives an estimation for the quality of microscopic mosaics since these values are used as thresholds to discard low quality image pairs during mosaicking. The results of this comparison between control modes are presented in Fig. 6.10 in the form of histograms of the NCC values over a line scanning task. Also, the percentage of frame pairs that have NCC values more than 0.8 and 0.85 are calculated. As the speed is kept approximately the same in all trials, the overlap percentage is the same and therefore it has little effect on the comparison results.

As presented, *mode A*, where both the contact and the orientation of the tool are controlled, results in higher overall NCC value with a mean of 0.89. Also, 90.2% of the frame pairs have NCC values higher than 0.8. In comparison, *mode B*, where the probe orientation is fixed, the mean of the NCC value is 0.85 and the percentage of frames with NCC value greater than 0.8 is 80.8%. Finally, when the user has fully manual control of the robotic arm, the mean value of the NCC is 0.83 and approximately 75.2% of image pairs have NCC value greater than 0.8.

The generated image mosaics from the experiment are presented in Fig. 6.11. Due to size constraint, only parts of the overall mosaic images are presented here. As it is demonstrated, in accordance with Fig. 6.10, the mosaic image generated using both contact and orientation control presents better uniformity and enhanced contrast. However, the mosaic where the robotic arm is controlling only the contact presents distorted cell structure and blurriness in the beginning due to the lack of perpendicular orientation to the surface. This enhances the initial aim of this work that focuses on compensating not only for axial forces but the 3-DoF contact and orientation. Finally, the *Manual Control* mode generates non-uniform mosaics with non-consistent appearance as the operator failed to compensate for the 3D surface irregularities.

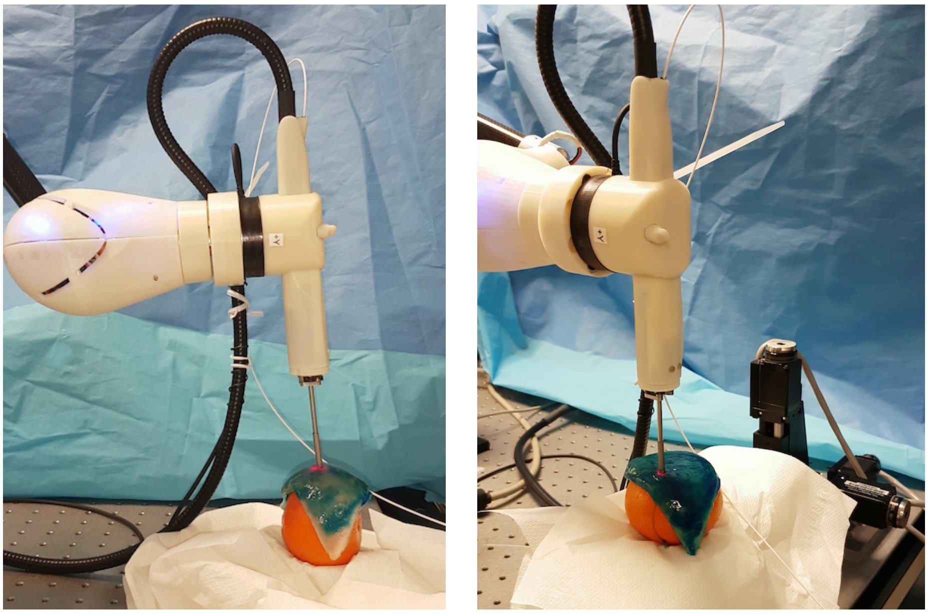

(a) stationary (b) with a moving platform

Figure 6.9: Experimental setups of the line scanning microscopy on a porcine tissue with a spherical surface.

6.3.4 Motion Compensation

An experimental setup, as presented in Fig. 6.9b, is created to replicate the conditions encountered during *in vivo* examinations. The platform moves up and down repeatedly every 6 seconds with speeds of 1.00, 1.25, and 1.87 mm/s. Fig. 6.12 shows the performance of the force controller to track the movement while the desired contact force is set to 50 mN. The disturbance generated from the platform is compensated by the system with deviations of 8 mN at lower speeds and 15 mN at the highest speed.

6.4 Conclusions

This work presents a cooperatively controlled robotic manipulator with 3-dimensional force adaptive control scheme. The system is equipped with a micro-scanning endoscopy probe allowing a wide area "optical biopsy" to be performed on an arbitrary 3D surface.

The robotic system automates the movement in 3 DoFs by three indepen-

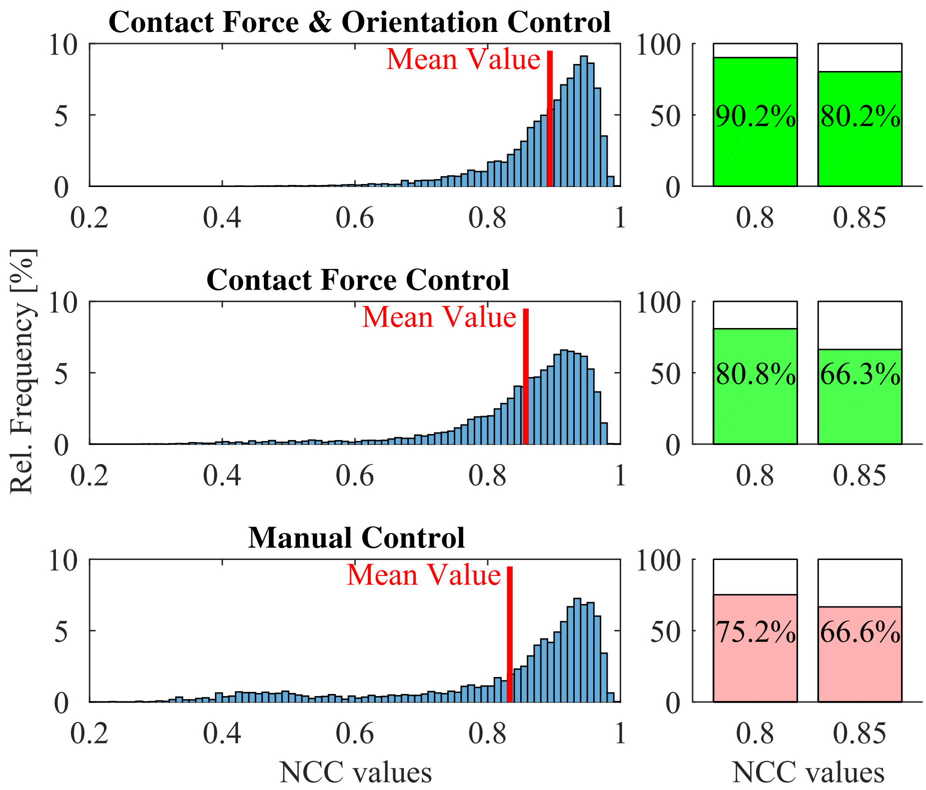

Figure 6.10: Comparison of the NCC values from the mosaicking process between different control schemes applied during scanning.

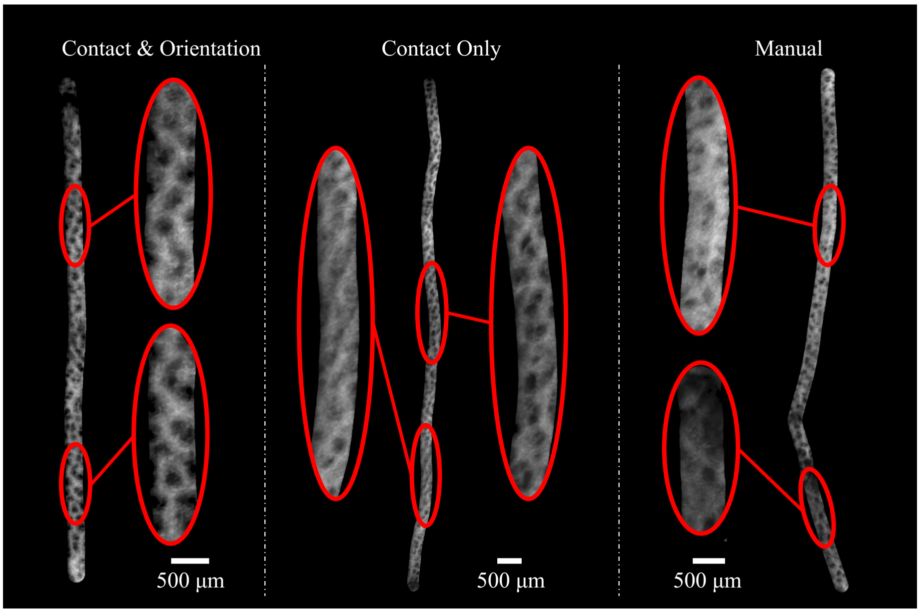

Figure 6.11: Comparison of mosaicking results from endomicroscopy scanning with different control schemes.

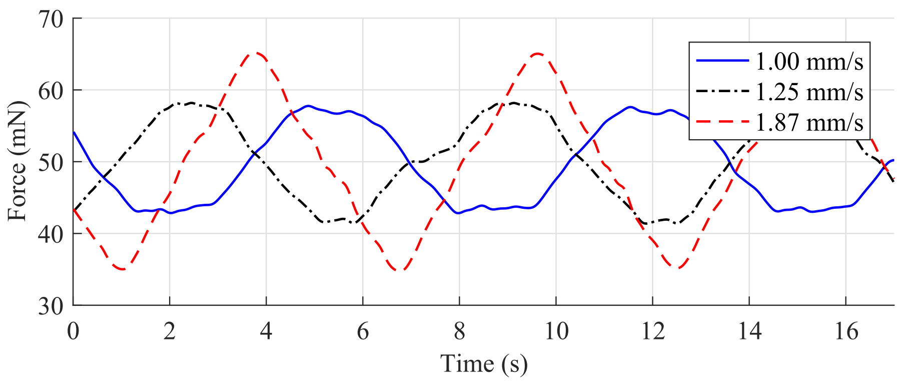

Figure 6.12: Comparison of responses from the contact force controller on a moving tissue sample at different speeds. The setpoint is at 50 mN.

dent closed-loop controllers while the other 2-DoF translation is manually controlled by an operator to generate a scanning pattern according to the region of interests. An incorporated 6-axis force/torque sensor provides high-resolution measurements for the feedback controls. Compensation of the tool weight during orientation changes are modelled with calibration that can be performed before the scan, which allows accurate force control within $14\,mN$ over the range of the robot's workspace. Experimental results show that the image mosaicking with 3D force controller system performs better than the system with only 1D force controller or with manual control.

Handling deforming, undulating surfaces during oncological surgery requires careful manual manipulation of imaging probes such as the pCLE and this adds operator burden and has been one of the limiting factors for routine clinical adoption of these new imaging technologies. The proposed scheme caters for both automatic contact and orientation force control and therefore is significantly simpler than existing robot assisted scanning schemes. This practically allows the operator to "point and scan" allowing consistent large area surveillance via automatic image mosaicking. The dexterous arm used in this paper allows fully cooperative control and therefore can cover large anatomical regions whilst offering flexibility in robotic arm configuration. With increasing drive towards early and precision intervention in surgery, the proposed platform demonstrates a ideal synergy of human control and robotic assistance. In oncological surgery, this allows the surgeon to focus on operative tasks while imaging probes can assist seamlessly for detailed tissue characterization *in situ, in vivo*, without interrupting the normal surgical workflow, with autonomy but still under the easy command of the surgeon.

7 Master Manipulator for Teleoperation of Single Access Surgical Instruments†

7.1 Introduction

The performance of a master-slave robotic system depends significantly on the ergonomics and the capability of its master device to correctly interface the user with the slave robot. Master manipulators generating commands in task space represent a commonly adopted solution for controlling a range of slave robots while retaining an ergonomic design. However, these devices present several drawbacks, such as requiring the use of clutching mechanics to compensate for the mismatch between slave and master workspaces, and the lack of capability to intuitively transmit important information such as specific joint limits to the user. In this chapter, a novel joint-space master manipulator is presented. This manipulator emulates the kinematic structure of highly flexible surgical instruments which it is designed to control. This system uses 6 active DoFs to compensate for its own weight by utilising its dynamic model, as well as to provide force feedback corresponding to the slave robot's joint limits. A force/torque sensor integrated at the end effector is used to relay user-generated master forces and torques directly to specific joints. This is performed to counteract the friction stemming from structural constraints imposed by the kinematic design of the instruments. Finally, a usability study is carried out to test the validity of the system, proving that the instruments can be intuitively controlled even at the extremities of the workspace.

† Part of this chapter was initially presented at:
P. Wisanuvej, G. Gras, K. Leibrandt, P. Giataganas, J. Liu, and G.-Z. Yang, **Master Manipulator Designed for Highly Articulated Robotic Instruments in Single Access Surgery**, in *IEEE/RSJ International Conference on Intelligent Robots and Systems (IROS)*, Vancouver, 2017, pp. 209–214.

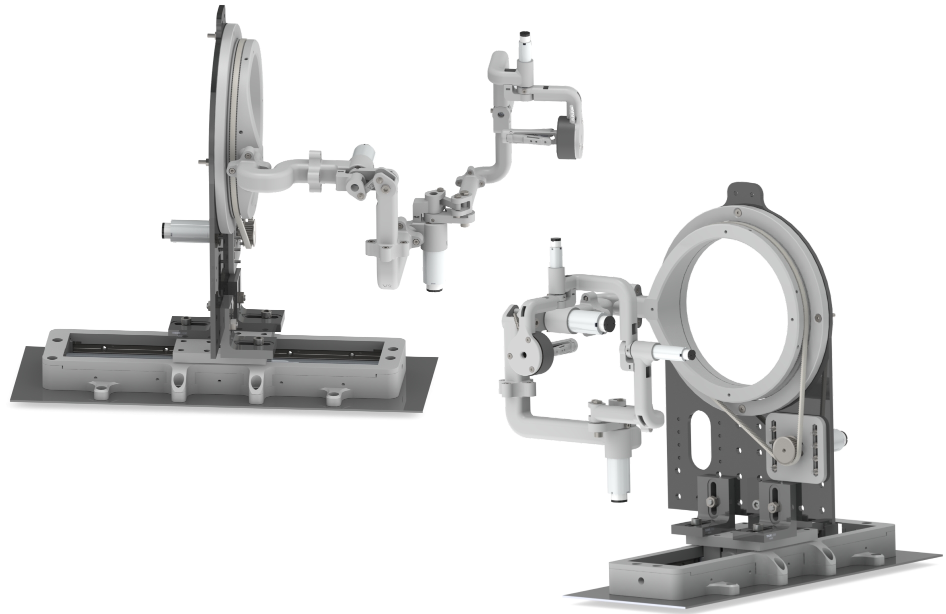

Figure 7.1: Different viewpoints of the proposed master manipulator.

In this chapter, a novel master manipulator for joint-space control is presented. This device is designed for use with highly articulated instruments in TEM. The device possesses 6 active DoFs and a gripper, for a total of 7 DoFs. The design of the master manipulator allows the user to cover the entire workspace of the instruments without clutching. Furthermore, all the active DoFs are used to render joint limits on the master device, granting the user an intuitive understanding of the state of the instruments. Standard master devices employ mechanical structures designed to limit the friction and resistance felt by the user. This approach is not possible here as the structure of the master device is dictated by the kinematics of the robot. To overcome this issue, a force/torque sensor located at the finger grips is used to compensate for the excessive friction and weight presented in some joints. Lastly, a usability study is carried out to characterise the performance of the system. In order to compare the proposed device, two master manipulators operating in task space with delta platforms: omega.7 and sigma.7 haptic devices (Force Dimension, Switzerland) are chosen for comparison. These delta manipulators are the actual manipulators used to control the slave surgical system.

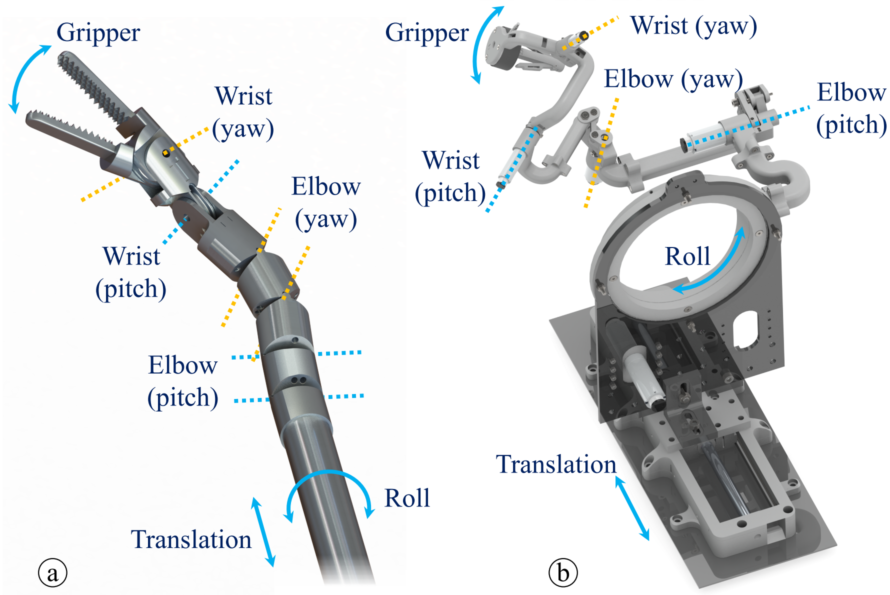

Figure 7.2: Joint control mapping of (a) the highly articulated robotic instrument to (b) the master manipulator. The corresponding axes of rotation and translation are shown.

7.2 Manipulator Design

The design of the master manipulator is shown in Fig. 7.1. This section describes the surgical instrument, the hardware design, workspace analysis, control system, and experimental results of the presented master manipulator.

7.2.1 Surgical Instrument

The slave surgical instrument [15] used in conjunction with the master manipulator is part of a robotic surgical system targeted for use in a TEM operation*. Full details of the overall surgical system are described in [13, 18]. The instrument shown in Fig. 7.2 (a) and Fig. 7.3 (a) consists of a cylindrical shaft, articulated elbow segments, a wrist, and a gripper. This encompasses 7 active joints plus 2 passive joints which are 1:1 coupled with the active ones within the same pair (dependent joints). Referring to Fig. 7.3 (a), Elbow joint 1A is coupled to Elbow joint 1B, *i.e.* the joint values are linked

*The design and development of the surgical instrument is the work of *Carlo A. Seneci* and *Jianzhong Shang et al.*

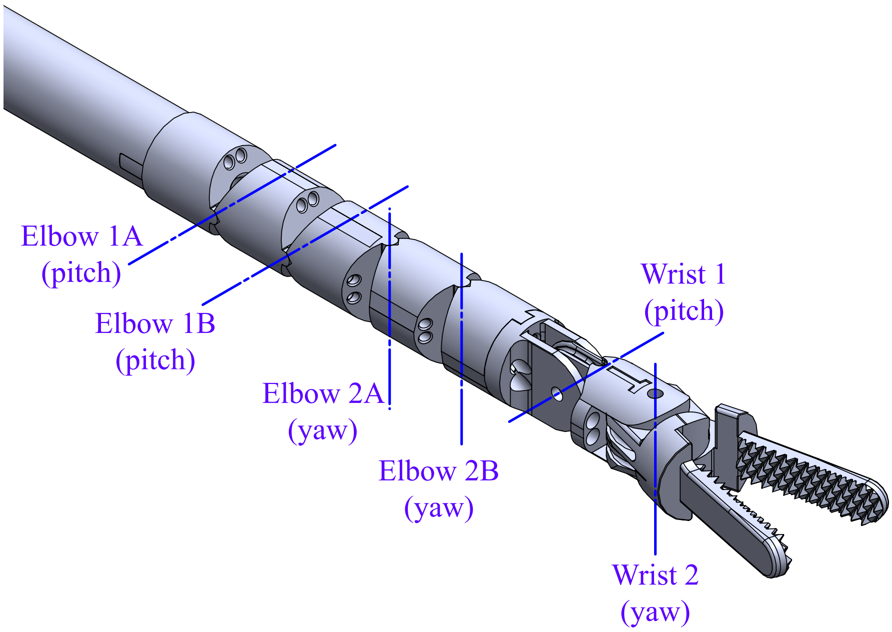

(a) Surgical Instrument

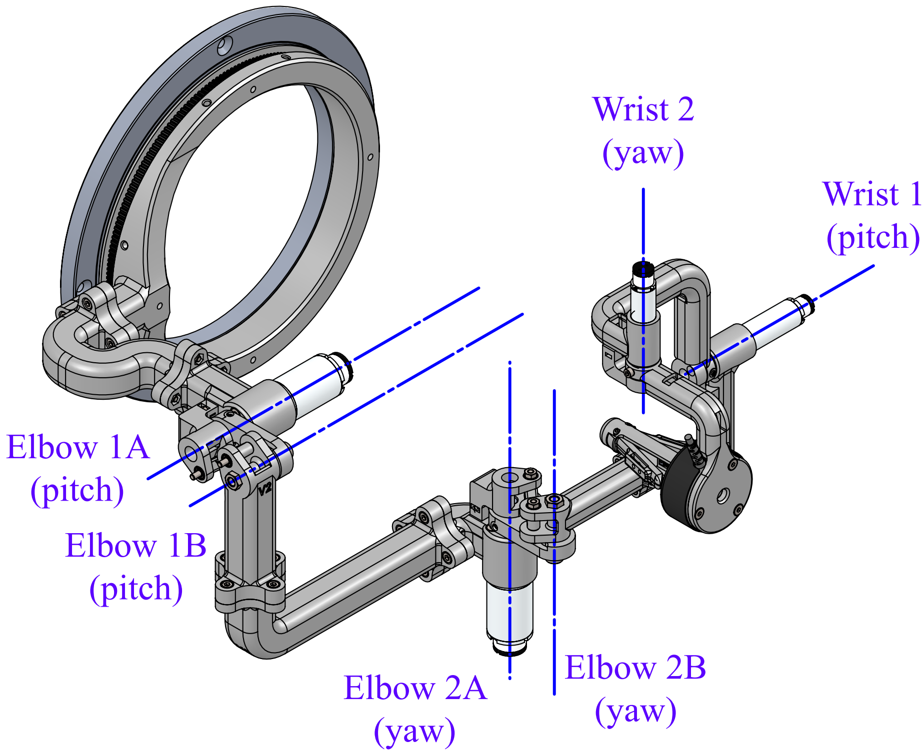

(b) Master Manipulator

Figure 7.3: Rotational axes of the articulated sections of the slave instrument, and the corresponding axes on the master manipulator (for simplification, some components are not shown).

together via the driving mechanism. The same applies to Elbow joints 2A and 2B. The dependent joint design was chosen in order to reduce the number of actuators while maintaining the range of motion. The dimensions and manufacturing process of the tool is iteratively optimised to accommodate the workspace and forces required by the surgical procedure [104].

7.2.2 Hardware Design

As the master manipulator is designed to work in joint-space control, the kinematic structure of the device is dictated by the surgical instrument. Fig. 7.2 and Fig. 7.3 shows the correspondence between the master and slave devices. Since the manipulation of both devices is mapped directly in the joint space, no clutching is required during operation. This imposes a fixed motion scaling for the telemanipulation. The scaling factor is selected so that the overall length of the device is within the motion range of an average human forearm. This results in the scaling factor of 5:1 with 300 mm being the overall length of the manipulator. The proximal end of the manipulator has a large hollow structure for controlling the roll axis of the surgical instrument. It is made from a slewing ring bearing which can handle large amount of radial load *i.e.* the entire weight of the articulated sections. This ring structure allows user to put his/her arm through the centre of the device and hold the finger grips to manipulate the end effector. It also serves as an arm rest.

Each active rotational joint of the master manipulator is actuated by a DC motor with an integrated gearhead and an incremental encoder (Maxon motor, Switzerland). The reduction ratios are chosen high enough so that the motor can produce sufficient torque to counter the gravity load and render the forces to the user, but also not too high so that they can be backdriven. The device can produce at least 5 N of force at the finger grips in any position inside the workspace while operating in a gravity compensation mode. The translation stage is powered by a linear DC-Servomotor (Faulhaber, Germany), which can produce enough force required for friction compensation while holding the load from all the rotational joints above it. Finger grips are fitted at the end effector that the user holds and manipulates the device. The gripper consists of two spring-loaded passive joints coupled together with a gear mechanism. A small neodymium magnet disk

(Radial Magnets, USA) is embedded in one lever. The grip angle can be measured using a Hall effect sensor, A1326 (Allegro MicroSystems, USA), integrated in the middle of the end effector. A Mini40 6-DoF force/torque sensor (ATI Industrial Automation, USA) is integrated at the end effector to assist in the friction compensation of certain joints, as presented in section 7.3.3. The detailed assembly of the finger grips is presented in Fig. 7.4.

7.2.3 Grip Angle Sensing

To measure the grip angle, the voltage V measured from the Hall effect sensor is converted to the distance between the magnet and the sensor $(A+B)$ based on a calibrated model. The model is obtained from a regression technique. Various linear and nonlinear regressing models were tested (polynomial, exponential, fourier, gaussian, and power models) and the best result with the least RMSE was obtained using a *4-term Gaussian model* (7.1). Fig. 7.5 shows a dataset collected from an experiment. The calibration is performed only once. The grip angle θ is then calculated (7.2) from the geometric parameters of the finger grips illustrated in Fig. 7.6.

$$y = \sum_{i=1}^{n} a_i e^{\left[-\left(\frac{x-b_i}{c_i}\right)^2\right]} \tag{7.1}$$

where x is voltage, y is $A+B$, and $n=4$.

$$\theta = sin^{-1}\frac{B+C}{D} \tag{7.2}$$

7.2.4 Dependent Joint Designs

Different approaches to emulate the behaviour of the instrument's dependent joints were explored, as presented in Fig. 7.7. The first method uses a series of gears placed along the link to couple the joint angle from the active joint to the passive one. This can be implemented using mostly off-the-shelf components. However, it limits the possible combinations of link lengths due to the limited availability of gear pitch and number of teeth. Additionally, this can only be done with an even numbers of gears to achieve the correct rotational direction. Adding multiple gears can also introduce significant backlash to the system. Alternatively, a cross-tendon mechanism

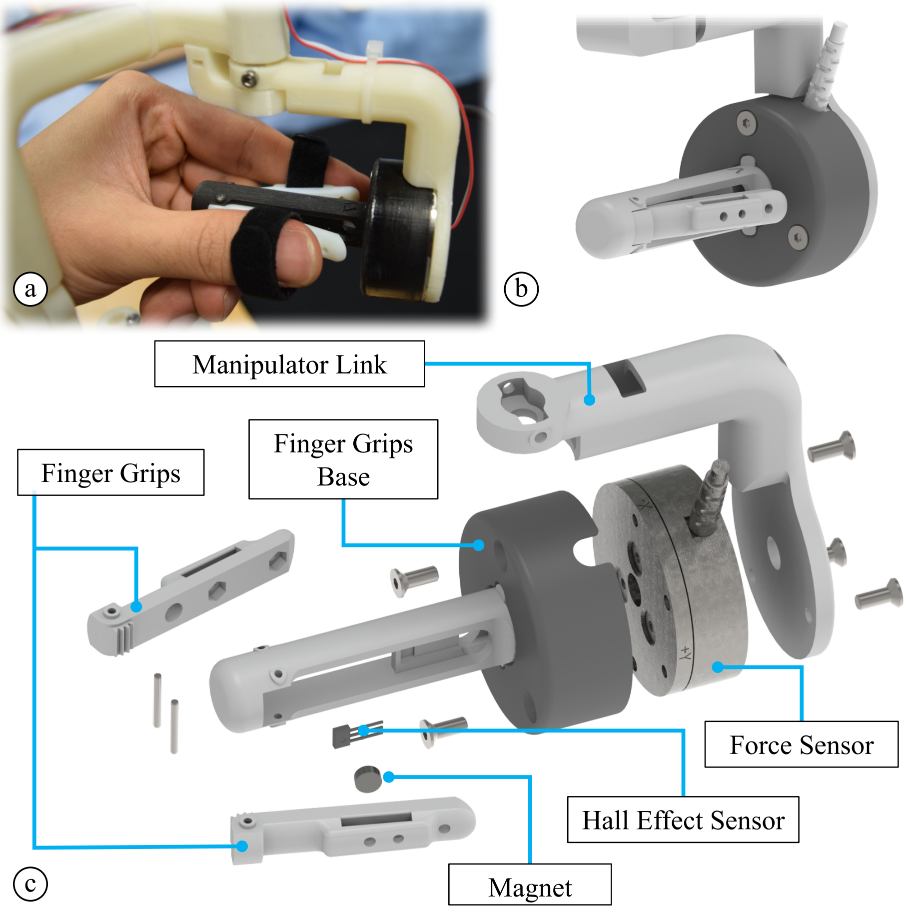

Figure 7.4: Master manipulator's finger grips design; (a) operator while manipulating the finger grips, (b) CAD rendering of the finger grips, and (c) exploded view presenting the magnet and the Hall effect sensor for position sensing and the integrated force sensor to facilitate the manipulator's motion.

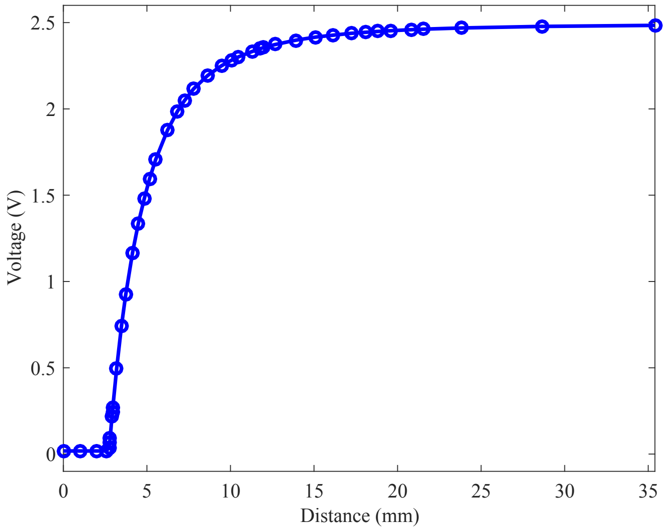

Figure 7.5: Distance-voltage data collected from an experiment, 42 data points in total.

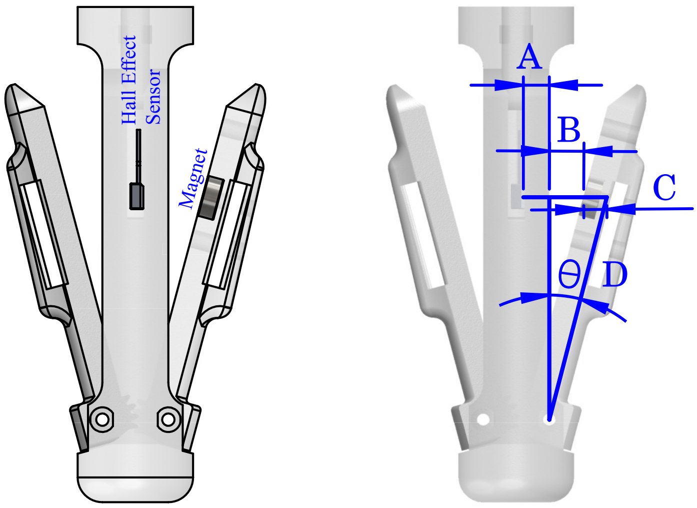

(a) components (b) geometric parameters

Figure 7.6: Grip angle sensor

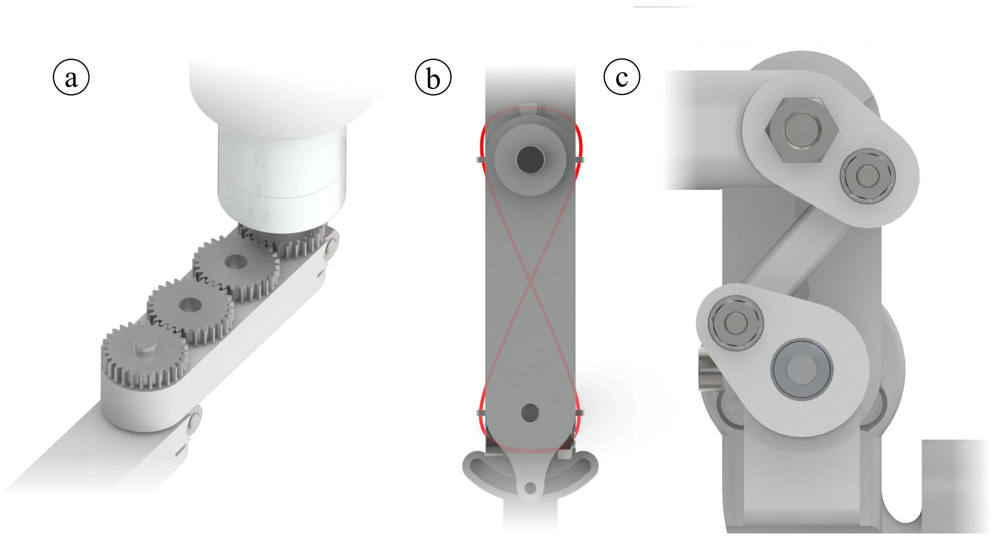

Figure 7.7: Different linkage designs for the mapping of the dependent joints; (a) gear-based design, (b) tendon-based design, and (c) currently implemented four-bar linkage design.

can be used instead of gearing. This can be implemented in arbitrary link lengths. Nevertheless, it still suffers from the hysteresis characteristics of the tendon, and the increased complexity of the assembly process. Finally, a four-bar mechanism was chosen for the proposed master manipulator because it does not suffer from the drawbacks of the former approaches. It further provides more rigidity with comparable size. Fig. 7.8 depicts the schematic of the mechanism. The primary link length l is fixed by the desired length of the manipulator's scaling factor, as previously described. In addition, two symmetric fixtures with length a are added to each side of the link with an angle θ. The second bar connects the fixtures diagonally via bearings. According to the geometry, this linkage produces a small angular deviation ϵ from an ideal dependent joint, where both joint angles are equal. This error is minimised by choosing θ to be as small as possible while taking into account the space required by the hinge joints. As presented in Fig. 7.8, for a given fixture length a an angle θ can be calculated which results into a maximal orientation error ϵ:

$$\epsilon(\theta) = \max_{q} \left\{ \mathrm{abs}(\tilde{q}(\theta, q) - q) \,|\, q \in [q^{\mathrm{min}}, q^{\mathrm{max}}] \right\} \tag{7.3}$$

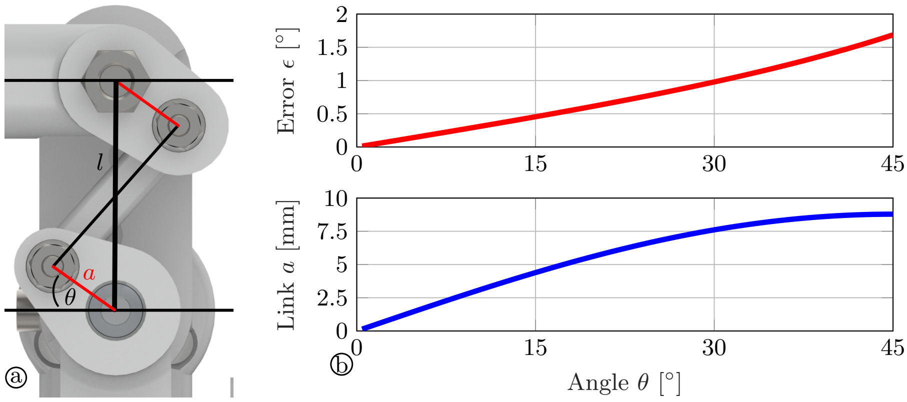

Figure 7.8: Parameter optimisation of the four bar mechanism. a.) parameter definition of the mechanism. b.) blue: relation between angle θ and link-length a, red: angular error ϵ as function of θ.

where q denotes the desired joint angle, $\tilde{q}$ is the resulting joint angle, and q^{min}, q^{max} are the ranges of joint motion.

Hence, the constrained optimisation problem can be formulated as:

$$\theta^{\star} = \arg\min\left(\epsilon\left(\theta\right)\right) \tag{7.4}$$

$$\text{subject to} \quad a \geq a_{\text{min}} \tag{7.5}$$

$$\text{and} \quad \theta = f^{-1}(a) \tag{7.6}$$

where a_{min} represents the mechanical constraints and f^{-1} is the function that relates the fixtures length to the angle θ. The optimal solution $\theta^{\star}$ was calculated as $\theta^{\star} = 35°$ resulting in maximal angular errors of $\epsilon = 1.2°$, for $l = 30\,\text{mm}$.

7.2.5 Workspace Analysis

The controlled surgical instruments have workspace limitations due to their geometry and their joint limits. It is important for the user to be able to percieve these limitations so that they can adapt their manipulation strategy accordingly, and retain an intuitive control of the instruments even at the edge of the workspace. These limitations can be conveyed implicitly to the user by providing them with an input device possessing similar properties. To compare the workspace of the slave and the master device, a workspace analysis was performed examining the dexterous workspace of their respective manipulators. A master device with a highly dexterous workspace may give the user the impression that certain instrument poses are feasible although they are not. Conversely, a master workspace with a small dexterous workspace may needlessly constrain the user's motions.

The dexterity measure $\mathcal{D}$ is calculated following the standard techniques of calculating the manipulability measure $\mathcal{M}$, introduced in [105]:

$$\mathcal{M} = \sqrt{|\mathbf{J}\,\mathbf{J}^T|}, \tag{7.7}$$

where $\mathbf{J}$ is the end effector Jacobian matrix. Since $\mathcal{M}$ does not consider mechanical constraints of the manipulator the dexterity measure is calculated as:

$$\mathcal{D} = \sqrt{|\mathbf{J}^q\,\mathbf{J}^{qT}|}, \tag{7.8}$$

where $\mathbf{J}^q$ is the joint-limit constrained end effector Jacobian. Using a constrained Jacobian to calculate the dexterity of a manipulator formalises the effects of the joint limits. Unlike in [106], the individual columns of $\mathbf{J}$ are penalised. When the i^{th} joint-value q_i approaches the limits $q_{i,\min}$ or $q_{i,\max}$ as:

$$\mathcal{P}_i^q = \frac{1 - \exp\left\{\frac{4\,\kappa_q\,(q_i - q_{i,\min})(q_{i,\max} - q_i)}{(q_{i,\max} - q_{i,\min})^2}\right\}}{1 - \exp\{\kappa_q\}}, \tag{7.9}$$

where the factor "4" and the denominator term "$1 - \exp\{\kappa_q\}$" in (7.9) are needed to normalise the penalisation term such that $\mathcal{P}_i^q$ spans the interval $[0, 1]$. At the joint-limits $\mathcal{P}_i^q$ evaluates to zero, and in the neutral position $\mathcal{P}_i^q$ evaluates to one. The scaling coefficient κ_q specifies the functional shape in between these points. The constrained Jacobian $\mathbf{J}^q$ is formed by penalising the columns $\mathbf{j}_i^q$ individually by

$$\mathbf{j}_i^q = \mathcal{P}_i^q\,\mathbf{j}_i^e, \tag{7.10}$$

where $\mathbf{j}_i^e$ is the i^{th} column of the end effector Jacobian. In contrast to the global penalisation presented in [106], this presented joint-wise penalisation is also suitable for redundant robots. The dexterity measure presented in [106] evaluates to zero when one joint reaches the limit, which is not appropriate for a redundant robot whose kinematics would not degenerate to an underconstrained system.

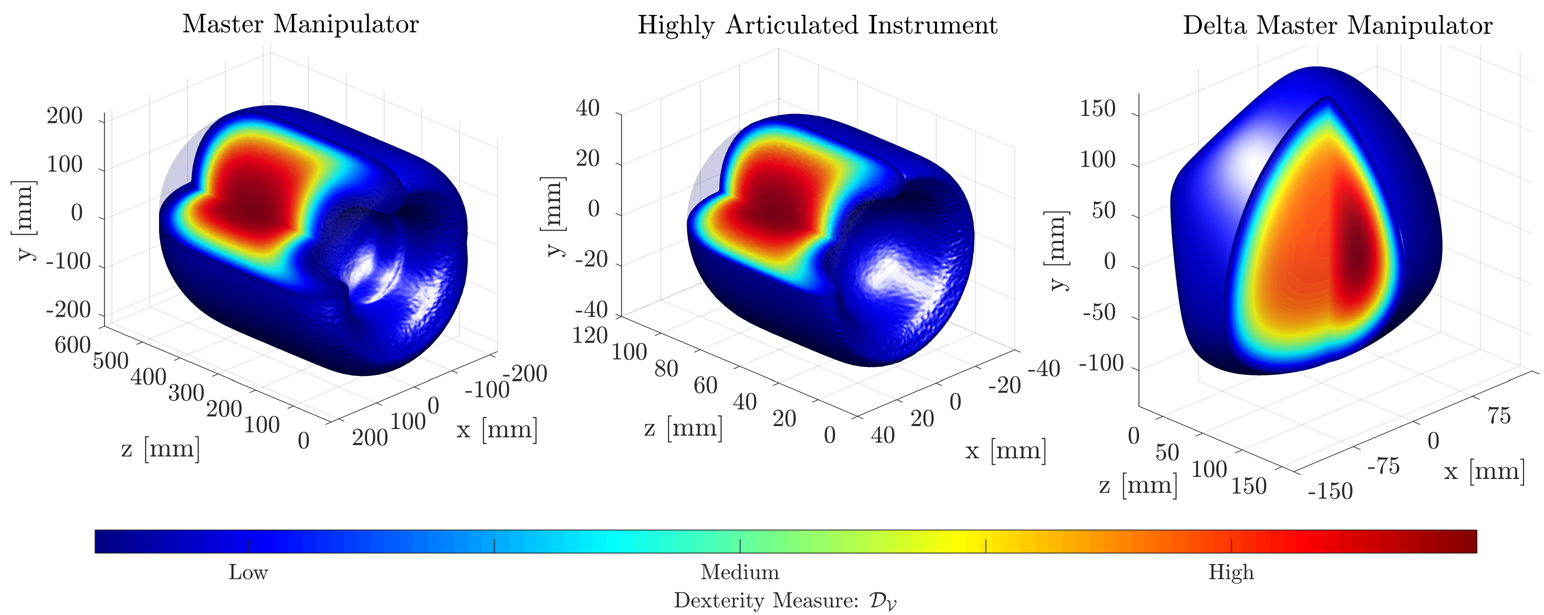

Figure 7.9: Dexterous workspace $\mathcal{D}_\mathcal{V}$ of the master manipulators and the highly articulated instrument.

Multiple configurations ($\mathbf{q}$) can map to the same end effector position ($\mathbf{x}$). The discretised workspace $\mathcal{V}$ which is comprised of voxels $v(i, j, k) \in \mathbb{R}^3$ and where i, j, k denote the indices of the voxels, is calculated as:

$$\mathcal{D}_{\mathcal{V}}(i, j, k) = \max_{\mathbf{q}_m} \{\mathcal{D}(\mathbf{q}_m) \mid \mathbf{x}(\mathbf{q}_m) \in v(i, j, k)\}. \tag{7.11}$$

A comparison of dexterous workspaces is depicted in Fig. 7.9. The computed dexterous workspaces illustrate the described dexterity measure $\mathcal{D}_{\mathcal{V}}$ of i.) the proposed master manipulator, ii.) the slave instruments manipulated by the master device, and iii.) the previously used master manipulator, the omega.7 delta robot. The visualisation illustrates that the omega.7 workspace shape is not suitable to manipulate the highly articulated tools designed for working in confined cylindrical shaped workspaces. In contrast, the dexterous workspace of the optimised master manipulator closely maps the workspace of the instruments.

7.3 Control System

All the rotational joints of the master manipulator are actuated by DC motors, which are driven by EPOS2 36/2 controllers (Maxon motor, Switzerland). The translation stage is actuated by a linear DC-Servomotor, which is driven by an MCLM 3006 controller (Faulhaber, Germany). All the motor controllers are connected to a host computer system via a CANopen communication interface. The motor controllers operate in torque control mode, which means the torque outputs of the motors are set by the software on the host computer. The control system in this software essentially calculates the appropriate torques to achieve four functionalities described in the following sections: joint limit (τ_L), viscous damping (τ_D), gravity compensation (τ_G), friction compensation (τ_F). The overall torque output to the i^{th} motor is a summation of those terms shown in equation 7.12. The joint values are being updated to the slave surgical system constantly while in operation. The overall diagram of the control system is shown in Fig. 7.10.

$$\tau_i = \tau_{L,i} + \tau_{D,i} + \tau_{G,i} + \tau_{F,i} \tag{7.12}$$

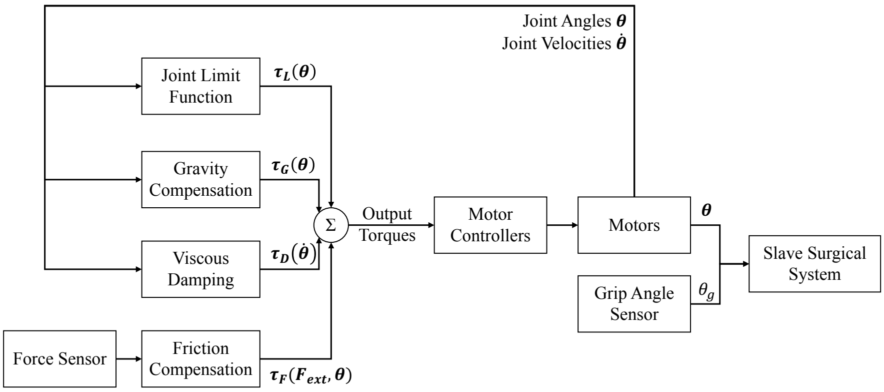

Figure 7.10: Diagram of the control system for the master manipulator. Four terms that contribute to the output torques; τ_L, τ_G, τ_D, τ_F; are calculated by the software on the host computer.

7.3.1 Joint Limit Force Rendering

To inform the user about when joint-limits are approached, a smooth haptic rendering profile is employed, rendering an increasing resistance the closer the user comes to the limits. Assuming symmetrical joint-limits of $\pm q_i^{\text{lim}}$, the motor torque for the i^{th} joint is calculated as:

$$q_i^{\text{lim},l} := q_i^{\text{lim}} - q_i^{\text{stiff}} \tag{7.13}$$

$$\tau_{L,i}(q_i) = \tau_{L,i,\max} \cdot \begin{cases} 0 & \text{, if } |q_i| < q_i^{\text{lim},l} \\ 1 & \text{, if } |q_i| > q_i^{\text{lim}} \\ \frac{1}{2} - \frac{1}{2}\cos\left(\pi \frac{(|q_i| - q_i^{\text{lim},l})}{q_i^{\text{stiff}}}\right) & \text{, else} \end{cases} \tag{7.14}$$

where $q_i^{\text{lim},l}$ is the lower limit from which the torque rendering ramps up. The stiffness is denoted as q_i^{stiff}, and $\tau_{L,i,\max}$ is the maximum torque rendered.

7.3.2 Gravity Compensation

The manipulator has a serial-link structure with integrated actuators and sensors in its joints. This results in a highly unbalanced and non-uniform variation in the weight perceived at the finger grip when it is manipulated throughout its workspace, which makes it unnatural to be manoeuvred. Additionally, the weight always pulls the device downward when the user releases the manipulator. The torque at each joint exerted due to gravity can be determined using the known mass parameters from the CAD design. The undesired weight can be compensated by providing the same amount of counter-torque at each joint. The parameters used for modelling the gravity torque include the mass and centre of mass of the links. The gravity torque is obtained by computing the inverse dynamics of the manipulator at zero velocity with acceleration equals to the gravity. A performance-optimised implementation of recursive Newton-Euler method by [107] is adopted to compute the inverse dynamics. Although the accuracy of the mass parameters calculated from the mechanical design are acceptable, the effect of the residual gravity force is further reduced by additional viscous damping:

$$\tau_{d,i} = -k\dot{q}_i \tag{7.15}$$

where k defines the damping coefficient, $\dot{q}_i$ denotes the joint velocity, and $\tau_{d,i}$ is the damping torque provided by the actuator. The damping can also reduce the abrupt motion by presenting additional friction to the user when the excessive manipulation speed is applied.

7.3.3 Friction Compensation

A significant obstacle to the use of serial-link master manipulators for joint-space control is the restrictions this approach imposes on the structure of the master device. This is particularly noticeable for devices with a high number of DoFs. In this chapter, the kinematic structure of the instruments imposes that the first two joints of the master manipulator be the translation and roll joints. However, the user only grasps the master manipulator at the end effector, on the very last joint.

The roll joint possesses a higher gear reduction (262:1, as opposed to 16:1 or 35:1 for the other joints), and far less cantilever advantage than any other rotational joints. In practice, and as shown in section 7.4.1, the materials used and friction present in the device mean that it is impossible for the user to rotate the roll joint without having to exert prohibitively high torques on the end effector. The translational joint encounters a similar problem as the translation forces are generated off-axis, thus creating torques hampering those same forces from translating the linear stage.

To address these issues, a 6-DoF force/torque sensor was incorporated in the last joint. The forces and torques detected by the sensor are transformed into the base joint's frame of reference following:

$$^{B}F_S = T_E \, {}^{E}T_S \, F_S, \tag{7.16}$$

$$^{B}Tq_S = T_E \, {}^{E}T_S \, Tq_S, \tag{7.17}$$

where F_S and Tq_S are the forces and torques read from the sensor, $^{B}F_S$ and $^{B}Tq_S$ are the forces and torques expressed in the base joint frame of reference, T_E is the homogeneous transform from the base joint to the end effector as obtained from the forward kinematics, and $^{E}T_S$ the static transformation from the end effector to the sensor frame of reference.

Torques detected by the sensor along the roll axis are then used to generate additional torques in the roll joint, using a proportional law with a dead band. Likewise, forces detected by the sensor along the translation axis are used to generate additional forces in the linear stage.

7.4 Experimental Results

7.4.1 Gravity and Friction Compensations

Evaluation of the gravity and friction compensation methods was carried out using the force/torque sensor integrated at the end effector. This sensor can directly measure the forces applied perceived by the user at the finger grips. Two short sequences of movements were performed by a user, each with one of two different control schemes applied to the manipulator. In one case no kind of compensation was used, and in the other both gravity and friction compensation were used. An excerpt of the experimental results are presented in Fig. 7.14 and Fig. 7.15. In the first case, where the gravity compensation and friction compensation methods are used, the maximum force and torque are 2.1 N and 42 Nmm with mean values of 0.9 N and 19 Nmm respectively. In contrast, without the compensations, the maximum force and torque exerted are 6.4 N and 151 Nmm with mean values of 3.1 N and 78 Nmm. This shows a significant amount of reduction in terms of the effort required by the user to move the manipulator. Furthermore, without the

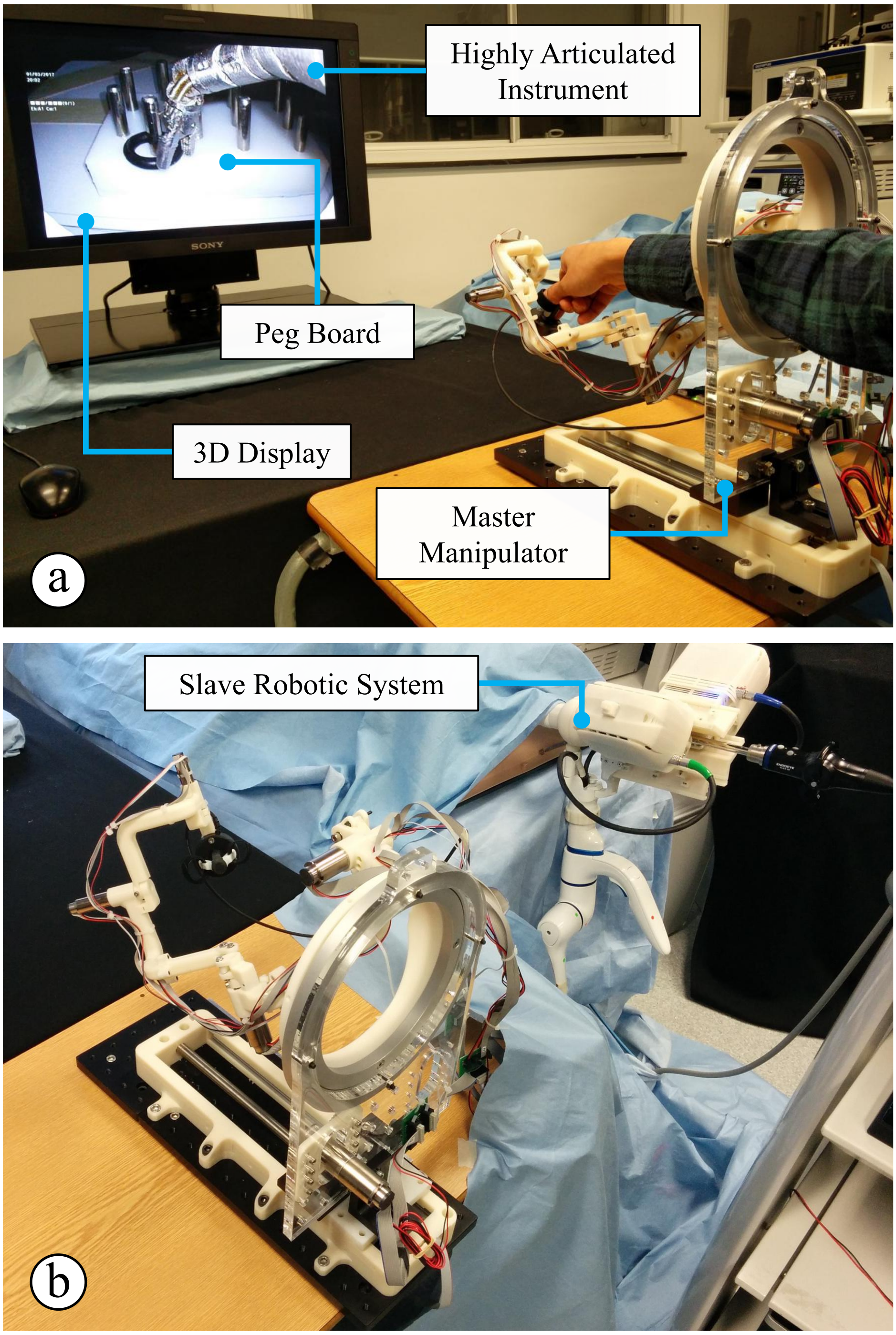

Figure 7.11: Experimental setup of the usability study, presenting (a) the operator manipulating the highly articulated instrument through the 3D display while performing the peg transfer task, and (b) the slave robotic system for single-access robotic surgery.

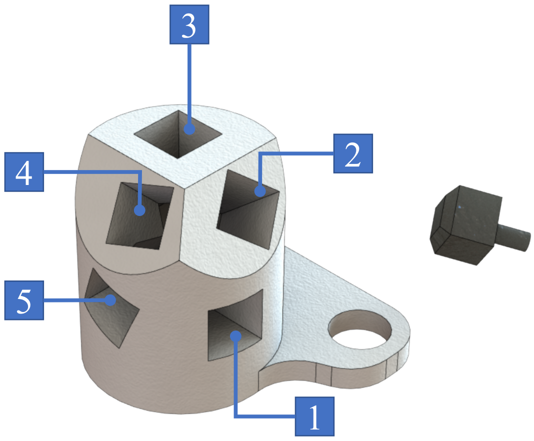

Figure 7.12: Structure and a peg for the insertion task, showing five different locations of the holes and the rubber peg.

friction compensation, the movements of the translation stage and the roll joint are very limited. A sequence of images in Fig. 7.13 demonstrate how the telemanipulation can be done with the device.

7.4.2 Usability Study

An experimental setup, presented in Fig. 7.11, was used to study the usability of the proposed manipulator in comparison with delta manipulators: omega.7 and sigma.7. Participants performed a single-handed peg insertion task into predefined holes in a fixed order using a structure and a peg shown in Fig. 7.12[†]. The task is to pick up a peg from a predefined starting position and fully insert it into a designated hole. The task starts from hole #1 and continues from there to the next hole in a sequential order until the last hole #5. All the participants had prior experience in using the Micro-IGES robotic surgical system with delta manipulators. The experiment was repeated twice for each user, and the time between each successful insertion was recorded. There are five participants in total, each performed the task using three different manipulators, and each task was repeated twice. This results in 150 trials of peg insertion task. Table 7.2,7.1 and Fig. 7.16 present the summary of the performance of the task.

[†]This structure was chosen in order to follow a similar experiment designed to test the usability of the *7-DoF surgical instrument for single access surgery*. Details of such experiment can be found in PhD thesis of *Carlo A. Seneci*

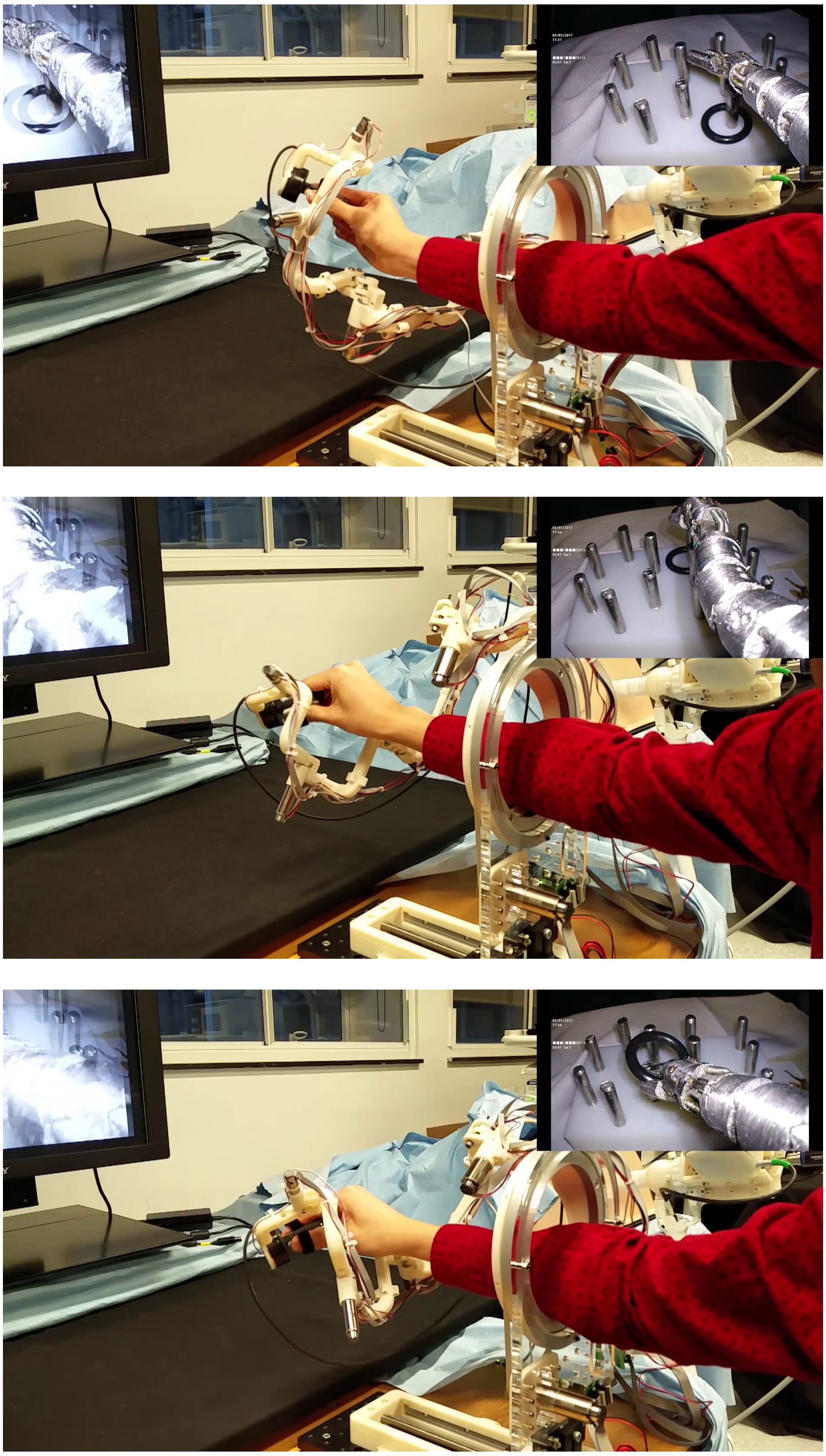

Figure 7.13: Telemanipulation of the highly articulated surgical instrument with the master manipulator. The top right corner of each image shows a view from the endoscope.

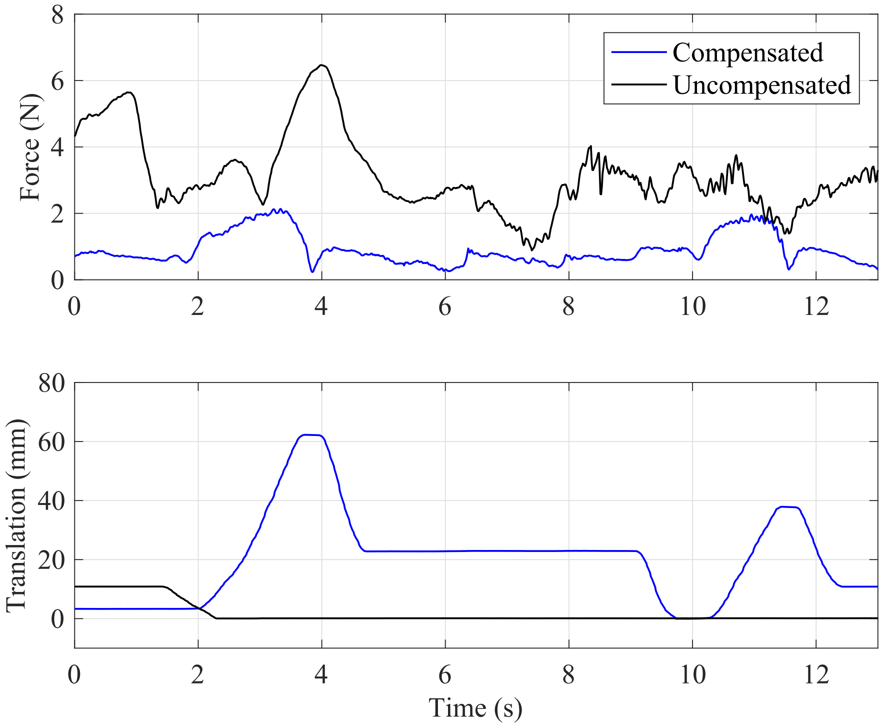

Figure 7.14: Comparison of manipulation force and the movement of the *translation* stage in implementations with and without the friction and gravity compensations. (see Fig. 7.2 for the reference of axis names)

	Master Manipulator	omega.7	sigma.7
Average Time	26.59	26.06	27.80
Standard Deviation	10.68	11.11	10.74
Median	24.78	23.09	28.34
Minimum	14.20	13.94	13.68
Maximum	50.11	51.69	43.26

Table 7.1: Task execution times (in second) between the master manipulators, with statistical values.

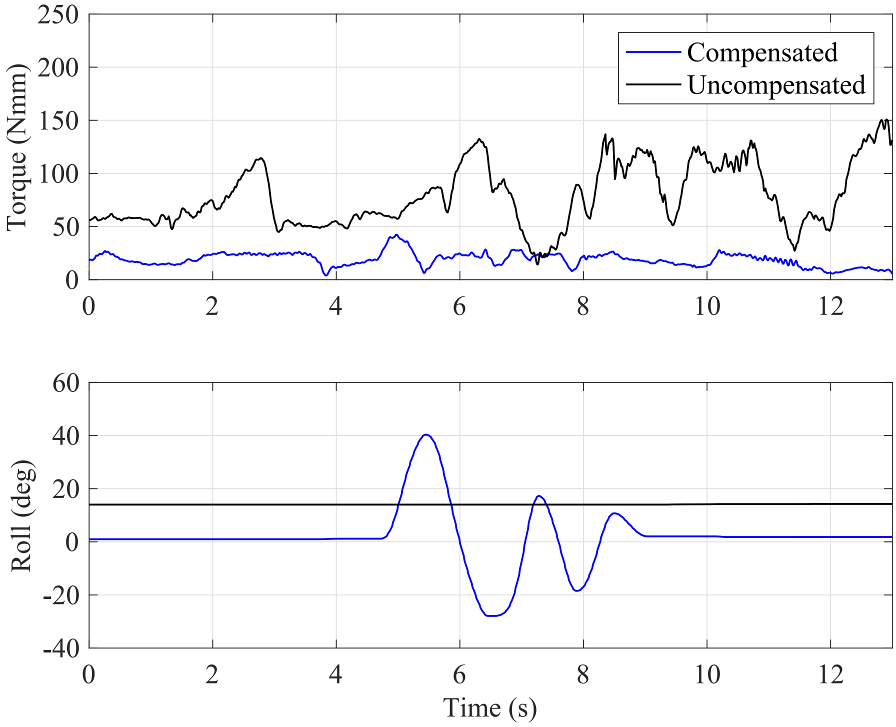

Figure 7.15: Comparison of manipulation torque and the movement of the *roll* joint in implementations with and without the friction and gravity compensations. (see Fig. 7.2 for the reference of axis names)

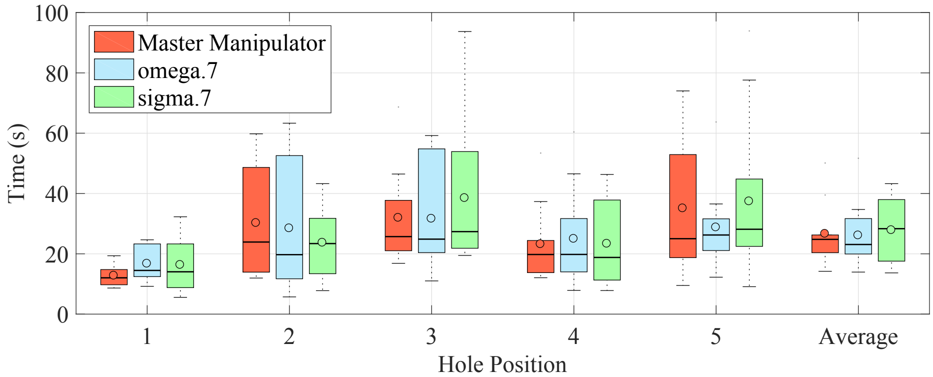

Figure 7.16: Task execution times between the master manipulators. The mean values are indicated by the circles.

	Master Manipulator	omega.7	sigma.7
Drops	1	3	2
Clutches	N/A	28	12

Table 7.2: Comparison of the number of times the peg was dropped or had to be placed down for repositioning, and the number of times the master devices had to be clutched.

7.4.3 Suturing Test

A preliminary suture was successfully carried out with the master manipulator. Because it was performed one hand, only one stitch was created without a knot tying. A sequence of images in Fig. 7.17 demonstrate how the stitch was done with the device.

7.5 Conclusion

This chapter presents a joint-space master manipulator device, designed for the control of highly articulated surgical instruments. The motivation for the development of this manipulator stemmed from the authors' past experience using task-space master manipulators with highly articulated surgical instruments. In particular, the need for clutching and lack of intuitive access to joint information proved to be two major drawbacks of these manipulators.

The presented system solves both of these issues. It operates via a different concept in terms of how a highly articulated surgical instrument can be telemanipulated with a kinematically identical manipulator via joint-space mapping as opposed to the conventional task-space mapping. The advantage of not having to rely on optimisation-based inverse kinematic approaches further increases the ease with which the system can be handled. The system can be safely driven to multiple joint limits, and still remain intuitively controlled as the limits are clearly marked using force feedback. A comparative study with conventional task-space master interfaces is conducted. It shows that the proposed master manipulator, while being a functional prototype with less stiffness and robustness, can perform equally well in the peg insertion task. The proposed manipulator does not

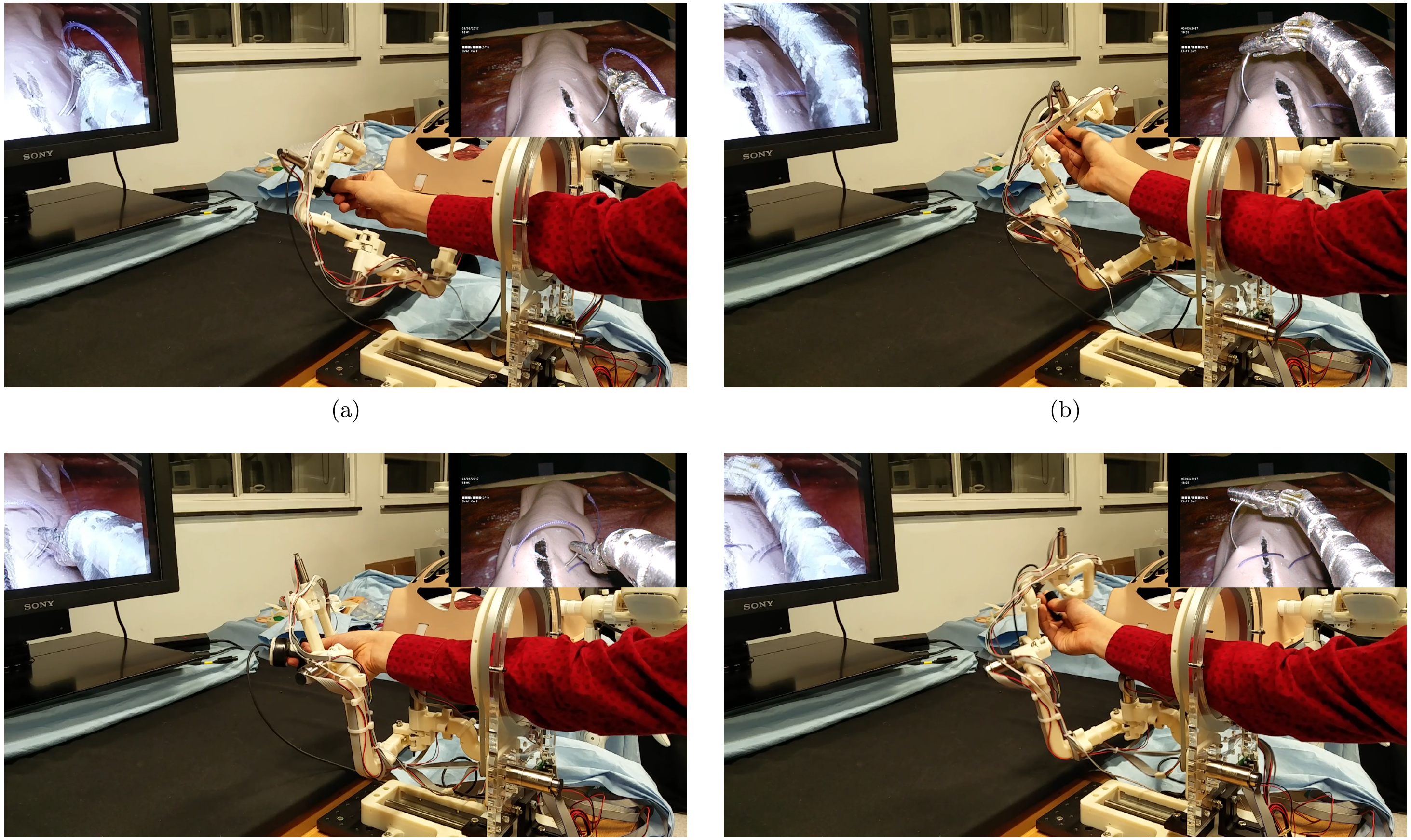

(a) (b) (c) (d)

Figure 7.17: One handed preliminary suture test. The top right corner of each image shows a view from the endoscope.

require clutching, also resulted in fewer peg drops. During the experiment, there is an observation that for some instances of peg drop, it occurred during clutching/un-clutching actions. Furthermore, a preliminary suture task was successfully performed, demonstrating the potential of using the master device to perform practical clinical tasks.

8 Conclusions and Future Research Directions

8.1 Contributions of this Thesis

This thesis explores the use of robotic manipulators to provide assistance in surgical applications, mainly in single-access surgery. Two articulated arms were developed specifically for the positioning of TEM surgical instruments, one of which has lightweight design with position- and force-sensing capabilities and another has cooperative control elements that assist surgeons in positioning surgical tools. The latter robot was also used for intraoperative biopsy applications. By integrating a probe-based confocal laser endomicroscopy system with the force-controlled robotic arm, a cooperative-controlled real-time optical biopsy system was realised. A low-cost technique to enable any robotic arms to sense a collision within health care environments was developed based on vibration signal processing. Lastly, a master interface designed specifically to control a TEM surgical instrument was developed. The development and evaluation of these devices led to a number of technical, clinical and scientific contributions:

1. The development of a lightweight, articulated surgical tool holder with an entirely passive mechanism. Its structural stiffness was characterised to ensure safety and suitability for clinical use. A comparative study against a conventional surgical clamp was carried out in a clinical investigation in humans, proving its practicality and demonstrating a more efficient surgical workflow for TEM.

2. The development of an articulated tool holder for minimally invasive surgery. It is a motorised device that supports a cooperative control scheme by allowing the user to directly move the surgical tool while being weight compensated. Its control system features a "hands-on"

reconfiguration that moves the joints in semi-null-space motion. A preliminary usability study was carried out comparing the passive tool holder. This device was able to perform quicker tasks with less effort spent.

3. The development of a collision detection system on a robotic manipulator. The system was able detect collisions with the environment in different locations with various directions. Four levels of material stiffness could be identified accurately and consistently. It is capable of performing "blind" environment mapping by solely relying on contact sensing.

4. The development of a robotic-assisted endomicroscopy system with an articulated robotic arm. The system demonstrated its capability to scan a moving *ex vivo* tissue surface with an arbitrary shape. The scanning system is both force adaptive and surface-normal adaptive, resulting in a contiguous large-area image mosaic with optimum quality.

5. The development of a joint-space master interface to telemanipulate a highly-articulated surgical instrument for single-access surgery. The device was able to render force feedback to the user. This allows rendering of the joint limits and speed limit, ensuring safe telemanipulation of the surgical tools. A comparative study with conventional task-space master interfaces was conducted. It is demonstrated that the joint-space interface can perform equally well in single hand pick-and-place tasks, without the need for a clutching mechanism.

8.2 Future Research Directions

Two key achievements presented in this thesis are the development of robotic manipulators for single-access surgery – the cooperative controlled surgical tool holder and a master manipulator for the teleoperation of the TEM surgical instrument. These devices are part of a surgical platform called "Micro-IGES robotic system" [13]. Looking at the kinematic configuration, a surgical tool is held by the grounded robotic arm that forms a chain of 13-DoF serial manipulator (7+6). In the current implementation, each device is independently manipulated. The master manipulator can only control the surgical instrument. To reposition the proximal device, the holding arm, an assistant is required to physically adjust the placement. The assistant, however, cannot move the surgical tool. This poses discoordination issues between the two devices. One potential solution is to allow the master manipulator to control the holder arm in task space while respecting the fulcrum point of the surgical port. This would also make use of the force-sensing capability of the arm to detect and prevent excessive external force, ensuring safety. Additionally, this approach can be used to tilt the camera view to the desired perspective manually by the surgeon him- or herself.

In Chapter 5, a blind approach of collision detection for a robotic arm using an accelerometer is presented. A possible improvement to the blind collision detection problem is to localise the impact within the link. Since the vibration signal is a wave that propagates through the link material, collisions at different locations make the signals arrive at the sensors on both sides at different times. We can possibly use the *Time Difference of Arrival (TDOA)* technique to implement the localisation [108].

The accuracy of the experimental results in terms of object identification proves that the accelerometer has very high potential to capture the difference in vibration patterns from a variety of materials. In this experiment, only four prototype materials have been used. This should be improved by adding more materials to prove this approach at the practical level.

The results from the preliminary work on the blind environment exploration method are promising. They demonstrates one possible application of using a simple accelerometer to implement a blind robot perception system. The current method is only limited to collecting point clouds of the environment as the impact direction estimation is not accurate. If this estimation could be improved, however, the normal vector of each point would be available. Therefore, instead of collecting points, planes would be collected. This could be merged into 3D mesh and provide more realistic reconstruction of the environment.

In Chapter 7, a joint-space master manipulator designed for the control of highly articulated surgical instruments is presented. The main challenge involved with this approach is to retain the ergonomics of an optimised task-space manipulator, such as an omega.7, while using a mechanical structure not optimised to that effect. The use of gravity compensation, and particularly force-torque compensation, has been instrumental in reaching this goal. However, several aspects present scope for further improvement. As the current device is at the prototype stage, a large number of components are 3D printed and lack stiffness. Combined with the fact that the model used for the gravity compensation was determined from theoretical values, the resulting gravity compensation, while sufficient, can still be improved. This could be accomplished with a mass parameters calibration method, such as [109]. A side effect of this imperfect compensation is to require the user to exert small forces to maintain the master manipulator in a given position. As a result, the force sensor may detect forces that do not really represent the user's intention to move and slightly distort the force-based motions in certain joint configurations. While non-critical, addressing these calibration and compensation issues will improve the usability of the system, further highlighting the advantages derived from this approach.

8.3 Conclusions

The research presented in this thesis proposes different types of robotic manipulators for enhancing surgical precision and patient outcomes in single-access surgery and, specifically, TEM.

An articulated robotic manipulator with passive joints was introduced, with built-in position and force sensors in each joint, and electronic joint brakes for instant lock/release capability. This addresses the difficulty in manipulation of heavy instruments in practical applications. Clinical trials demonstrated that this system is more precise, efficient, and intuitive than using conventional surgical clamps.

The articulated manipulator concept was further improved with motorised joints, evolving into an active tool holder. The joints allow the incorporation of advanced features such as ultra-lightweight gravity compensation and hands-on kinematic reconfiguration, which can optimise the placement of the tool holder in the operating theatre.

Due to the enhanced sensing capabilities, the application of the active robotic manipulator was further explored in conjunction with advanced image guidance approaches such as endomicroscopy. A combination of the fully cooperative robotic manipulator with a high-speed scanning endomicroscopy instrument was presented, simplifying the incorporation of optical biopsy techniques in routine surgical workflows.

One key aspect of any robotic manipulator working in the operating room is the safety of its operation. A technique enabling robotic manipulators to reliably detect collisions and characterise materials was introduced. The method was also extended to an environment mapping scenario where the manipulator can learn and build a map of its surroundings.

A final embodiment of a cooperative robotic manipulator was presented as an input interface to control an articulated surgical instrument. This master interface addresses the drawbacks of traditional master-slave devices, e.g., the clutching mechanism, the mismatch between master-slave workspaces, and the lack of intuitive feedback. The presented joint-space robotic manipulator emulates the kinematic structure of the surgical instrument, allowing it to be safely driven to multiple joint limits while retaining an intuitive control behaviour. A preliminary comparative study with conventional task-space master interfaces showed that the proposed device can perform equally well in standard minimally invasive surgery (MIS) peg transfer tasks.

Bibliography

[Citing pages are listed after each reference.]

[1] Y. Kobayashi, Y. Sekiguchi, T. Noguchi, Y. Takahashi, Q. Liu, S. Oguri, K. Toyoda, M. Uemura, S. Ieiri, M. Tomikawa, T. Ohdaira, M. Hashizume, and M. G. Fujie, "Development of a robotic system with six-degrees-of-freedom robotic tool manipulators for single-port surgery," *The International Journal of Medical Robotics and Computer Assisted Surgery (IJMRCAS)*, vol. 11, no. 2, pp. 235–246, 2015. [Pages 13, 33, and 35.]

[2] M. Arnold, M. S. Sierra, M. Laversanne, I. Soerjomataram, A. Jemal, and F. Bray, "Global patterns and trends in colorectal cancer incidence and mortality," *Gut*, vol. 66, no. 4, pp. 683–691, 2017. [Page 21.]

[3] V. Vitiello, Su-Lin Lee, T. P. Cundy, and G.-Z. Yang, "Emerging Robotic Platforms for Minimally Invasive Surgery," *IEEE Reviews in Biomedical Engineering*, vol. 6, no. 1, pp. 111–126, 2013. [Pages 21 and 35.]

[4] C. Bergeles and G.-Z. Yang, "From Passive Tool Holders to Microsurgeons: Safer, Smaller, Smarter Surgical Robots," *IEEE Transactions on Biomedical Engineering (TBME)*, vol. 61, no. 5, pp. 1565–1576, 2014. [Page 21.]

[5] M. E. Hagen, J. J. Meehan, I. Inan, and P. Morel, "Visual clues act as a substitute for haptic feedback in robotic surgery." *Surgical Endoscopy*, vol. 22, no. 6, pp. 1505–8, 2008. [Page 22.]

[6] C.-H. King, M. O. Culjat, M. L. Franco, J. W. Bisley, G. P. Carman, E. P. Dutson, and W. S. Grundfest, "A Multielement Tactile Feedback System for Robot-Assisted Minimally Invasive Surgery," *IEEE Transactions on Haptics*, vol. 2, no. 1, pp. 52–56, 2009. [Pages 22 and 41.]

[7] L. Santos-Carreras, R. Beira, A. Sengül, R. Gassert, and H. Bleuler, "Influence of force and torque feedback on operator performance in a VR-based suturing task," *Applied Bionics and Biomechanics*, vol. 7, no. 3, 2010. [Page 22.]

[8] W. Semere, M. Kitagawa, and A. Okamura, "Teleoperation with sensor/actuator asymmetry: task performance with partial force feedback," in *International Symposium on Haptic Interfaces for Virtual Environment and Teleoperator Systems (HAPTICS)*, Chicago, IL, 2004, pp. 121–127. [Page 22.]

[9] C. R. Wagner, N. Stylopoulos, P. G. Jackson, and R. D. Howe, "The Benefit of Force Feedback in Surgery : Examination of Blunt Dissection," *Presence: teleoperators and virtual environments*, vol. 16, no. 3, pp. 252–262, 2007. [Page 22.]

[10] E. Samur, S.-C. L., A. Sengul, G. Rognini, S. Marchesotti, and H. Bleuler, "Role of haptics in surgical robotics: report on a workshop." *Editorial News of IEEE Transactions on Haptics*, 2011. [Page 22.]

[11] L. Morelli, S. Guadagni, G. Di Franco, M. Palmeri, G. Di Candio, and F. Mosca, "Da Vinci single site© surgical platform in clinical practice: a systematic review," *The International Journal of Medical Robotics and Computer Assisted Surgery (IJMRCAS)*, vol. 12, no. 4, pp. 724–734, 2016. [Pages 22 and 31.]

[12] J. H. Kaouk, G. P. Haber, R. Autorino, S. Crouzet, A. Ouzzane, V. Flamand, and A. Villers, "A novel robotic system for single-port urologic surgery: First clinical investigation," *European Urology*, vol. 66, no. 6, pp. 1033–1043, 2014. [Pages 22 and 31.]

[13] J. Shang, K. Leibrandt, P. Giataganas, V. Vitiello, C. A. Seneci, P. Wisanuvej, J. Liu, G. Gras, J. Clark, A. Darzi, and G.-Z. Yang, "A Single-Port Robotic System for Transanal Microsurgery—Design and Validation," *IEEE Robotics and Automation Letters (RA-L)*, vol. 2, no. 3, pp. 1510–1517, 2017. [Pages 22, 42, 124, and 147.]

[14] G.-Z. Yang, P. Wisanuvej, K. Leibrandt, C. A. Seneci, J. Shang, and J. Liu, "Surgical instrument, robotic arm and control system for a

robotic arm," International Patent WO2 017 203 231A1, November 30, 2017. [Page 22.]

[15] G.-Z. Yang, C. A. Seneci, and J. Shang, "Surgical instrument," UK Patent GB2 550 575A, November 29, 2017. [Pages 22 and 124.]

[16] C. A. Seneci, G. Gras, P. Wisanuvej, J. Shang, and G.-Z. Yang, "3D Printing of Improved Needle Grasping Instrument for Flexible Robotic Surgery," in *IEEE/RSJ International Conference on Intelligent Robots and Systems (IROS)*, Vancouver, 2017, pp. 2524–2530. [Page 22.]

[17] G.-Z. Yang, P. Wisanuvej, C. Seneci, and K. Leibrandt, "Control system," UK Patent GB2 550 577A, November 29, 2017. [Page 22.]

[18] K. Leibrandt, P. Wisanuvej, G. Gras, J. Shang, C. A. Seneci, P. Giataganas, V. Vitiello, A. Darzi, and G.-Z. Yang, "Effective Manipulation in Confined Spaces of Highly Articulated Robotic Instruments for Single Access Surgery," *IEEE Robotics and Automation Letters (RA-L)*, vol. 2, no. 3, pp. 1704–1711, 2017. [Pages 22, 42, and 124.]

[19] J. Liu, N. Penney, P. Wisanuvej, A. Darzi, and G.-Z. Yang, "A Case Study of a Passive Robotic Arm for Conventional Transanal Microsurgery," in *Hamlyn Symposium on Medical Robotics*, London, 2017. [Page 22.]

[20] G.-Z. Yang, J. Liu, and P. Wisanuvej, "Safety Device," UK Patent GB2 554 846A, April 18, 2018. [Page 22.]

[21] G.-Z. Yang and J. Liu, "Absolute rotary encoder," International Patent WO2 016 083 825A1, June 2, 2016. [Pages 22 and 50.]

[22] K. S. Roh, S. Yoon, Y. Do Kwon, Y. Shim, and Y.-J. Kim, "Single-Port Surgical Robot System with Flexible Surgical Instruments," in *International Conference on Intelligent Robotics and Applications (ICIRA)*, Portsmouth, 2015, pp. 447–459. [Page 31.]

[23] A. Bajo, R. E. Goldman, L. Wang, D. Fowler, and N. Simaan, "Integration and preliminary evaluation of an Insertable Robotic Effectors

Platform for Single Port Access Surgery," in *IEEE International Conference on Robotics and Automation (ICRA)*, St Paul, MN, 2012, pp. 3381–3387. [Page 31.]

[24] G. P. Haber, R. Autorino, H. Laydner, B. Yang, M. A. White, S. Hillyer, F. Altunrende, R. Khanna, G. Spana, I. Wahib, K. Fareed, R. J. Stein, and J. H. Kaouk, "SPIDER surgical system for urologic procedures with laparoendoscopic single-site surgery: From initial laboratory experience to first clinical application," *European Urology*, vol. 61, no. 2, pp. 415–422, 2012. [Page 31.]

[25] D. Giannotti, G. Casella, G. Patrizi, G. Di Rocco, L. Castagneto-Gissey, A. Metere, M. G. Bernieri, A. R. Vestri, and A. Redler, "Spider surgical system versus multiport laparoscopic surgery: performance comparison on a surgical simulator," *BMC Surgery*, vol. 15, no. 1, p. 54, 2015. [Page 33.]

[26] J. Shang, C. J. Payne, J. Clark, D. P. Noonan, K.-W. Kwok, A. Darzi, and G.-Z. Yang, "Design of a multitasking robotic platform with flexible arms and articulated head for Minimally Invasive Surgery," in *IEEE/RSJ International Conference on Intelligent Robots and Systems (IROS)*, Vilamoura, 2012, pp. 1988–1993. [Page 33.]

[27] M. Hvilshøj, S. Bøgh, O. Skov Nielsen, and O. Madsen, "Autonomous industrial mobile manipulation (AIMM): past, present and future," *Industrial Robot: An International Journal*, vol. 39, no. 2, pp. 120–135, 2012. [Page 36.]

[28] N. Lauzier, S. Lefrançois, D. Castonguay, L.-A. Allen Demers, J.-F. Duval, Y. Drolet Mihelic, P. O. Proulx, R. Bekhti, P. Cardou, V. Duchaine, S. Bouchard, and J.-P. Jobin, "Force/torque sensor, apparatus and method for robot teaching and operation," US Patent 20 150 323 398, November 12, 2015. [Page 36.]

[29] R. Taylor, P. Jensen, L. Whitcomb, A. Barnes, R. Kumar, D. Stoianovici, P. Gupta, Z. Wang, E. Dejuan, and L. Kavoussi, "A steady-hand robotic system for microsurgical augmentation," *The International Journal of Robotics Research (IJRR)*, vol. 18, no. 12, pp. 1201–1210, 1999. [Page 36.]

[30] B. Mitchell, J. Koo, I. Iordachita, P. Kazanzides, A. Kapoor, J. Handa, G. Hager, and R. Taylor, "Development and application of a new steady-hand manipulator for retinal surgery," in *IEEE International Conference on Robotics and Automation (ICRA)*, Rome, 2007, pp. 623–629. [Page 36.]

[31] A. Uneri, M. A. Balicki, J. Handa, P. Gehlbach, R. H. Taylor, and I. Iordachita, "New steady-hand Eye Robot with micro-force sensing for vitreoretinal surgery," in *IEEE RAS & EMBS International Conference on Biomedical Robotics and Biomechatronics (BioRob)*, Tokyo, 2010, pp. 814–819. [Page 36.]

[32] W. L. Bargar, A. Bauer, and M. Börner, "Primary and Revision Total Hip Replacement Using the Robodoc(R) System," *Clinical Orthopaedics & Related Research*, vol. 354, pp. 82–91, 1998. [Page 36.]

[33] B. Davies, M. Jakopec, S. J. Harris, F. Rodriguez y Baena, A. Barrett, A. Evangelidis, P. Gomes, J. Henckel, and J. Cobb, "Active-Constraint Robotics for Surgery," *Proceedings of the IEEE*, vol. 94, no. 9, pp. 1696–1703, 2006. [Page 36.]

[34] G. Xu, A. Song, and H. Li, "Control system design for an upper-limb rehabilitation robot," *Advanced Robotics*, vol. 25, no. 1-2, pp. 229–251, 2011. [Pages 36 and 59.]

[35] R. Konietschke, U. Hagn, M. Nickl, S. Jörg, A. Tobergte, G. Passig, U. Seibold, L. Le Tien, B. Kübler, M. Gröger, and Others, "The DLR MiroSurge-A robotic system for surgery." in *IEEE International Conference on Robotics and Automation (ICRA)*, vol. 9, Kobe, 2009, pp. 1589–1590. [Page 36.]

[36] O. Brock, O. Khatib, and S. Viji, "Task-consistent obstacle avoidance and motion behavior for mobile manipulation," in *IEEE International Conference on Robotics and Automation (ICRA)*, vol. 1, Washington DC, 2002, pp. 388–393. [Page 36.]

[37] M. Duguleana, F. G. Barbuceanu, A. Teirelbar, and G. Mogan, "Obstacle avoidance of redundant manipulators using neural networks based reinforcement learning," *Robotics and Computer-Integrated Manufacturing*, vol. 28, no. 2, pp. 132–146, 2012. [Page 36.]

[38] Y. Li and Y. Liu, "A new task-consistent overturn prevention algorithm for redundant mobile modular manipulators," in *IEEE/RSJ International Conference on Intelligent Robots and Systems (IROS)*, Edmonton, 2005, pp. 418–423. [Page 36.]

[39] J. D. English, A. Maciejewski, and Others, "Fault tolerance for kinematically redundant manipulators: anticipating free-swinging joint failures," *IEEE Transactions on Robotics and Automation*, vol. 14, no. 4, pp. 566–575, 1998. [Page 36.]

[40] A. D. Luca and R. Mattone, "Sensorless Robot Collision Detection and Hybrid Force / Motion Control," in *IEEE International Conference on Robotics and Automation (ICRA)*, Barcelona, 2005, pp. 999–1004. [Page 37.]

[41] A. Luca, A. Albu-Schaffer, S. Haddadin, and G. Hirzinger, "Collision Detection and Safe Reaction with the DLR-III Lightweight Manipulator Arm," in *IEEE/RSJ International Conference on Intelligent Robots and Systems (IROS)*, Beijing, 2006, pp. 1623–1630. [Page 37.]

[42] S. Haddadin, A. Albu-Schaffer, A. De Luca, and G. Hirzinger, "Collision detection and reaction: A contribution to safe physical human-robot interaction," in *IEEE/RSJ International Conference on Intelligent Robots and Systems (IROS)*, Nice, 2008, pp. 22–26. [Page 37.]

[43] H.-W. Je, J.-Y. Baek, and M. C. Lee, "Current based compliance control method for minimizing an impact force at collision of service robot arm," *International Journal of Precision Engineering and Manufacturing*, vol. 12, no. 2, pp. 251–258, 2011. [Page 37.]

[44] T. Meriçli, Ç. Meriçli, and H. Akın, "A robust statistical collision detection framework for quadruped robots," *RoboCup 2008: Robot Soccer World Cup XII*, 2009. [Page 38.]

[45] R. H. Lamotte, "Softness Discrimination With a Tool," *Journal of Neurophysiology*, vol. 83, no. 4, pp. 1777–1786, 2013. [Page 38.]

[46] K. Kuchenbecker, J. Fiene, and G. Niemeyer, "Event-Based Haptics and Acceleration Matching: Portraying and Assessing the Realism of Contact," in *First Joint Eurohaptics Conference and Symposium on*

Haptic Interfaces for Virtual Environment and Teleoperator Systems, Pisa, 2005, pp. 381–387. [Page 38.]

[47] J. Romano and K. Kuchenbecker, "Creating realistic virtual textures from contact acceleration data," *IEEE Transactions on Haptics*, vol. 5, no. 2, pp. 109–119, 2012. [Page 38.]

[48] J. Windau, "An Inertia-Based Surface Identification System," in *IEEE International Conference on Robotics and Automation (ICRA)*, Anchorage, AK, 2010, pp. 2330–2335. [Page 38.]

[49] H. Liu, X. Song, and T. Nanayakkara, "Friction estimation based object surface classification for intelligent manipulation," in *IEEE International Conference on Robotics and Automation (ICRA): Workshop on Autonomous Grasping*, Shanghai, 2011. [Page 38.]

[50] D. Vail and M. Veloso, "Learning from Accelerometer Data on a Legged Robot," in *IFAC/EURON Symposium on Intelligent Autonomous Vehicles*, Lisbon, 2004. [Pages 38 and 91.]

[51] E. Torres-Jara, L. Natale, and P. Fitzpatrick, "Tapping into Touch," in *Fifth International Workshop on Epigenetic Robotics: Modeling Cognitive Development in Robotic Systems*, Nara, 2005, pp. 79–86. [Page 38.]

[52] J. Richmond and D. Pai, "Active Measurement of Contact Sounds," in *IEEE International Conference on Robotics and Automation (ICRA)*, vol. 3, San Francisco, CA, 2000, pp. 2146–2152. [Page 38.]

[53] S. Femmam, "Perception and characterization of materials using signal processing techniques," *IEEE Transactions on Instrumentation and Measurement*, vol. 50, no. 5, pp. 1203–1211, 2001. [Page 38.]

[54] M. Campos, R. Bajcsy, and V. Kumar, "Exploratory procedures for material properties: The temperature perception," in *International Conference on Advanced Robotics: Robots in Unstructured Environments (ICAR)*, Pisa, 1991. [Page 38.]

[55] G. Paul, D. K. Liu, N. Kirchner, and S. Webb, "Safe and Efficient Autonomous Exploration Technique for 3D Mapping of a Complex

Bridge Maintenance Environment," in *International Symposium on Automation and Robotics in Construction (ISARC)*, Madras, 2007. [Page 38.]

[56] T. Kunz, U. Reiser, M. Stilman, and A. Verl, "Real-time path planning for a robot arm in changing environments," in *IEEE/RSJ International Conference on Intelligent Robots and Systems (IROS)*, Taipei, 2010, pp. 5906–5911. [Page 38.]

[57] P. Allen and P. Michelman, "Acquisition and interpretation of 3-D sensor data from touch," *IEEE Transactions on Robotics and Automation*, vol. 6, no. 4, pp. 397–404, 1990. [Page 38.]

[58] A. M. Okamura, "Feature Detection for Haptic Exploration with Robotic Fingers," *The International Journal of Robotics Research (IJRR)*, vol. 20, no. 12, pp. 925–938, 2001. [Page 38.]

[59] J. M. Jabbour, M. A. Saldua, J. N. Bixler, and K. C. Maitland, "Confocal endomicroscopy: Instrumentation and medical applications," *Annals of Biomedical Engineering*, vol. 40, no. 2, pp. 378–397, 2012. [Page 39.]

[60] T. Ohigashi, N. Kozakai, R. Mizuno, A. Miyajima, and M. Murai, "Endocytoscopy: novel endoscopic imaging technology for in-situ observation of bladder cancer cells." *Journal of Endourology / Endourological Society*, vol. 20, no. 9, pp. 698–701, 2006. [Page 39.]

[61] A. Patsias, L. Giraldez-Rodriguez, A. Polydorides, R. Richards-Kortum, S. Anandasabapathy, T. Quang, A. Sikora, and B. Miles, "Feasibility of Transoral Robotic-Assisted High Resolution Microendoscopic Imaging of Oropharyngeal Squamous Cell Carcinoma." *Head & neck*, 2014. [Page 39.]

[62] T. Vercauteren, A. Perchant, G. Malandain, X. Pennec, and N. Ayache, "Robust mosaicing with correction of motion distortions and tissue deformations for in vivo fibered microscopy," *Medical Image Analysis*, vol. 10, no. 5, pp. 673–692, 2006. [Page 39.]

[63] M. Hughes and G.-Z. Yang, "Robotics and smart instruments for translating endomicroscopy to in situ, in vivo applications," *Com-*

puterized Medical Imaging and Graphics, vol. 36, pp. 589–590, 2012. [Page 39.]

[64] W. T. Latt, R. C. Newton, M. Visentini-Scarzanella, C. J. Payne, D. P. Noonan, J. Shang, and G. Z. Yang, "A hand-held instrument to maintain steady tissue contact during probe-based confocal laser endomicroscopy," *IEEE Transactions on Biomedical Engineering (TBME)*, vol. 58, no. 9, pp. 2694–2703, 2011. [Page 40.]

[65] W. T. Latt, T. P. Chang, A. Di Marco, P. Pratt, K.-W. Kwok, J. Clark, and G.-Z. Yang, "A hand-held instrument for in vivo probe-based confocal laser endomicroscopy during Minimally Invasive Surgery," in *IEEE/RSJ International Conference on Intelligent Robots and Systems (IROS)*, Vilamoura, 2012, pp. 1982–1987. [Page 40.]

[66] P. Giataganas, V. Vitiello, V. Simaiaki, E. Lopez, and G. Z. Yang, "Cooperative in situ microscopic scanning and simultaneous tissue surface reconstruction using a compliant robotic manipulator," in *IEEE International Conference on Robotics and Automation (ICRA)*, vol. 1, Karlsruhe, 2013, pp. 5378–5383. [Page 40.]

[67] P. Giataganas, M. Hughes, and G. Z. Yang, "Force adaptive robotically assisted endomicroscopy for intraoperative tumour identification," *International Journal of Computer Assisted Radiology and Surgery*, vol. 10, no. 6, pp. 825–832, 2015. [Page 40.]

[68] S. Zuo, M. Hughes, and G. Z. Yang, "Novel Balloon Surface Scanning Device for Intraoperative Breast Endomicroscopy," *Annals of Biomedical Engineering*, vol. 44, no. 7, pp. 2313–2326, 2015. [Page 40.]

[69] M. S. Erden, B. Rosa, N. Boularot, B. Gayet, G. Morel, and J. Szewczyk, "Conic-spiraleur: A miniature distal scanner for confocal microlaparoscope," *IEEE/ASME Transactions on Mechatronics*, vol. 19, no. 6, pp. 1786–1798, 2014. [Page 40.]

[70] B. Rosa, M. S. Erden, T. Vercauteren, B. Herman, J. Szewczyk, and G. Morel, "Building large mosaics of confocal edomicroscopic images using visual servoing." *IEEE Transactions on Biomedical Engineering (TBME)*, vol. 60, no. 4, pp. 1041–9, 2013. [Page 40.]

[71] U. Hagn, R. Konietschke, A. Tobergte, M. Nickl, S. Jörg, B. Kübler, G. Passig, M. Gröger, F. Fröhlich, U. Seibold, L. Le-Tien, A. Albu-Schäffer, A. Nothhelfer, F. Hacker, M. Grebenstein, and G. Hirzinger, "DLR MiroSurge: a versatile system for research in endoscopic telesurgery." *International Journal of Computer Assisted Radiology and Surgery (IJCARS)*, vol. 5, no. 2, pp. 183–93, 2010. [Page 41.]

[72] A. Tobergte, G. Passig, B. Kübler, U. Seibold, U. A. Hagn, F. A. Fröhlich, R. Konietschke, S. Jörg, M. Nickl, S. Thielmann, and Others, "Mirosurge-advanced user interaction modalities in minimally invasive robotic surgery," *Presence: Teleoperators and Virtual Environments*, vol. 19, no. 5, pp. 400–414, 2010. [Page 41.]

[73] W. McMahan, J. Gewirtz, D. Standish, P. Martin, J. A. Kunkel, M. Lilavois, A. Wedmid, D. I. Lee, and K. J. Kuchenbecker, "Tool Contact Acceleration Feedback for Telerobotic Surgery," *IEEE Transactions on Haptics*, vol. 4, no. 3, pp. 210–220, 2011. [Page 41.]

[74] M. Kitagawa, D. Dokko, A. M. Okamura, and D. D. Yuh, "Effect of sensory substitution on suture-manipulation forces for robotic surgical systems." *The Journal of Thoracic and Cardiovascular Surgery*, vol. 129, no. 1, pp. 151–8, 2005. [Page 41.]

[75] S. Matich, C. Neupert, A. Kirschniak, H. F. Schlaak, and P. P. Pott, "A new single-port robotic system based on a parallel kinematic structure," in *2015 IEEE/RSJ International Conference on Intelligent Robots and Systems (IROS)*, Hamburg, 2015, pp. 236–241. [Page 42.]

[76] S. J. Phee, S. C. Low, V. A. Huynh, A. P. Kencana, Z. L. Sun, and K. Yang, "Master and slave transluminal endoscopic robot (MASTER) for natural orifice transluminal endoscopic surgery (NOTES)," in *Annual International Conference of the IEEE Engineering in Medicine and Biology Society (EMBC)*, Minneapolis, MN, 2009, pp. 1192–1195. [Page 43.]

[77] S. Shim, T. Kang, D. Ji, H. Choi, S. Joung, and J. Hong, "An all-joint-control master device for single-port laparoscopic surgery robots," *International Journal of Computer Assisted Radiology and Surgery (IJCARS)*, vol. 11, no. 8, pp. 1547–1557, 2016. [Page 43.]

[78] C. Neupert, S. Matich, N. Scherping, M. Kupnik, R. Werthschutzky, and C. Hatzfeld, "Pseudo-Haptic Feedback in Teleoperation," *IEEE Transactions on Haptics*, vol. 9, no. 3, pp. 397–408, 2016. [Page 43.]

[79] Z. M. Thant, S. C. Low, S. W. Tang, L. Phee, K. Y. Ho, and S. C. Chung, "Ergonomic master controller for flexible endoscopic gastrointestinal robot manipulator," in *International Conference on Biomedical and Pharmaceutical Engineering (ICBPE)*, Singapore, 2006, pp. 575–579. [Page 43.]

[80] H. Kunitake and M. a. Abbas, "Transanal endoscopic microsurgery for rectal tumors: a review." *The Permanente Journal*, vol. 16, no. 2, pp. 45–50, 2012. [Page 46.]

[81] Y. Qi, D. Stoddard, and J. R. T. Monson, "Indications and techniques of transanal endoscopic microsurgery (TEMS)." *Journal of Gastrointestinal Surgery*, vol. 15, no. 8, pp. 1306–8, 2011. [Page 46.]

[82] A. Morita, Y. Okada, M. Kitano, T. Hori, M. Taneda, T. Kirino, C. Y. Liu, and P. Cappabianca, "Development of hybrid integrated endoscope-holder system for endoscopic microneurosurgery," *Neurosurgery*, vol. 55, no. 4, pp. 926–932, 2004. [Page 46.]

[83] Hongwei Zhang, S. Ahmad, and G. Liu, "Torque estimation technique of robotic joint with harmonic drive transmission," in *IEEE International Conference on Robotics and Automation (ICRA)*, Karlsruhe, 2013, pp. 3034–3039. [Page 50.]

[84] T. Kröger, "Opening the door to new sensor-based robot applications—The Reflexxes Motion Libraries," in *IEEE International Conference on Robotics and Automation (ICRA)*, Shanghai, 2011, pp. 1–4. [Pages 61, 106, and 107.]

[85] H. Olsson, K. Åström, C. Canudas de Wit, M. Gäfvert, and P. Lischinsky, "Friction Models and Friction Compensation," *European Journal of Control*, vol. 4, no. 3, pp. 176–195, 1998. [Page 64.]

[86] B. Siciliano, L. Sciavicco, L. Villani, and G. Oriolo, *Robotics: Modelling, Planning and Control*. Springer, 2009. [Pages 66 and 108.]

[87] M. Pedley and Freescale Semiconductor, "AN3461: Tilt Sensing Using a Three-Axis Accelerometer," 2013. [Page 86.]

[88] W. McMahan, E. D. Gomez, L. Chen, K. Bark, J. C. Nappo, E. I. Koch, D. I. Lee, K. R. Dumon, N. N. Williams, and K. J. Kuchenbecker, "A practical system for recording instrument interactions during live robotic surgery," *Journal of Robotic Surgery*, 2013. [Page 88.]

[89] B. Mathieu, S. Essid, T. Fillon, J. Prado, and G. Richard, "YAAFE, an Easy to Use and Efficient Audio Feature Extraction Software," in *International Society for Music Information Retrieval Conference (ISMIR)*, Utrecht, 2010, pp. 441–446. [Page 91.]

[90] O. Tchernichovski, F. Nottebohm, C. E. Ho, B. Pesaran, and P. P. Mitra, "A procedure for an automated measurement of song similarity," *Animal Behaviour*, vol. 59, no. 6, pp. 1167–1176, June 2000. [Page 91.]

[91] E. Scheirer and M. Slaney, "Construction and evaluation of a robust multifeature speech/music discriminator," in *IEEE International Conference on Acoustics, Speech, and Signal Processing (ICASSP)*, Munich, 1997, pp. 1331–1334. [Page 91.]

[92] O. Gillet and G. Richard, "Automatic transcription of drum loops," in *IEEE International Conference on Acoustics, Speech, and Signal Processing (ICASSP)*, Montreal, 2004, pp. 2–5. [Page 91.]

[93] P. Boersma, "Accurate short-term analysis of the fundamental frequency and the harmonics-to-noise ratio of a sampled sound," in *Proceedings of the Institute of Phonetic Sciences*, vol. 17, Amsterdam, 1993, pp. 97–110. [Page 91.]

[94] W. McMahan, "Using Accelerometers to Localize Tactile Contact Events on a Robot Arm," in *Workshop on Advances in tactile sensing and touch based human-robot interaction, ACM/IEEE International Conference on Human-Robot Interaction (HRI)*, Boston, 2012. [Page 92.]

[95] M. Hall, E. Frank, and G. Holmes, "The WEKA data mining software: an update," *ACM SIGKDD Explorations Newsletter*, vol. 11, no. 1, pp. 10–18, 2009. [Pages 92 and 99.]

[96] J.-P. Merlet, "C-surface applied to the design of an hybrid force-position robot controller," in *IEEE International Conference on Robotics and Automation (ICRA)*, vol. 4, Raleigh, 1987, pp. 1055–1059. [Page 105.]

[97] P. Kazanzides, N. Bradley, and W. Wolovich, "Dual-drive force/velocity control: implementation and experimental results," in *IEEE International Conference on Robotics and Automation (ICRA)*, Scottsdale, 1989, pp. 92–97. [Page 105.]

[98] T. Yoshikawa and A. Sudou, "Dynamic hybrid position/force control of robot manipulators-on-line estimation of unknown constraint," in *IEEE Transactions on Robotics and Automation*, vol. 9, no. 2, 1993, pp. 220–226. [Page 105.]

[99] M. Hughes and G.-Z. Yang, "Line-scanning fiber bundle endomicroscopy with a virtual detector slit," *Biomedical Optics Express*, vol. 7, no. 6, p. 2257, 2016. [Page 106.]

[100] P. Giataganas, M. Hughes, C. J. Payne, P. Wisanuvej, B. Temelkuran, and G.-z. Yang, "Intraoperative robotic-assisted large-area high-speed microscopic imaging and intervention," *Transactions on Biomedical Engineering (TBME)*, pp. 1–9, 2018. [Page 106.]

[101] T. Vercauteren, A. Meining, F. Lacombe, and A. Perchant, "Real time autonomous video image registration for endomicroscopy: fighting the compromises," *SPIE BIOS-Three-Dimensional and Multidimensional Microscopy: Image Acquisition and Processing XV*, vol. 6861, p. 68610C, 2008. [Page 107.]

[102] M. J. Tsai and Y. H. Chiou, "Manipulability of manipulators," *Mechanism and Machine Theory*, vol. 25, no. 5, pp. 575 – 585, 1990. [Page 109.]

[103] R. C. Newton, D. Noonan, C. Payne, J. Andreyev, A. Di Marco, M. V. Scarzanella, A. Darzi, and G.-Z. Yang, "Probe tip contact force and bowel distension affect crypt morphology during confocal endomicroscopy," *Gut*, vol. 60, no. Suppl 1, pp. A12–A13, 2011. [Page 109.]

[104] C. A. Seneci, K. Leibrandt, P. Wisanuvej, J. Shang, and A. Darzi, "Design of a Smart 3D-printed Wristed Robotic Surgical Instrument with Embedded Force Sensing and Modularity," in *IEEE International Conference on Intelligent Robots and Systems (IROS)*, Daejeon, 2016, pp. 3677–3683. [Page 126.]

[105] T. Yoshikawa, "Manipulability of Robotic Mechanisms," *The International Journal of Robotics Research (IJRR)*, vol. 4, no. 2, pp. 3–9, 1985. [Page 132.]

[106] M. J. Tsai and Y. H. Chiou, "Manipulability of manipulators," *Mechanism and Machine Theory*, vol. 25, no. 5, pp. 575–585, 1990. [Page 132.]

[107] P. I. Corke, *Robotics, Vision & Control: Fundamental Algorithms in MATLAB.* Springer, 2011. [Page 136.]

[108] K. R. Arun, E. Ong, and A. W. H. Khong, "Source localization on solids using Kullback-Leibler Discrimination Information," in *International Conference on Information, Communications and Signal Processing (ICICS)*, Singapore, 2011, pp. 1–5. [Page 148.]

[109] D. Ma and J. Hollerbach, "Identifying mass parameters for gravity compensation and automatic torque sensor calibration," in *IEEE International Conference on Robotics and Automation (ICRA)*, Minneapolis, MN, 1996, pp. 661–666. [Page 149.]